# Development of New Catalysts for Methane Oxidation in Dual-Fuel HGV Engines

J. Kamieniak-Rodziewicz

PhD 2017

# Development of New Catalysts for Methane Oxidation in Dual-Fuel HGV Engines

Joanna Kamieniak-Rodziewicz

**A thesis submitted in partial fulfilment of the requirement of Manchester Metropolitan University for the degree of Doctor of Philosophy**

**School of Science and Environment**
**Manchester Metropolitan University**
**In collaboration with *G-Volution Plc.***

**August 2017**

## Declaration

This is to certify that the material contained in this thesis has been produced by the author and has not been accepted in substance for any other degree and is not currently submitted for any other academic award.

Joanna Kamieniak-Rodziewicz

# Abstract

1.4 billion tonnes of cargo is transported in the UK every year, using 1,445,000 heavy goods vehicles (HGVs) over a collective distance of 19 billion km and these figures are likely to increase in the future. For example, the number of trucks is expected to rise by 75% by 2040, and the demand for transport fuels will also grow rapidly. In view of that, natural gas has become subject to big investments for new businesses lines, such as dual-fuel engines. This type of engine typically utilises diesel as a primary fuel with the substitutions of natural gas in order to reduce running costs, as well as for environmental benefits. However, the main downside of the utilisation of natural gas is that it has a higher combustion enthalpy per unit mass, when compared to other conventional fuels. Also, it is not fully burned in the engine, thus results in increased methane emissions in the exhaust. The aim of this project is, therefore, to develop new catalysts to manage emissions of methane to meet the requirements established by the Euro VI regulations.

This thesis reports the synthesis and full characterisation of hydroxyapatite (HAP) as the support for a range of catalysts, using several methods and templates to improve its porosity. Moreover, carbon nanorods were employed for the first time as a hard-template in the synthesis of HAP, obtaining high BET surface areas that corresponded to 242.2± 2.3 $m^2g^{-1}$. Then, the thermal, chemical and mechanical stability of HAP was investigated by reproducing possible environmental conditions, which the catalyst would be exposed to in real exhausts from HGV engines. The main findings were that mesoporous HAP is fully stable to any change of pH and any mechanical disturbance, and only started to dehydroxylate at temperatures above 650°C, which is, nonetheless, higher than the engine operating temperature. In consequence, HAP was confirmed as an extremely powerful catalyst support.

Additionally, new methods for doping HAP with Pd and Ni metals were explored in order to improve the metal distribution on the support and, hence its catalytic activity. Ultrasound was utilised to assist conventional ion exchange (IE) and incipient wetness impregnation (IW) methodologies. The results for IW revealed that the ultrasound breaks down metal clusters and subsequently improves their distribution,

when compared to the standard IW protocol, and in the case of IE, even though the distribution remains stable, the utilisation of ultrasound significantly accelerated the process from 3 days to 3 hours. Furthermore, pretreatment of HAP with different pH before doping with Pd using the IW protocol considerably enhanced the metal distribution when compared to the conventional IW procedure, and remained the high metal distribution when IE took place in a different pH buffer solution instead of neutral water.

All synthesised and characterised samples were tested towards dry reforming of methane (DRM) and oxidation of methane, reproducing the oxygen lean and rich conditions found in an exhaust of a HGV, respectively. Products of the reactions were analysed using an in-house built catalysis rig equipped with GC-TCD. For DRM, the most active catalyst impressively exceeded the commercially available catalyst tested under same conditions; converting 100% at a temperature of 250ºC, and still achieving 80% conversion after 88 hours continuous reaction. On the other hand, it was found that the oxidation of methane in the presence of oxygen species proceeds through a redox cycle between reduced metal and metal oxide. Based upon the catalytic profiles of previously synthesised catalysts, the metal oxide was more active and revealed more stable conversions when compared to the reduced metal. The results obtained, therefore, suggest that the adsorbed lattice oxygen plays a key role in the catalysis reaction. Lastly, coking process was also studied *via* TGA as a preliminary deactivation process of the catalysts. It was found that all Pd and Ni based catalysts were resistant to the formation of carbon on their surface.

# Aims and Objectives

The primary focus of this project was to design and synthesise a cost-effective novel catalysts for methane decomposition in a dual-fuel engine for heavy goods vehicles, which could operate at the temperatures below 500°C providing high catalytic response. The objectives of this project are described in detail below.

## Objectives

1. Develop methane catalyst support with high thermal and structural stability.

2. Explore doping methods of metals that will contribute towards better catalytic activity of the materials. Assess different metals and their influence on the structure of the support.

3. Develop catalytic testing rig that will reproduce engine conditions and critically examine the activity towards methane decomposition.

4. Scrutinise the catalytic activity of the synthesised catalysts towards methane in both oxygen lean and oxygen rich conditions, using dry reforming of methane reaction and *via* complete oxidation, respectively. Benchmark the results against commercially available catalysts.

5. Examine deactivation process of catalysts by investigating carbon deposition as a main lifetime limitation.

# Acknowledgments

First and foremost, I would like to express my gratitude to my supervisors, especially Professor Craig Banks for the opportunity to conduct the work and for his trust and the 'green light' into perceiving my ideas in the experimental part of this project, which has gone into writing this thesis.

I would also like to offer special thank you to G-Volution Plc. for their financial contribution for this project. I am grateful for the support and enthusiasm from Paul Howard and Chris Smith and their thoughts provoking scientific discussions. The opportunity to work close to you both provided me invaluable experience and pushed my thinking outside of the lab scale at the university.

I owe my deep gratitude to Banks Research Group, for unforgettable team building days out, and our day-by-day discussions in the lab. Especially I would like to thank Ed for his support at all times. I learnt a lot about myself in terms of self-discovery based on your professional approach combined with your personality, and I am thankful for this.

I also want to thank my family, my Mum, Dad and Artur for their love and care, for believing in me, encouragement and understanding my reduced time spent at home due to 'one more' quick test in the lab. Kocham was i dziękuję za wszystko, bez was bym tego nie osiągnęła.

Finally, I would like to extend my huge thank you to Dr Elena Bernalte, for continues support, both professional and personal, who has always been there to listen about my results, my ideas or doubts as a work leader and my best friend. You sacrificed many hours to help me understand my results and encouraged me to keep going, even staying 24 hours in the lab with me to complete my stability tests. Your patience, impressive knowledge and intellectual insight into practically anything brought out the strongest parts of me and led to some of my best work. You have turned me from student to professional and I will be always grateful for this. Gracias, mi amiga, por ser quien eres y por todo lo que me das. For this reason, in addition to Artur, this thesis is dedicated to you.

*"Having chosen something worth doing, never give up, and try not to let anyone down"*

Harry Kroto (1939-2016), Nobel Prize Laureate in Chemistry

# List of Tables

# List of Figures

# List of Equations

# Table of Content

# Chapter 1: Introduction

This chapter introduces the important aspects of natural gas, which allow to facilitate the greater understanding of the aims of this project. Also, principles of dual-fuel engine is described with the European legislations for methane emissions and developed catalysts up to date are reviewed. The main features of hydroxyapatite are discussed and characterisation techniques are described in order to understand their important role in the materials prepared. Part of this chapter have been published in Trends in Analytical Chemistry, 2015, 73, 146-157.

## 1.1 Natural gas

### *1.1.1 Natural gas composition and features*

Natural gas (NG, hereafter) refers to hydrocarbon rich-gas. It is a mixture of paraffinic hydrocarbons, such as methane (>98%) with ethane, propane, butane *etc.* in small proportions. NG was first discovered by the 'father of Natural Gas', William Hart, in 1821 in Fredonia (US) and is naturally formed under the earth's surface.[1] As a consequence of drilling in the ground, in the 19$^{th}$ century NG was locally utilised as a natural source of energy, especially light. In its pure form, NG is odourless, colourless and lighter than air, therefore every leak dissipates into the atmosphere.[2] Since natural gas is over 98% methane, it is also generally referred as methane and if it is originated from organic waste is called biomethane. In *Figure 1.1* a classification of natural gas depending on the origin and chemical composition is summarised. In relation to the chemical content of natural gas, it can be classified into two different groups, depending on hydrocarbon content and sulfur content. According to hydrocarbon content, two types of NG can be distinguished, *dry gas*, where methane is the main constituent with trace amounts or no higher hydrocarbons, and *wet gas* where components other than methane make up more than 10 % by volume. Natural gas can be also classified based on sulfur content, which is usually in form of $H_2S$. In this regard, NG can be sweet, where there is negligible or no constituents of sulfur species, or sour, where $H_2S$ content exceeds allowable quantities and require further processing.[3]

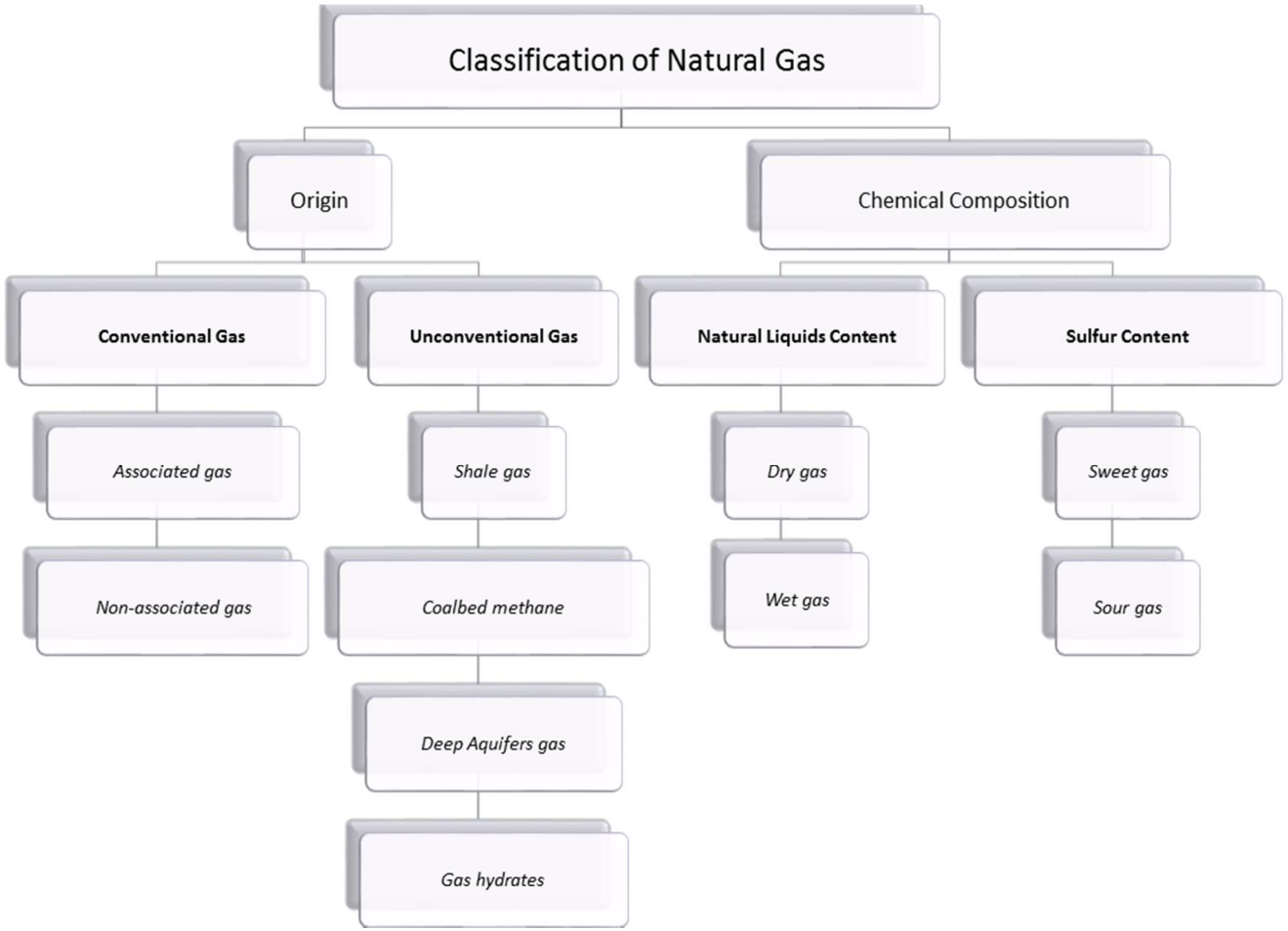


***Figure 1.1*** *Natural gas classification schematic diagram*

Methane cannot be absorbed in the body *via* skin or ingestion, although a person exposed to it *via* inhalation will experience dizziness, headache or nausea.[4] Such symptoms are not caused by the methane itself, but by the oxygen-deficient atmosphere created due to the high concentration of methane. Consequently, humans should never enter an area where methane concentration in air exceeds 1%. Long-term inhalation of methane caused by leaking pipes or a large release of the gas can be fatal *i.e.* when oxygen levels will be less than 12% .[5]

### *1.1.2 Natural gas origin*

Natural gas originates from three major processes: thermogenic, biogenic and abiogenic.[6] *Thermogenic* processes involve slow decomposition of organic materials that arise in sedimentary basins under the influence of temperature and pressure. In the anaerobic conditions, degradation of living organisms is slow and incomplete, and the residues accumulate and form complex structures, so-called kerogen, that requires thermal treatments *i.e.* maturation to complete the process of gas formation.

On the other hand, during *biogenic* processes methane is formed by the actions of living organisms, called methanogenic bacteria, on organic materials in the early stage of their burial or deposition of sediments. Such methanogens are present where electron acceptors are limited *e.g.* $O_2$ or $SO_4^{2-}$, and their typical territory involves flooded soils, anaerobic digesters or gastrointestinal tracks.[2] The last process that generates methane is called *abiogenic* and involves volcanic gases. Hydrocarbons are formed by the reduction of $CO_2$ during magma cooling, usually in hydrothermal systems during water-rock interactions.[7] Nevertheless, all naturally produced gas is found in gas reservoirs.

The gas reservoir is a natural storage area that consists of permeable and porous rocks, surrounded by water-resistant materials, and the natural gas is formed underneath the surface. The porous rocks store formed gas, which is then effectively sealed by impermeable rocks in order to prevent its escaping.[3]

Regarding its origin, natural gas can be classified into conventional and unconventional, as shown in *Figure 1.1*. Conventional gas can be found in deep reservoirs that are associated with the presence of crude oil (called as associated gas, and usually referred to wet gas, which is typically leaner in methane and contains paraffinic constituents) or contains little or no crude oil (non-associated gas, also called as dry gas, and is usually richer in methane). Nevertheless, after gas processing methane is produced in its pure form. Another class of natural gas is unconventional and involves several types of gas *i.e*. shale gas, coalbed methane, deep aquifer gas and gas hydrates.[8] A brief description of those is included below:

**Shale gas** can be produced through thermogenic, biogenic or a mixture of both pathways and can be found in low-permeability shale, sandy carbonates, dolomite, sandstone, siltstones, and limestones. It is important to note, that this type of gas is not associated with oil. According to stable isotope studies, it is mostly found in Illinois and southwestern Ontario, Canada.[9]

**Coalbed methane** is formed in coal seams through coalification processes by increasing temperature and pressure in the buried organic matter that is slowly transformed into coal. The major component of the produced gas is methane, with the trace amounts of ethane, $CO_2$, $N_2$ and $H_2S$. It has been well described in the literature that methane migrates faster than $CO_2$, thus it can be accumulated in the water-saturated layers of a basin as a free gas. Moreover, both gases can be adsorbed in the coalbed, which exhibits a macroporous structure. Hence it is important to monitor the concentrations of $CH_4$ and $CO_2$ in there to prevent possible explosions.[10]

**Deep aquifer gas** is generated due to gas migration through the aquifers to reservoir rocks. The content of the gas is strictly influenced by the temperature, pressure and salinity, because methane is not soluble in water, thus aquifers are typically largely saturated by this gas.[2]

**Gas hydrate,** known as 'the ice that burns'**,** originates from gas molecules captured in hydrogen bonded water molecules that can form hydrates at specific conditions, and is typically found in marine environments. This process happens through a nucleation step that involves nuclei formation (incubation time), followed by crystal growth filled with gas hydrate, which is generally created *via* microbial reduction of $CO_2$ from organic matter.[11]

Apart from the natural origins of NG, there are also chemical approaches developed to obtain methane. The main industrial methodology is called ***methanation***. In this process, the formation of methane takes place through the catalytic reaction of hydrogen with carbon monoxide (CO) or/and carbon dioxide ($CO_2$), as described by Gao.[12] A typical reaction involves the gasification of biomass to obtain synthesis gas, followed by its catalytic conversion into synthetic natural gas (SNG). Even though the noble metals are described as very active and selective towards this process, they are too expensive to be employed for large-scale production, thus Ni metal is the most widely utilised catalyst.

On the other hand, methane can also be produced through an eco-friendly route called ***bio-methanation***, which uses microbes to break down organic products, such as food waste, into methane.[13] This is essentially the process where organic waste is converted to biomethane and organic sludges, as occurs in anaerobic digesters.[14] In the anaerobic digestion process, organic waste is shredded and pretreated with high temperature and acid to enhance enzymatic hydrolysis, and therefore increase the rate of gas production.[15] Then, the hydrolysis products are treated with microbes and kept at a constant temperature of 30±1°C to digest the organic medium into methane.[14, 16] Generally, the industrial methane production process can take in the range of 12-14 days.[17] Moreover, this process is used industrially across many countries to satisfy renew-able energy directives, because it creates a useful energy source from waste materials that would otherwise be buried into landfill sites. For interested readers, the biomethanation process is described in a high level of detail in a review by Jaiganesh *et al*.[18]

### *1.1.3 Worldwide use of Natural Gas and its processing*

The worldwide demand for energy constantly increases and is predicted to grow further, because of the constant increase of human activities. Due to availability and abundance of fossil fuels resources, it can be predicted that their importance in the world's energy economy is unlikely to decrease quickly. Natural gas has found its great applications in many different sectors.

Due to its ignition properties and high heating capabilities, it is predominantly used as a fuel to provide domestic heating throughout the world. Besides, it is utilised to generate electricity *via* the combustion of methane.[2]

NG has been also utilised in the transport sector as a fuel for decades, with over 23 million vehicles worldwide running powered by natural gas with leading consumers in Asia and Latin America, according to a NGV Knowledge Base report from 2017 (*Figure 1.2*).[19] Nevertheless, there are about 3000 vehicles in US, interestingly more than half owed by the government only.

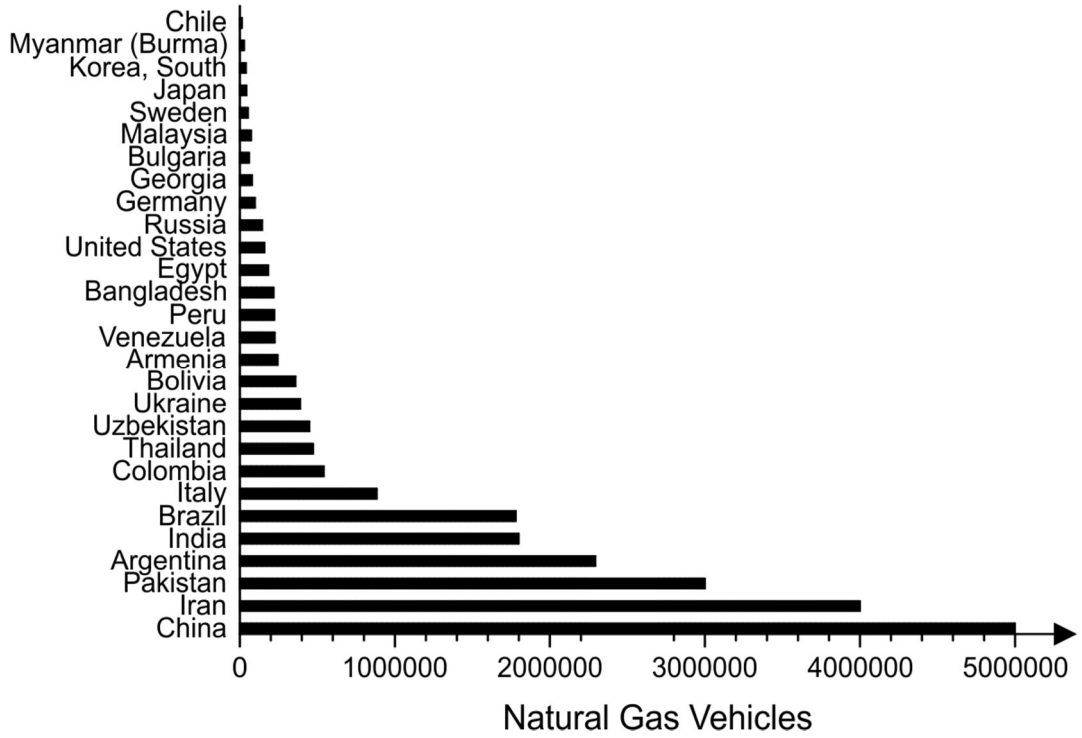


***Figure 1.2*** *World's leading consumers of NG powered vehicles, Source: NGV Global report 2017*

Before NG is received by the consumer, it needs to go through several processes (*Figure 1.3*). The first step is gas extraction *via* drilling and pumping from the natural reservoirs, which allows to obtain up to 60% of the reservoir capacity to be accessed. Then, depending on the source of the gas and its composition, the gas obtained is dehydrated to prevent water solidification during the cooling process, and raw gas is transferred to so-called treatment plants. A portion of the gas is placed in an acid gas removal unit, referred to sweetening unit, where any $CO_2$ and $H_2S$ present are removed.

Then, removal of mercury takes place to avoid its reaction with aluminium present in the heat exchangers, which in consequence can cause gas leaks and mechanical failure leading to catastrophic events. The resulting gas is prepared for transport through pipelines or cargo ships and trucks after compressing or liquidising processes. Finally, at the receiving terminals liquefied or compressed gas is re-gasified and sent to the consumers end.[20]

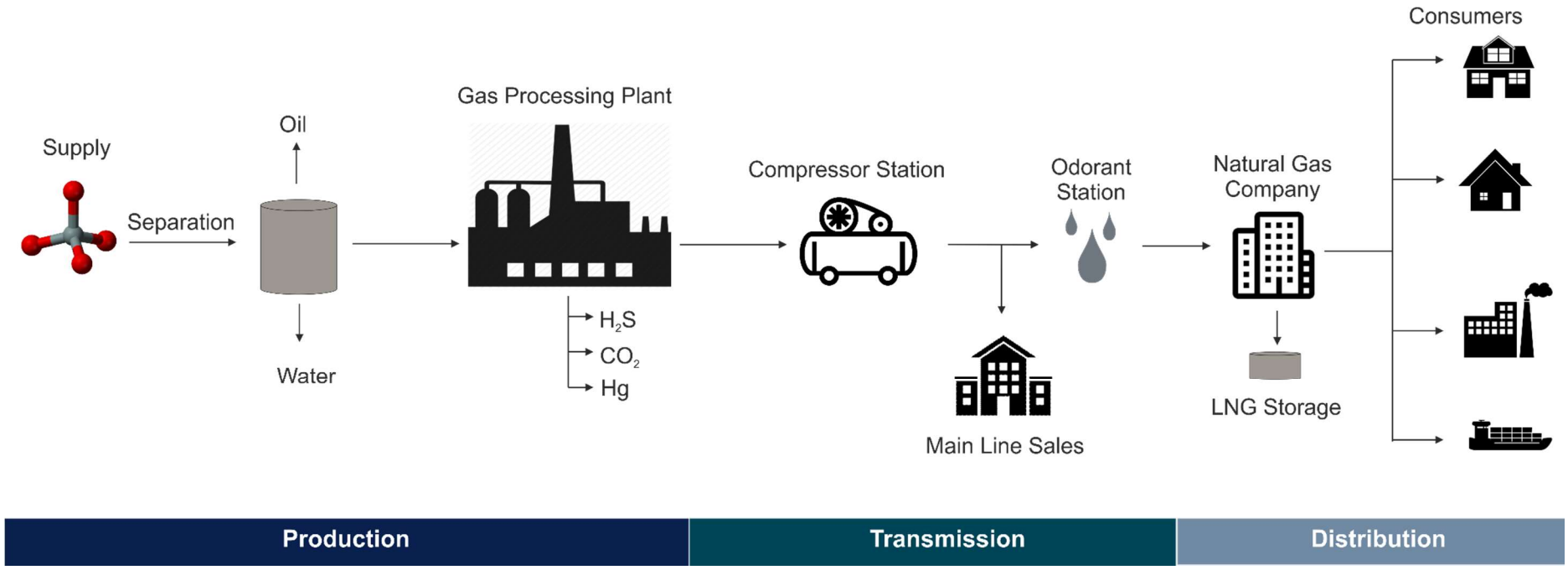


***Figure 1.3*** *Processing path of Natural Gas*

Today, Russia has achieved a major production milestone of over 180 billion $m^3$ of exported NG in one year, confirming their position as the world's leading producer and supplier of NG, followed by Qatar, exporting 120 billion $m^3$ of NG around the world (*Figure 1.4*). However, the USA is the most equipped supplier for Russian and Qatar's gas, maintaining an important role in the gas industry. On the other hand, the three biggest NG importers are Japan, Germany and United States that apart from supplying it further, utilise it in different sectors.

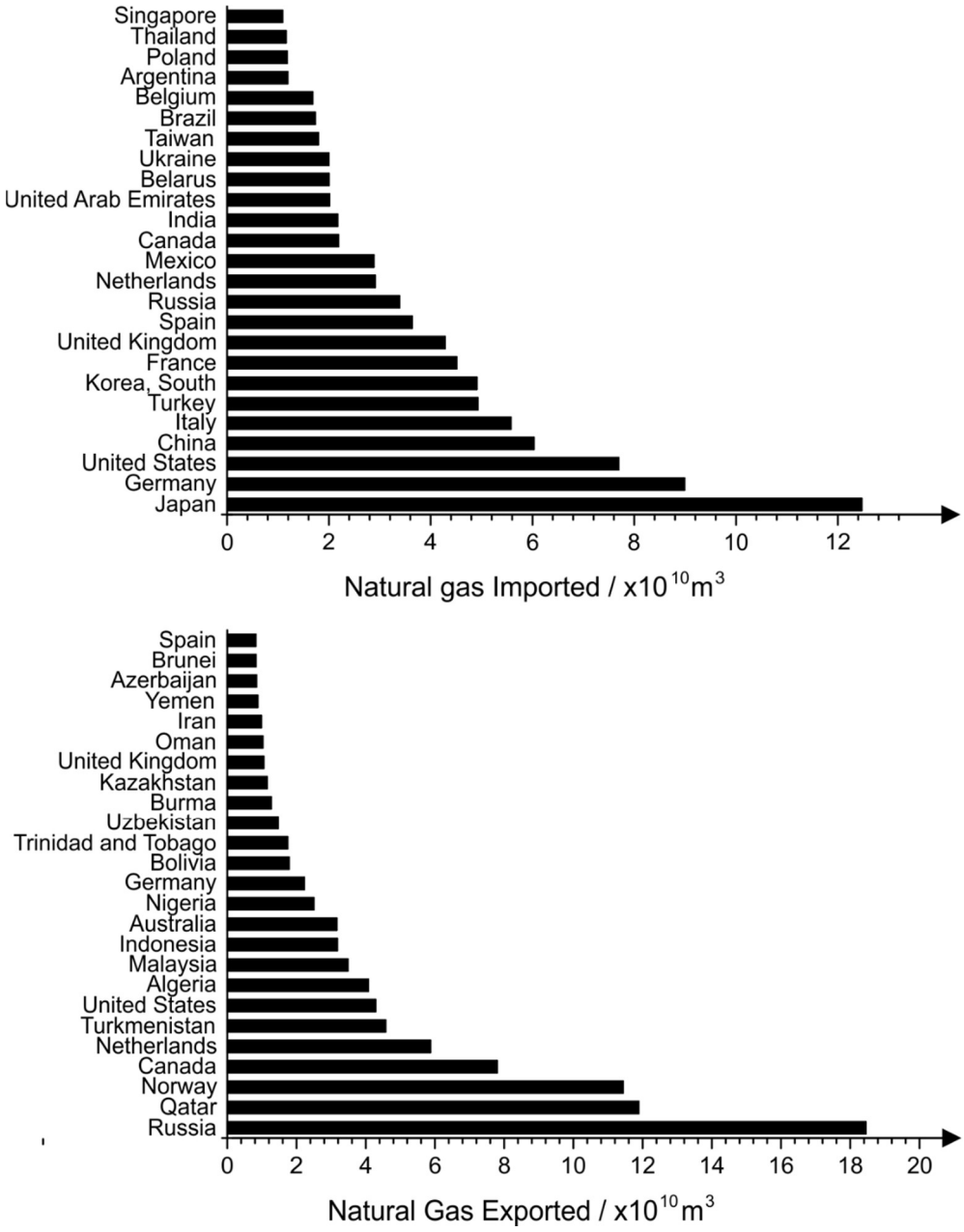


***Figure 1.4*** *Worldwide leaders in import and export of Natural Gas in 2014-2015, Source: The World Factbook*

It is interesting to note, that regarding utilisation of NG in the UK nearly half (45%) is produced by the UK itself and originates from the North Sea and East Irish Sea, followed by imported NG (21% from Norway and 35% from Russia), and the remaining 17% comes from imported LNG tankers.[21]

### *1.1.4 LNG vs CNG*

Natural gas can be stored either as compressed natural gas (CNG), liquefied natural gas (LNG) or even blended with hydrogen.[22] Since NG is environmental benign when compared to other fuels, it is also cost-effective and exhibits excellent efficiency making it the most preferred fossil fuel. NG is also much cleaner than coal and oil, hence the gas market gained great global recognition in the transport section.

Natural gas is converted to LNG by cooling it down to -162°C, at which point it transforms to liquid, thus reducing its volume by factor of more than 600, giving rise to the transportation possibilities over long distances.[22] However, the main downside of LNG is that it requires expensive cryogenic storage containers and it has a 7 day shelf life.

On the other hand, CNG is compressed in gaseous form to a pressure that corresponds to 200-250 kg $cm^{-2}$. Superior to conventional petrol, it operates at a third of its cost, making it a powerful alternative for automobile owners. Nevertheless, since there is heat gain during fuelling, the refill needs to be done at the slow rate, and is usually done overnight. In fact, CNG is more available and accessible than LNG, however it has been estimated that the use of LNG is more effective, especially in heavy duty trucks. In consequence, those vehicles need to be equipped with special dual-fuel systems in order to consume NG along with the conventional fuel.[23]

## 1.2 Dual-fuel engines and Environmental Regulations

### *1.2.1 Principles of Dual-Fuel Engines*

1.4 billion Tonnes of cargo is transported in the UK every year, using 1,445,000 heavy goods vehicles (HGVs) over a collective distance of 19 billion km and this is a subject to rise in future. Thus, as the number of trucks constantly increases and is expected to rise by 75% by 2040, the demand for transport fuels will also grow rapidly.[23] In consequence, the necessity for diesel fuel, which is the main fuel for HGVs, will increase by 85% over the same period.

In view of this evolution, the availability of diesel can become insufficient, and since oil reserves are in regions that are in frequent political instability, NG has been subject to large investments for future business lines.

As a fuel, NG has a clean nature of combustion and can reduce engine exhaust emissions by approximately 50% for non-methane hydrocarbons, 50-87% for $NO_x$, 20-30% for $CO_2$ and 70-95% for CO (*Figure 1.5*).[24] Another important advantage of using NG is its economical prospective, since NG coupled with diesel as a fuel is much cheaper, hence it provides lower running costs. Furthermore, by employing NG maintenance requirements are lowered, because NG does not mix or dilute with lubricants present in the engine. It is also not toxic or carcinogenic and can be easily adapted due to its high availability. Moreover, as long as safety is considered, NG is generally considered a safer fuel to use than other fuels due to its low density and high flammability limits that leads to higher dispersal rates, which in consequence are less likely to ignite in the events of leaks, when compared to diesel or gasoline.[25]

However, the main downside of the NG is the fact, that it has a higher combustion enthalpy per unit of mass when compared to other conventional fuels and is not fully burned in the engine, which results in increased methane emissions in the exhaust. In addition, NG/air mixture in cylinder is non-homogenous, thus its combustion is incomplete.

Consequently, scientists have combined diesel and gas into one engine, achieving major improvements from economic and environmental points of view, since replacing even a small proportion of the diesel with NG gives direct cost as well as environmental benefits.[25, 26]

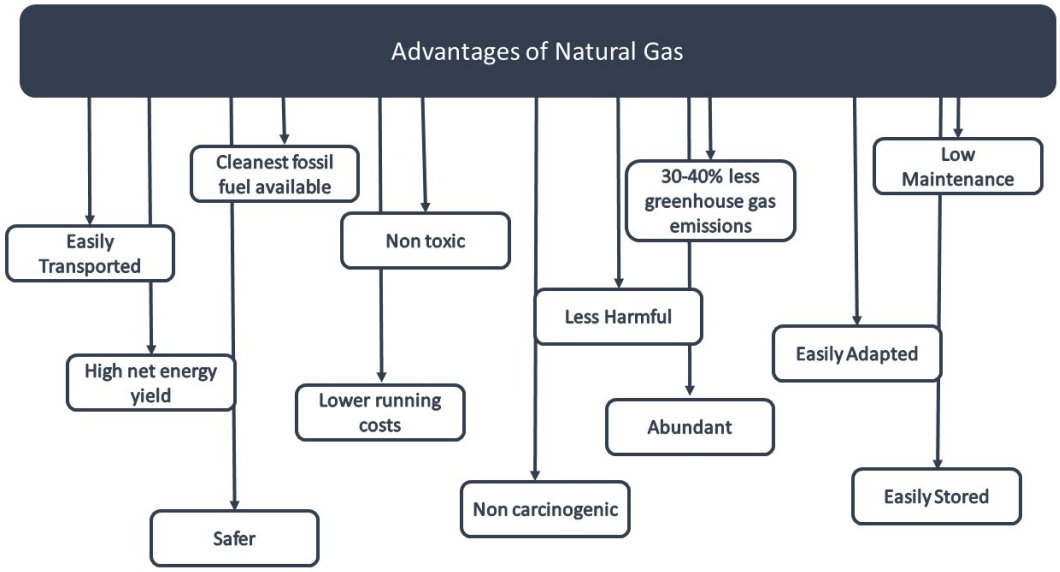


***Figure 1.5*** *Advantages of Natural gas as a fuel*

Dual-fuel engines were first introduced to the industrial transport market in 1939, produced by the National Gas and Oil Engine Co. in the UK and its utilisation drastically grew across the countries after the Second World War, due to its multiple aforementioned advantages. However, the earliest report found on a dual-fuel system was performed by Cave in 1929, in which hydrogen was introduced as a substituent in a diesel engine.[26] In the most typical dual-fuel engines, the original diesel engine is simply modified to be able to use diesel as a primary fuel and LNG or CNG as a secondary fuel, as shown in *Figure 1.6.*

The technology developed involves the coexistence of compression-ignition (CI) and spark ignition (SI) engines for combusting diesel and NG, respectively. To combust diesel, air is compressed at certain pressures and temperatures, at which fuel injected in the liquid phase easily fires and burns progressively by ignition.

On the other hand, spark ignition involves compression of a gas and air mixture under its ignition point, which is then fired at a special instant.[27]

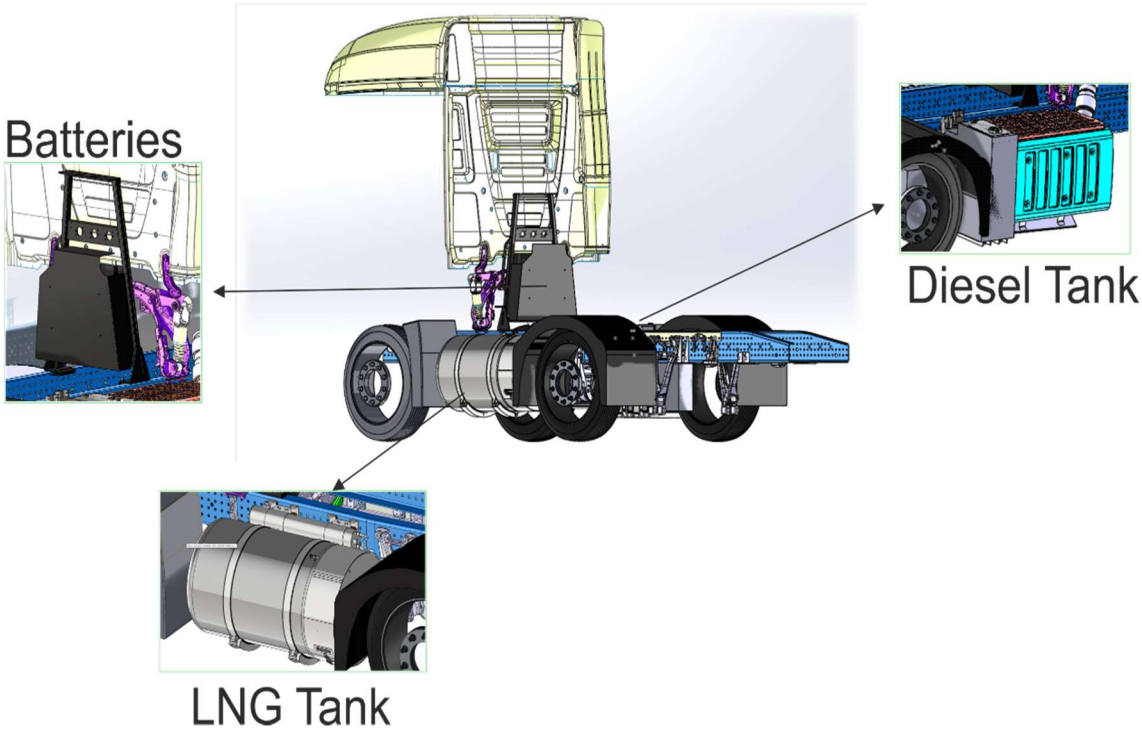


***Figure 1.6*** *Concept of Dual-Fuel Engines (Figure provided by G-Volution Plc)*

Engine cycle is generally divided into several steps: intake, compression, combustion, expansion and exhaust processing. The basic operation of a dual-fuel engine involves substitutions of gas *via* pulse-injections while running on diesel, and the amount of injected gas is highly dependent on engine load and speed. In order to control the substitution ratio through the journey, special software was developed, that is capable of calculating engine efficiency in real time and optimising the dosing of the gas. In view of that, that the amount of diesel has to be reduced by the software simultaneously with injecting the gas in order to maintain an equivalent power output.

The substitution ratio varies with the operational state of the engine between 0-49%, however the average dosing over all drive cycles corresponds to 20-25%. It is interesting to note that the power output of the engine remains unchanged when it operates on two fuel simultaneously. Regarding the operation of the dual-fuel engine, the vehicle starts on diesel only at all times, because LNG requires vaporising

before it is supplied into the engine. This involves a basic heat exchanger combined with a pressure regulator, at the point when the water temperature exceeds a pre-set point, the system automatically switches to dual-fuel.

To overcome the challenge of exhaust emissions, a catalytic converter is placed in the exhaust to transform unburnt methane into less harmful components. A typical converter consists of a can with the substrate of a honeycomb shaped ceramic support, which is coated with the developed catalyst that consists of a washcoat (support of the catalyst) and metal particles (Figu*re 1.7*). The mat secures the substrate in the metal sleeve and expands to compensate the size variations of ceramic substrate and metal sleeve across the temperature range.

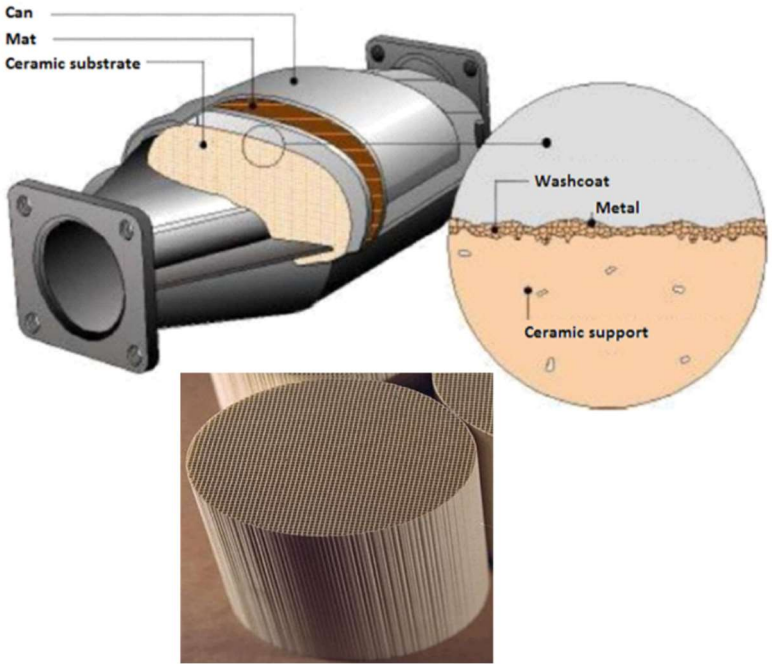


***Figure 1.7*** *Schematic of the catalytic converter in the exhaust (Figure provided by G-Volution Plc)*

## *1.2.2 Exhaust Emission Regulations*

Above and beyond the legislated reductions of certain exhaust gases, emissions are the critical issue faced by the current generation of engines that employ fossil fuels. In order to meet the regulations established by the Environmental Protection Agency (EPA) in US or/and 'Euro' for Europe, engine manufacturers continuously

need to improve the efficiency and technology, as the standards become stricter every year. Moreover, the most recent European regulations (EuroVI) introduced particle number (PN) emission limits for the first time. It is also worth noting, that there are two test cycles over which the vehicle needs to be examined *i.e.* steady state, where the speed and load are kept constant and transient state (*Table 1.1*), where speed and load vary over the engine cycle (*Table 1.2*).[28]

In general, it is agreed that the dual-fuel engine needs to meet the same regulations as a diesel-fuelled engine for steady state tests. In fact, surprisingly, emission data originated from EPA for this type of engines only include non-methane hydrocarbons, thus $CH_4$ emissions are not controlled by any regulations in the US.

***Table 1.1*** *Europe regulations for Heavy-Duty Diesel Engines during Steady-State Testing*

| Stage | Date | CO | HC | NOx | PM | PN | Smoke |
|---|---|---|---|---|---|---|---|
| | | g/kWh | | | | 1/kWh | 1/m |
| **Euro I** | 1992 ≤ 85 kW | 4.50 | 1.10 | 8.00 | 0.61 | | |
| | 1992 > 85 kW | 4.50 | 1.10 | 8.00 | 0.36 | | |
| **Euro II** | 1996 | 4.00 | 1.10 | 7.00 | 0.25 | | |
| | 1998 | 4.00 | 1.10 | 7.00 | 0.15 | | |
| **Euro III** | *1999 EEV only* | 1.50 | 0.25 | 2.00 | 0.02 | | 0.15 |
| | 2000 | 2.10 | 0.66 | 5.00 | 0.10 | | 0.80 |
| **Euro IV** | 2005 | 1.50 | 0.46 | 3.50 | 0.02 | | 0.50 |
| **Euro V** | 2008 | 1.50 | 0.46 | 2.00 | 0.02 | | 0.50 |
| ***Euro VI*** | ***2013*** | ***1.50*** | ***0.13*** | ***0.40*** | ***0.01*** | ***$8.0\times10^{11}$*** | |

*HC: hydrocarbons; NOx: nitrogen oxides; PM: particulate matter; PN: particle number.*

***Table 1.2*** *Europe regulations for Heavy-Duty Diesel and Gas Engines during Transient Testing*

| Stage | Date | CO | NMHC | $CH_4$ | NOx | PM | PN |
|---|---|---|---|---|---|---|---|
| | | g/kWh | | | | | 1/kWh |
| Euro III | *1999 EEV only* | 3.00 | 0.40 | 0.65 | 2.00 | 0.02 | |
| | 2000 | 5.45 | 0.78 | 1.60 | 5.00 | 0.16 | |
| Euro IV | 2005 | 4.00 | 0.55 | 1.10 | 3.50 | 0.03 | |
| Euro V | 2008 | 4.00 | 0.55 | 1.10 | 2.00 | 0.03 | |
| ***Euro VI*** | ***2013*** | ***4.00*** | ***0.16*** | ***0.50*** | ***0.46*** | ***0.01*** | $6.0\times10^{11}$ |

*NMHC: Non-methane hydrocarbons; NOx: nitrogen oxides; PM: particulate matter; PN: particle number.*

## 1.3 Environmental issues

Besides many powerful ways to utilise NG, it should not be forgotten that methane can be a dangerous gas. It is the second most abundant greenhouse gas (GHG) after carbon dioxide ($CO_2$), and exhibits explosive properties if the gas is not controlled; (even 5% of methane in the air can cause an explosion).[29-31] Although $CH_4$ is second to $CO_2$ in its overall contribution to global warming, it is up to 25 times more harmful than $CO_2$. However, yearly emissions of methane around the world are significantly smaller than that of $CO_2$, and concentrations of $CH_4$ in the atmosphere are 200 times lower than those of $CO_2$, $CH_4$ is responsible for about 20% of global warming.[32] Thus, for the reasons alluded to above, methane poses a huge environmental concern.

### *1.3.1 Methane worldwide emissions*

The biggest global threat originating from GHGs emissions is caused by increasing the average surface temperature referred to as global warming.[33] Methane is released both naturally and *via* human activities from different origins and its concentrations in the atmosphere has assumed alarming proportions. Over the last two centuries, the concentration of methane in the atmosphere has more than doubled.

This drastic change is due to the rapid growth in human activities, which increase the concentration of atmospheric methane through a variety of forms of emission routes.[33]

Methane is naturally emitted by grassland[34], wetlands[35, 36], coal beds[37], termites[38], lakes[39], wildfires[40] and oceans[41, 42], and corresponds to around 250 million tonnes each year. In general, methane emissions statistics vary quite significantly depending upon the source and besides naturally emitted methane, anthropogenic sources are generally grouped under three sectors: agriculture, energy and waste. Agriculture involves enteric fermentation (28%), rice cultivation (10%), manure management (6%) and other agricultural activities (10%). Energy sources consist of oil and gas (18%), biomass burning (3%), stationary and mobile sources (6%) and coal mining (6%) while the waste sector involves wastewaters (8%) and landfills (10%), as presented in *Figure 1.8*.[43]

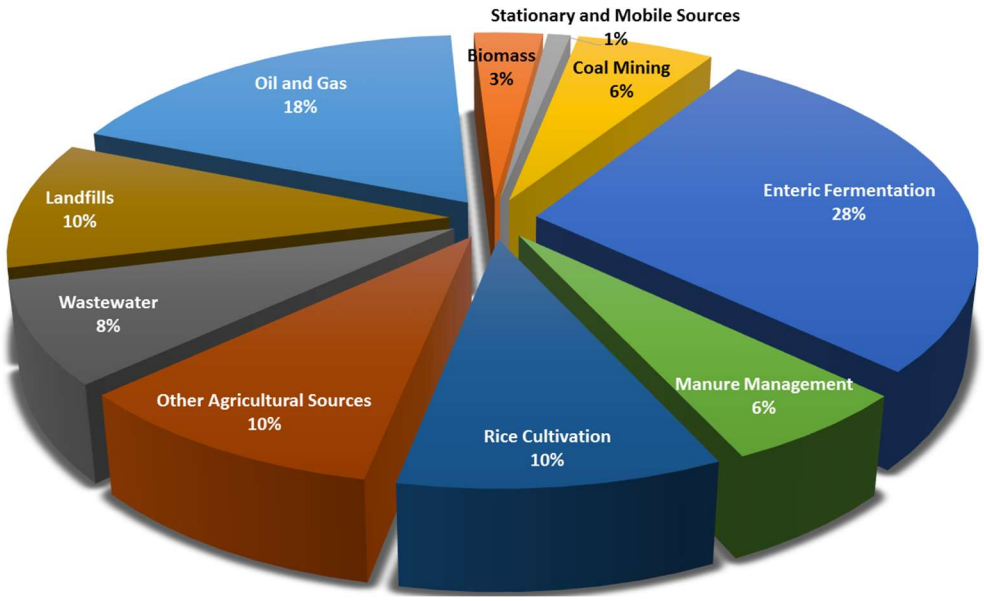


***Figure 1.8*** *Anthropogenic methane emissions in 2010*

Due to their variety of sources, methane emissions are affected by a number of factors, like energy use, distribution of human population, climate or agricultural practises. Nevertheless, taking into account natural and anthropogenic origins, the transport sector constitutes approximately 17% of total methane emissions. The biggest producer of GHGs is a road transport with the majority associated with HGVs,

followed by aviation and rail. Emissions are expected to increase by 26% between 2010 and 2030, thus becoming a great obstacle to overcome when designing new transport vehicles. [44]

### *1.3.2 Mechanism of methane transformations in the atmosphere*

The effect of methane on climate and atmospheric chemistry are a reason of concern. $CH_4$ is the most abundant reactive trace gas in the troposphere and its reactivity is important in both tropospheric and stratospheric chemistry. In the troposphere, in the presence of sufficiently high levels of NOx, $CH_4$ is oxidised by OH groups to form formaldehyde ($CH_2O$), carbon monoxide (CO) and ozone ($O_3$).

In view of that, methane helps to control concentrations of OH and CO in the troposphere. More-over, methane influences the amounts of water vapour and ozone in the stratosphere and plays a key role in the conversion of reactive chlorine species into less reactive HCl.

Nevertheless, there are only one major and two minor possible reactions for tropospheric methane. The most important determinant of the rate at which $CH_4$ is removed from the atmosphere is the concentration of OH.[45] This is due to the oxidation reaction that takes place between $CH_4$ and OH radicals, which is formed *via* photodissociation of tropospheric ozone and water vapour (*Figure 1.9*).

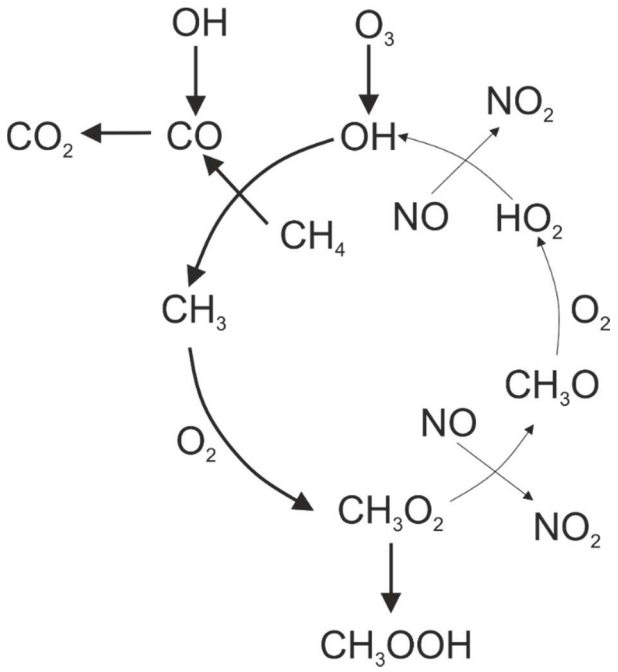


***Figure 1.9*** *Scheme of the methane oxidation cycle in the atmosphere. Note that the bold arrows in the first half of the cycle indicate no NOx present*

In consequence, the residue of methane is removed through dry soil oxidation and transported to the stratosphere. It is important to note, that the oxidation of $CH_4$ with OH species is a highly effective process and is capable of removing nearly 90% of $CH_4$ from the atmosphere.[1] In fact, this reaction is time consuming and the lifetime of methane in the atmosphere corresponds to nearly 9 years, this time is believed to be lower due to increased concentration of OH present in the troposphere.

However, the amounts of OH in the atmosphere are not only affected by $CH_4$, but also by the amount of CO produced, since it is further oxidised to $CO_2$ causing another drop in OH levels. This is called as feedback cycle, and the consequence is the increase of lifetime of methane. In this case, $CH_4$ concentrations are lowered at the slower rate than expected from the atmospheric lifetime even though there can be no apparent changes in the levels of OH.[1]

### *1.3.3 Impact of methane on climate*

There are two recognised types of effects of methane on the atmosphere: direct and indirect. Direct effects involve methane's capability to absorb infrared radiation emitted by the warm surface of the earth to space at the colder atmospheric temperatures, which leads to net trapping of IR in the atmosphere. This phenomenon is called the greenhouse effect. On the molar basis, an extra mole of $CH_4$ released to the atmosphere is about 24 times more effective in absorbing infrared radiation and hence affecting the climate when compared to each additional mole of $CO_2$ emitted. Following this, on a mass basis, a further kilogram of methane is 66 times more effective as a GHG than an extra kilogram of released $CO_2$. However, it is worth noting that the lifetime of $CO_2$ is longer than that of $CH_4$, and the dissociation of methane leads to the formation of $CO_2$ which has its own effects on climate.[44]

In addition to direct effects on the environment, methane can also indirectly influence the atmosphere *via* chemical interactions that affects other important gases present in the air. As already mentioned, $CH_4$ influences the levels of OH radicals, which apart from methane, plays a key role as a primary oxidising agent. In consequence, oxidation of methane is an important source of tropospheric and stratospheric ozone, stratospheric water vapour and $CO_2$, which is a consequent product of the reaction. It is expected in future that the concentration of tropospheric OH species are subject to change due to the increased amount of greenhouse gases released.[46]

Additionally, the increase of methane released to the atmosphere is associated with changes in tropospheric ozone, which is the most important indirect effect, even though the processes that affect ozone in the troposphere remain unclear.[47]

On the other hand, in the stratosphere, methane also plays an important role as a source of water vapour. Although concentrations of water vapour are relatively small, even small changes in their levels can significantly affect radiative forcing, in consequence enhancing the greenhouse effect associated with the increased levels of water vapour.

In addition, an increase of water vapour in the stratosphere leads to higher amounts of polar stratospheric clouds, which together with ice clouds are also efficient in enhancing the atmospheric greenhouse effect. Finally, the end product of oxidation of methane reaction is $CO_2$, one of the most important GHG.[1]

### *1.3.4 Projections for future*

Unfortunately, anthropogenic activities and consequent methane emissions are unlikely to slow down. Specifically in the transport sector, there is much research and development underway to convert the engines of many fleet vehicles in order to use methane and biomethane as a primary fuel. However, one area identified as requiring attention is that not all of methane injected into an engine is combusted due to the running temperatures, thus the exhausts of methane based vehicles eject higher levels of methane.

The obvious strategy is to create catalytic converters to chemically clean up the methane from the exhaust prior to its emission to the atmosphere. On the other hand, optimistic projections of stabilising atmospheric $CH_4$ levels in the future in the transport sector have been set by the Climate Change Act from 2008, where GHG emissions including $CH_4$ from HGV needs to decrease by 80% by 2050 (based on 1990s levels).[48]

## 1.4 Heterogeneous transformation of methane

### *1.4.1 Possible reactions to transform methane*

Since the $CH_4$ molecule is inert, drastic conditions are required to activate it, like high temperature or aggressive reactants, which can cause selectivity losses. For those reasons, there are limited industrial pathways that can be employed to transform methane. The most widely studied approaches involve dry ($CO_2$) reforming of methane, steam ($H_2O$) reforming, autothermal reforming and partial oxidation.[49] These techniques differ in the oxidant employed, kinetics, energies of the reaction and the final $CO/H_2$ ratio produced. For example, **steam reforming** provides synthesis

gas (syngas, CO and $H_2$) in a ratio of 1:3, which can be directly used for methanol or ammonia production since both require high $CO/H_2$ ratios. However, this approach can also lead to the water-gas shift reaction to produce $CO_2$ among CO and $H_2$ as a side product, which needs to be removed by expensive purification prior to utilisation of the syngas and is becoming a concern for the petroleum industry. Moreover, the major challenge during this approach comes with deactivation of the catalysts through sintering, carbon deposition and poisoning by trace elements like S, As, P and Pb.[49]

**Dry reforming of methane** has been reported as the most cost-effective approach from all reforming reactions. It is capable of producing high purity syngas, thus this type of reaction has drawn much attention and has been described further in *section 4.1.1*. Another interesting approach is **oxidation of methane** in the presence of oxygen, which is a highly exothermic process that causes safety issues associated with operating at high space velocities.[49] For this reason, such a reaction has not been applied in industry so far. Nevertheless, with oxygen employed as an oxidant a mixture of CO and $H_2$ at a ratio of 1:2 is obtained. However, with oxygen species present in the reaction production of $CO_2$ is more favourable than production of syngas, which from an engine point of view is a desirable advantage. In fact, many side reactions may take place at the same time as oxidation of methane, all described in *section 6.1.1*.

### *1.4.2 Catalysts employed to transform methane*

Different catalysts have been developed to transform methane to less harmful components; most of them employ palladium, platinum, nickel, rhodium or cobalt, which show the highest catalytic activity and selectivity towards methane, independent of the oxidant employed (*Table 1.3*).[30, 50-54]

Since the metals are expensive and have limited availability, different supports have been applied together with small amount of metal particles (up to 10 wt%). For this reason, a plethora of the materials with different physicochemical properties have been extensively reported in the literature as a catalytic support in order to

enhance the avail-ability of the metal to the catalytic reaction. The majority of them involve oxides, such as ɣ-$Al_2O_3$, $TiO_2$, $SiO_2$, $CeO_2$, $Mn_3O_4$ and $ZrO_2$, as summarised in the review by Gelin *et al.*[55], with most widely employed and commercialised catalyst support for methane reforming in HGV engine being ɣ-$Al_2O_3$.[56-60]

However, among ɣ-$Al_2O_3$, zirconia reports higher stability in the catalytic performance over time on stream.[61] A summary of different metal/support combinations with their reaction conditions and catalytic activities are included in *Table 1.3*

***Table 1.3*** *List of interesting catalysts with utilised loading method, reaction employed and activity towards methane decomposition*

| Metal | Support | Loading Method | Reaction | Detector | Maximum Activity | Reference |
|---|---|---|---|---|---|---|
| **Pd/Pt** | ɣ-$Al_2O_3$ | IE | Complete Methane Oxidation | MS | 50% at 500°C | [53] |
| **Pd** | $ZrO_2$ | IW | Methane Combustion | IR | 92% at 800°C | [30] |
| **Pd** | ɣ-$Al_2O_3$ | IW | DRM | GC-TCD | 69% at 700°C | [62] |
| **Pd** | $CeO_2$ | IW | Methane Oxidation | GC-TCD | 100% at 450°C | [63] |
| **Pd** | $CeO_2$ | IW | Steam Reforming of Methane | IR | 7% at 300°C | [64] |
| **Pd/Ni** | $Co_2O_4/SiO_2$ | Co-precipitation | Complete Methane Oxidation | GC-TCD | 100% at 387°C | [65] |
| **Ni** | $CeO_2$ | IW | DRM | GC-TCD | 12% at 550°C | [66] |
| **Ni** | $ZrO_2$ | IW | DRM | GC-TCD | 65% at 750°C | [67] |
| **Ni** | ɣ-$Al_2O_3$ | IW | DRM | GC-TCD | 63% at 800°C | [68] |
| **Ni** | ɣ-$Al_2O_3$ | IW | DRM | IR | 95% at 850°C | [54] |

| | | | | | | |
|---|---|---|---|---|---|---|
| **Ni/Co** | ɣ-$Al_2O_3$ | IW | DRM | IR | 88% at 850°C | [54] |
| **Ni/Co/Mg** | ɣ-$Al_2O_3$ | IW | DRM | IR | 95% at 850°C | [54] |
| **Ni** | $SiO_2$ | IW | DRM | GC-TCD | 95% at 900°C | [69] |
| **Rh** | $SiO_2$ | IW | DRM | GC-TCD | 72% at 800°C | [70] |
| **Rh** | $ZrO_2$ | IW | DRM | GC-TCD | 32% at 783°C | [70] |
| **Rh** | $TiO_2$ | IW | DRM | GC-TCD | 66% at 780°C | [70] |
| **Rh** | ɣ-$Al_2O_3$ | IW | DRM | GC-TCD | 79% at 742°C | [70] |
| **Pt** | $CeO_2$ | IE | Partial Oxidation | GC-TCD | 100% at 800°C | [71] |
| **Pt** | $ZrO_2$ | IW | DRM | GC-TCD | 18% at 800°C | [72] |
| **Pt** | ɣ-$Al_2O_3$ | IW | DRM | GC-TCD | 46% at 800°C | [73] |
| **Pt** | Ce/$ZrO_2$ | IW | DRM | GC-TCD | 21% at 800°C | [72] |
| **Pt** | La/$ZrO_2$ | IW | DRM | GC-TCD | 26% at 800 | [72] |
| **$Co_3O_4$** | $CeO_2$ | Co-precipitation | Methane Oxidation | IR | 43% at 465°C | [74] |

| | | | | | | |
|---|---|---|---|---|---|---|
| **$Co_3O_4$** | $CeO_2/ZrO_2$ | Co-precipitation | Methane Oxidation | IR | 78% at 500°C | [74] |
| **Co** | γ-$Al_2O_3$ | Hydrogel | DRM | GC-TCD | 32% at 700°C | [75] |
| **Co** | MgO | IW | DRM | GC-TCD | 92% at 900°C | [76] |
| **Co** | $SiO_2$ | IW | DRM | GC-TCD | 12% at 850°C | [54] |
| **Ru** | γ-$Al_2O_3$ | IW | DRM | GC-TCD | 46% at 750°C | [77] |
| **Ru** | $CeO_2$ | IW | DRM | GC-TCD | 52% at 750°C | [77] |
| **Fe** | γ-$Al_2O_3$ | IW | Methane Decomposition | GC-TCD | 70% at 750°C | [78] |
| **Fe** | $CeO_2$ | Co-precipitation | Methane Decomposition | GC-TCD | 25% at 750°C | [79] |

It is generally reported that the observed variations in the activity of the catalysts are attributed to the acid-base properties of the support, which can either enhance or inhibit the catalytic performance of the metals. For example, as reported by Wu *et al*. an increase in the acidic strength of the support favours propane oxidation, therefore in their study, the alumina support was acidified with $H_2SO_4$ prior to the metal doping.[80] However, in the particular case of methane, its activation has been assigned to basic sites within the support, and this phenomenon is further described in *section 4.1.1*. The other important aspect that needs to be considered to achieve the maximum catalytic potential of the material is high dispersion of the metal in the matrix of the support. Taking both factors into account, Sugaya *et al.* observed a linear correlation between electronegativity of the cation in the metal oxide and the turnover number (TON), which refers to the number of moles of substrate that catalyst can convert before becoming inactive.[81]

Nevertheless, there is still a necessity for new supports that exhibit high thermal stability and porosity, and will also reduce the cost of the catalyst enhancing the performance of the metal in catalytic reactions.

## 1.5 Hydroxyapatite

### *1.5.1 Chemistry of Hydroxyapatite*

Hydroxyapatite (HAP) is an inorganic compound from the family of apatites with the general formula $Ca_5(PO_4)_6OH$, however the formula of the unit cell corresponds to $Ca_{10}(PO_4)_3(OH)_2$. It has been thoroughly described in the literature that HAP is the most stable form of calcium orthophosphate of all apatites.[82] Regarding the unit cell arrangements, HAP can be represented as $M1_4M2_6(PO_4)_6(OH)_2$, where calcium exhibits two crystallographic positions. Four calcium atoms occupy M1 position and are surrounded by nine oxygen atoms from the $PO_4$ tetrahedra, while the other six calcium atoms occupy M2 positions where they are coordinated by six oxygen atoms from $PO_4$ groups and one oxygen, which belongs to the OH group (*Figure 1.10*).[83]

Specifically, $Ca^{2+}$ ions are more flexibly arranged within the lattice, which in consequence is more prone to display $Ca^{2+}$ vacancies, whereas $PO_4^{3-}$ ions refine the hexagonal shape of the crystal. The arrangement of the Ca atoms are built up around $PO_4$ groups, providing stability to the structure.[84]

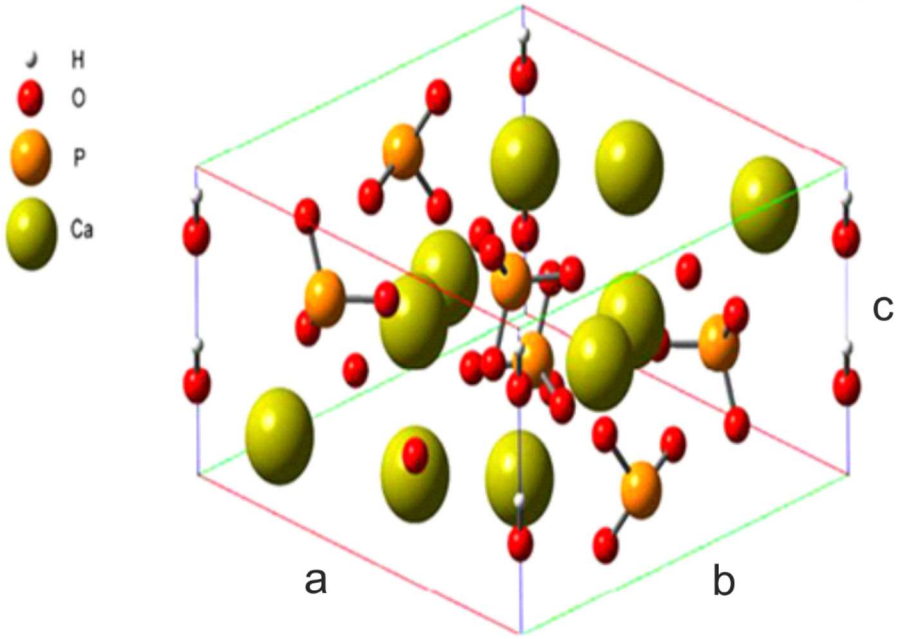


***Figure 1.10*** *Unit cell arrangement of HAP*

HAP exhibits a hexagonal $P6_3/m$ space group with the unit cell dimensions of a=b=0.937 nm and c=0.6881 nm, but they are subject to change depending on the additives. The standard X-ray diffraction pattern of HAP (JCPDS 09/0432) is presented in *Figure 1.11*. It is interesting to note, that Retvield analysis can be also employed in XRD analysis to detect any variations within the unit cell constants and any shift of the diffraction peaks in order to detect any impurities or secondary phases.[84]

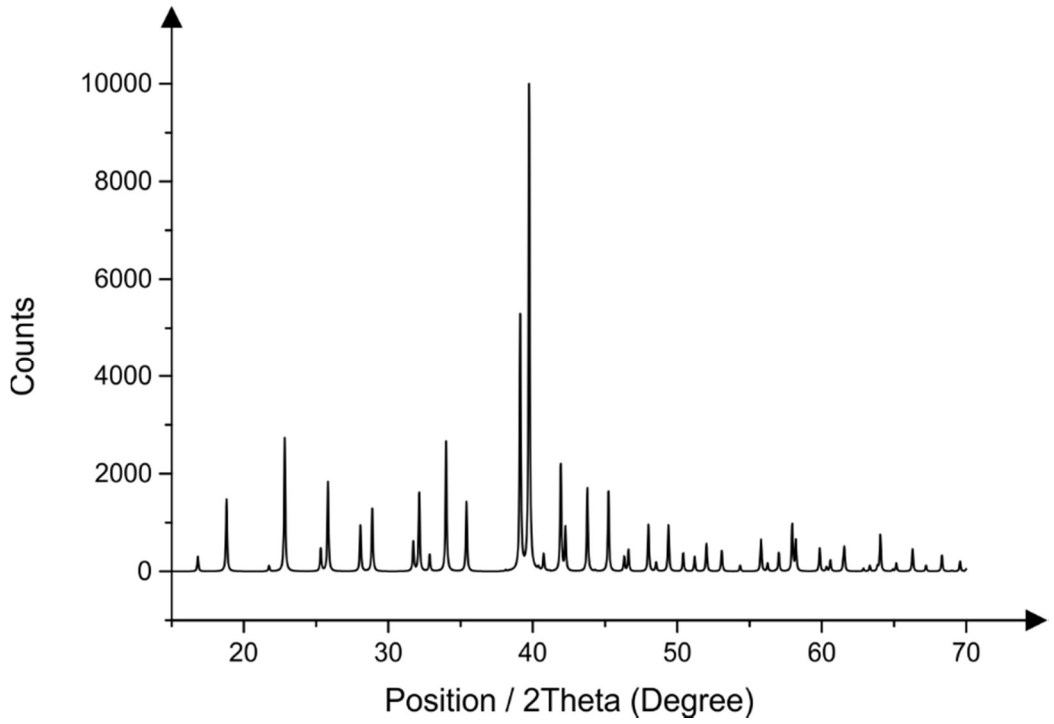


***Figure 1.11*** *Standard XRD pattern of HAP (JCPDS 09/0432)*

The major impurity that can be found within HAP is carbonate (3-8 wt%) originating from carbonate ions present in the precursors utilised during the synthesis, or from simply adsorbing $CO_2$ from air, and it is possible for it to occur *via* two different substitutions. One route involves replacement of OH group by $CO_3^{2-}$, and because the OH group is a much smaller specie it leads to expansion along the a-axis and contraction of the c-axis. Whereas in the case where $CO_3^{2-}$ substitutes for a $PO_4$ group, it has the opposite effect on the lattice parameters. In fact, any changes in crystal parameters often influence its physicochemical properties and thus its response depending on the application. For example, for biological applications carbonated HAP has been described as more bioactive when compared to the pure form of HAP, which is attributed to enhanced solubility of the carbonated phase.[85] In addition, HAP has two types of crystal planes, which carry different charges: positive on the a-plane and negative on the c-plane. It is assumed that the a-plane attracts acidic proteins, while the c-plane tend to adsorbs basic ones.[86] In view of this, HAP becomes bifunctional with a bright future in many different sectors of science.

Since HAP is a ceramic material, interactions within its structure have been described as a mixture of ionic and covalent bonds, which are characteristic for this type of materials. However, there are many crystal structures that calcium orthophosphate can form, depending on the stoichiometry and conditions during the synthesis. The main phases are listed in *Table 1.4.*

***Table 1.4*** *The main phases of calcium orthophosphate that can be obtained through precipitation*

| *Phase name* | *Chemical Formula* | *Ca/P ratio* | *Space group* |
|---|---|---|---|
| *Hydroxyapatite (HAP)* | $Ca_{10}(PO_4)_6(OH)_2$ | 1.67 | Hexagonal $P6_3/m$ |
| *Tetracalcium Phosphate (TTCP)* | $Ca_4(PO_4)_2O$ | 2.0 | Monoclinic $P2_1$ |
| *Octacalcium Phosphate (OCP)* | $Ca_8H_2(PO_4)_6 \cdot 5H_2O$ | 1.33 | Triclinic $P^1$ |
| *α-Tricalcium Phosphate (α-TCP)* | $Ca_3(PO_4)_2$ | 1.5 | Monoclinic $P2_1/a$ |
| *β-Tricalcium Phosphate (β-TCP)* | $Ca_3(PO_4)_2$ | 1.5 | Rhombohedral R3cH |
| *Dicalcium phosphate (DCPA)* | $CaHPO_4$ | 1.0 | Triclinic $P^1$ |
| *Dicalcium Phosphate dehydrate (DCPD)* | $CaHPO_4 \cdot 2H_2O$ | 1.0 | Monoclinic $I_a$ |
| *Oxyapatite (OAP)* | $Ca_{10}(PO_4)_6O$ | 1.67 | Hexagonal $P6_3/m$ |
| *Oxyhydroxyapatite (OHAP)* | $Ca_5(PO_4)_3(OH)_{1-X}O_{X/2}$ | 1.67 | Triclinic $P6_3/m$ |

In order to obtain a pure phase of HAP during the synthesis, the molar ratio of Ca/P needs to be set to 1.67. Otherwise the precipitated minerals can contain other phosphate forms.

Regarding the crystal structure of HAP, it is a relatively hard crystal, however it has an unusually low interfacial energy, which explains the formation of small crystals *via* nucleation. In fact, other thermodynamically less stable calcium phosphates also exhibit lower surface energies, thus they nucleate faster than HAP and they are often present as intermediates which leads to the eventual formation of HAP. This will be extensively described in *Chapter 2*.

### *1.5.2 Applications of Hydroxyapatite*

The structural and chemical features of HAP provide all the essential requirements for its application in many different scientific areas, with the additional advantage of its low production costs (*Figure 1.12*).

In the biological conditions, HAP is known as a mineral component of bone and is responsible for its superior toughness, but also exhibits excellent biocompatibility, bone-bonding ability, and possesses no toxicity or inflammatory response towards the human body. Thus it has been widely applied in biomedicine.[87] There is a plethora of examples where the utilisation of HAP is described in the literature, and mostly involving the replacement of damaged parts of musculoskeletal systems, but it also plays a crucial role in drug or gene delivery agents using substituted HAP.

An interesting summary is the current review written by Supova *et al*.[88] In fact, although it has been described that ingrowth of HAP in human bones increases with the porosity of HAP, at the same time the degradation rate of porous HAP also increases, limiting its in vitro reactivity. However, such problems have been overcome with substituted HAP, making it a perfect biomaterial.[87, 89] For instance, Wiesmann and co-workers described HAP substituted with potassium that was later involved in the process of dentin mineralisation.[90] Other than potassium, zinc can be found in all biological tissues and plays vital role in different biological functions, yet deficiency of this mineral is associated with decreased bone density, thus Zn substituted HAP has been extensively investigated to promote osteoblast activity.[91]

Besides biomedical applications, the specific characteristics of HAP, such as low water solubility and high stability under oxidising and reducing conditions, make this material suitable for environmental applications as a sorbent in the purification of wastewater and removal of a variety of heavy metals, such as arsenic (III), selenium (IV), lead (II), cadmium (II), cobalt (II) or nickel (II) from contaminated industrial aqueous waste.[92-96]

Another powerful application of HAP is the determination of ammonia for applications such as environmental pollution control, reported by Zhang *et al*. who describes the electrochemical detection of ammonia (at room temperature) using a composite of HAP/graphene which exhibits a significant improvement in the analytical sensitivity compared to that of a bare graphene sensor.[97] These specific applications of HAP require careful control of properties, such as particle size, dimensional anisotropy, morphology, real microstructure *etc.,* all of which are critically important for the optimisation and utilisation of HAP.[98, 99]

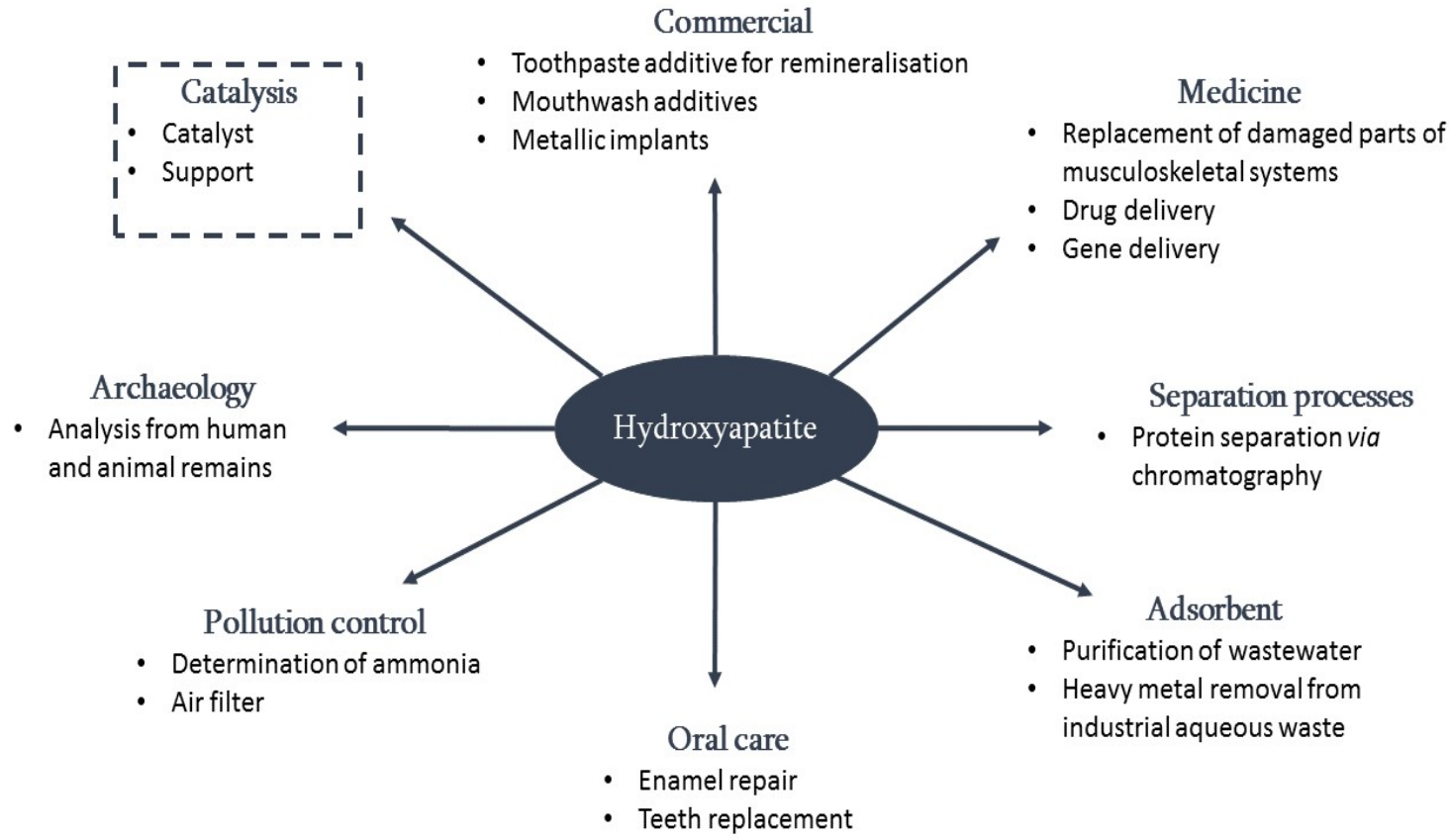


***Figure 1.12*** *Applications of Hydroxyapatite*

In recent years, HAP found its powerful applications in catalysis fields and is typically used as a catalyst support for a limited amount of metals/metal oxides due to its high structural stability, bifunctionality of acidic and basic sites within the structure and the possibility of isomorphous substitution.[100-103] The addition of metals, either as nanoparticles and/or substituted into the framework, greatly increases the range of reported reactions including acetone condensation[104], water-gas shift[105], alkane dehydrogenation/oxidative coupling[106-109], alcohol synthesis/transformation[110] or oxidation of volatile organic compounds[111-113], alcohols[114, 115], carbon monoxide[116] and also methane[117-119]. For example, in the study reported by Mori *et al.* palladium nanoclusters were applied onto HAP surfaces and employed towards selective oxidation of alcohols with the use of molecular oxygen.[100]

On the other hand, palladium metal coupled with HAP was also utilised in Suzuki-Miyaura cross-coupling reactions with sixteen different aryl boronic acids and several different aryl halides, described by Indra *et al*.[101] However, it is not only palladium metal that has been successfully assembled with HAP; rhodium supported HAP has also been investigated towards hydrogen generation from the methanolysis of ammonia borane, revealing very high activity.[102] Besides these the hydrophilic properties of HAP allow it to be used directly as a heterogeneous catalyst in dehydration reactions, *e.g.* the reaction of lactic acid to produce acrylic acid, an important intermediate for acrylate polymers and other key molecules[120, 121], or in the Guerbet coupling of alcohols.[122-124] Additionally, Yoon and co-workers studied the effects of adding ceria to Ni/HAP catalysts with a view to reducing the well-established tendency for Ni to generate carbon during reactions. Results showed that ceria doped samples enhanced the catalytic stability, due to the oxygen storage capacity of ceria preventing excessive carbon deposition.[125]

Regards methane transformation, Sugiyama *et al.* have extensively reported various stoichiometric forms of apatites and their selectivity towards catalytic activity in the presence and absence of tetrachloromethane (TCM), stating that with the stoichiometric HAP (Ca/P ratio 1.67) the products obtained are $CO_2$ and $H_2$ while its non-stoichiometric analogue ($1.67>Ca/P\geq1.50$) is more selective towards CO and $H_2O$.[126]

On the other hand, stoichiometric HAP favours dehydrogenation of alcohols while the other form favours dehydration, with enhanced activity observed along with the increased acidity of the catalyst. However, the source of such differences remains unclear since calcium vacancies may be distributed throughout the lattice of HAP and low Ca/P ratios can lead to the formation of other phosphate analogues or a mixture of both.[127] Nevertheless, activation of methane has been attributed to basic sites present on the surface of the catalyst making stoichiometric HAP (Ca/P 1.67) an extremely attractive support as it was reported to possess hydroxyl groups that are available for the reaction.[128, 129] In fact, even though HAP has been extensively explored towards different catalytic reactions, methane decomposition over modified HAP remains the subject of research. Boukha *et al.* studied Ni doped HAP for the DRM reaction and reported low (22%) methane conversion at 600°C.[130]

Also, Jun *el al.* synthesised similar catalysts that involved Ni supported by HAP with higher methane conversion corresponding to 88% at 750°C.[118] However, the temperatures at which a number of authors claim catalytic conversion of methane described here and also summarised in *Table 1.3* could be also attributed to partial thermal cracking of methane rather than a catalytic reaction, or a mixture of both resulting in different methane conversions.

For these aforementioned reasons, stoichiometric HAP has been chosen in the present work as a support material for metals for the catalytic transformation of methane and its further implementation in dual-fuel engines.

## 1.6 Physicochemical Characterisation Techniques

A plethora of analytical techniques has been employed in this thesis to characterise the synthesised materials and study their physicochemical properties. In this section, a brief description of the fundamentals of the techniques employed are described as well as the specifications of the equipment employed throughout this work.

### *1.6.1 Scanning Electron Microscopy (SEM), Energy-Dispersive X-ray (EDX) Spectroscopy and Transmission Electron Microscopy (TEM)*

SEM (scanning electron microscopy) imaging has been employed to analyse the surface morphology of the synthesised materials and reveal particle shape, size and nature of the prepared catalysts with the resolution down to 2-5 nm. Microscopic images were recorded using a Supra 40VP model manufactured by Carl Zeiss Ltd. coupled to an Apollo 40SDD energy-dispersive X-ray spectroscopy (EDX) system to obtain elemental composition of the materials.

SEM is capable of producing excellent topographical images of both conductive and non-conductive solid materials at very high magnifications (even 300 000X), however most images are produced with magnification below 8000X. Non-conductive materials are usually coated with a layer of gold or carbon to prevent the material from charging under the microscope and improve quality of the image. The SEM instrument consists of a tungsten filament, which generates beam of a high energy electrons focused into a small beam directed onto the surface of the sample. Two types of signals can be then generated, by secondary electron or *via* back-scattered electrons. In the signal caused by secondary electrons, created ions are loosely bounded outer electrons released by the impact of high energy incident electrons, and this is the most common imaging approach, On the other hand, back-scattered electrons are detected through the reflected electron wave. To produce an image, the electron beam is scanned in a raster pattern and emitted electrons of each type are detected by electron detector.[131]

Energy dispersive X-ray spectroscopy (EDX) is a semi-quantitative technique used in conjunction with SEM that is able to perform elemental analysis of the material. After the material is bombarded with a high energy electron beam originated from the SEM, emitted electrons from the atoms generate the free electron vacancies that are filled by electrons from higher states. This leads to the emission of X-rays to balance the difference in the energy, which are characteristic of the element from which they are emitted. Then, the detector produces spectra of emitted X-rays as a function

of their energy, which allows the elements present to be identified. The main limitation of this technique is that it can only detect features that are not smaller than 1µm, and elements with energy higher than 1keV (Z=11), thus it is unable to analyse very fine particles present in the sample. Elements with lower energy than 1 keV will be absorbed by the Be window.[132]

Furthermore, transition electron microscopy (TEM) was conducted using a JEOL JEM 2100 and a high resolution transition electron microscope (HR-TEM) was utilised where appropriate with JEOL 3000F. Those are a powerful techniques with the highest point resolution of 0.05 nm and possible magnification of 50 000 000X. In the case of TEM, the detected electrons are those, which are transmitted through the specimen and as they pass through, an image is generated. It is worth noting, that the TEM produces images of a thin layer of the material, which can provide information about pores within the structure and the position and distribution of metal particles present.[133] Even though TEM is more accurate than SEM, it involves sample preparation, where the sample should not exceed 30-50 nm in thickness and needs to be electron transparent, thus availability of this technique is limited.

Unless stated otherwise, SEM/EDX analysis was performed with the support of Dr Hayley Andrews (Manchester Metropolitan University, UK). TEM analysis was performed by Geoff Parr (Salford University, UK) and HR-TEM by Kerstin Jurkschat, (University of Oxford, UK).

### *1.6.2 X-Ray Diffraction (XRD)*

X-ray diffraction (XRD) has been utilised to identify phase purity, crystallinity and unit cell dimensions of the synthesised materials, using a PANalytical X'Pertin Powder system in the powder spinning mode at a 2θ range between 20-60°, with a 1° anti-scatter slit and step size of 0.052°, 200s per step.

A XRD system consists of a sample holder, X-ray tube and detector. Generated *via* producing electrons in the cathode ray tube, X-ray beam is first focused into the sample and penetrates many micrometres of the material. Then, when electrons have

sufficient energy to remove inner shell electrons of the targeted material, characteristic spectra is produced, usually called as a 'fingerprint' of the crystal.

Direction of the diffracted X-ray beam is determined by the periodicity of the planes of atoms in the crystal solid. By measuring the angles, under which X-rays are diffracted, the crystal lattice d-spacing is calculated based on Bragg's Law (*Equation 1.1*),[133]

$$n\lambda = 2d\ sin\theta \qquad 1.1$$

where λ corresponds to the wavelength of the incident X-ray beam applied to the crystal surface, θ is the angle of reflection/incidence, which generates the diffracted beam at the same angle and d is the crystal lattice spacing, as shown in *Figure 1.13*. The detector then records and analyses the number of X-ray incident at each angle, followed by its conversion to a count rate. The sensitivity of this technique depends on the material of interest, as it is most sensitive for the elements with high atomic number.[134] Peak position and intensity can be used to investigate lattice constant and stress of studied sample. Also, grain size and degree of crystallisation can be measured by peak angles. In general, sharp and narrow peaks indicate perfect crystals.

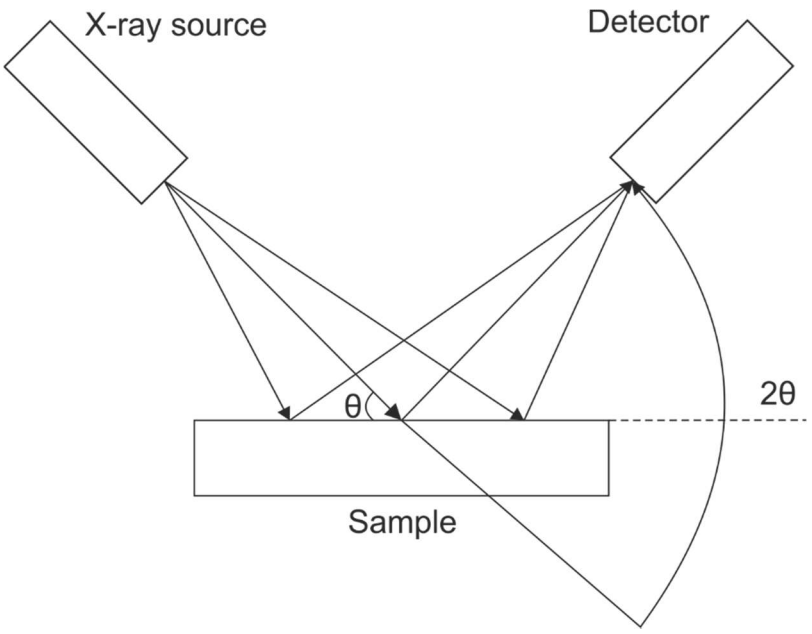


***Figure 1.13*** *Schematic representation of simplified XRD apparatus*

In order to identify the unknown species, the obtained data can be compared with the standard line patterns available for various compounds, stored and updated yearly in the international centre for diffraction data (ICDD).

### *1.6.3 Porosimetry Analysis*

Nitrogen adsorption isotherm analysis has been employed in order to investigate porosity and surface area of obtained materials and was carried out using a Micromeritics ASAP 2020 Surface Analyser at -196ºC. All samples were degassed prior to analysis under vacuum ($p<10^{-3}$ Pa) for 3 hours at 300ºC. Brunauer-Emmett-Teller (BET) surface area was calculated in the relative pressure range 0.05-0.30.

First, the sample is pretreated in order to remove any excess of gas and impurities from the surface of the sample. Then, nitrogen is supplied and adsorbed onto the surface of the material placed in a cryogenic container, and the amount of adsorbed gas is calculated by means of the BET equation (*Equation 1.2*), where $V_a$ is the volume of gas adsorbed at standard temperature and pressure, P is the partial vapour pressure of the adsorbate gas in equilibrium, $P_0$ is the saturated pressure of the adsorbent gas, $V_m$ is the volume of gas adsorbed at standard temperature and pressure to produce an apparent monolayer on the sample surface, and C is a dimensionless constant that is related to the enthalpy of adsorption of the adsorbate gas on the powder sample. Then, the surface area (SA) is calculated (*Equation 1.3*), where M is the molecular weight of adsorbate, $N_A$ is Avogadro's constant ($6.023 \times 10^{23}$ mol$^{-1}$) and $A_{cs}$ is the cross section area required by the adsorbate (for nitrogen $A_{cs}$ = 0.162 nm$^2$).[133]

$$\frac{1}{[V_a\left(\frac{P_0}{P}-1\right)]} = \frac{C-1}{V_m-C} x \frac{P}{P_0} + \frac{1}{V_m C} \qquad 1.2$$

$$SA = \frac{V_m N_A}{M} x A_{cs} \qquad 1.3$$

Subsequently, an adsorption isotherm is generated by the measured amount of gas adsorbed across a wide range of relative pressures at constant temperature. Desorption is also monitored by measuring the gas removed as pressure is reduced.

Moreover, pore size distribution is calculated from experimental isotherms using the Kelvin model of pore filling *via* the Barrett-Joyner Halenda (BJH) equation, which relates the amount of adsorbate removed from the pores of the sample as the relative pressure ($P/P_0$) decreases to the size of the pores.[135] BET technique is non-destructive and is capable of providing information about surface of the material with <0.15% of reading error.

### *1.6.4 Fourier Transform Infrared Spectroscopy (FTIR)*

Fourier transform infrared spectroscopy (FTIR) has been utilised to identify chemical bonding within the molecular components of the materials and was performed using attenuated total reflection (ATR) sampling technique, Nicolet 380 Smart iTR with a diamond detector.

This technique measures infrared radiation of the investigated sample against the wavelength with the resolution up to 0.001 $cm^{-1}$. It can be employed for qualitative and quantitative analysis of the solid material. When the sample is exposed to infrared irradiation, absorbed IR leads to the excitement of the molecule into the higher vibrational states and the wavelength of the absorbed light is characteristic of the specific molecules. The detector within the instrument then quantifies the reflected light as a function of wavelength.[132] It results in a spectrum with the peak characteristics that can readily provide structural information of a molecule.

### *1.6.5 Raman Spectroscopy*

Raman Spectroscopy has been employed to investigate molecular vibrations within the material, using an ''inVia'' confocal Raman Microscope, Reinshaw PLC, equipped with a confocal microscope (x50 objective) with argon laser (514 nm excitation) and a very low laser power (0.8 mW) to avoid heating effects.

Raman Spectroscopy involves pointing a laser as a monochromatic light into the material and the scattered light at the specific frequencies is detected. Most of the scattered light maintains the same energy as when it is introduced with (Rayleigh

scattered); however small fraction of the light changes the energy by exchanging the energy with the molecular vibrations of the molecule (Raman scattered).[136] In the case when the light gains the energy, the Raman scattering is described as 'anti-Stokes', whereas when the energy of the light decreases more intense 'Stokes' scattering is obtained. Raman spectra are plotted in respect to the laser frequency that corresponds to the energy levels of different functional groups present, thus interpretation of data is similar to that of FTIR.[137]

### *1.6.6 Inductively Coupled Plasma Optical Emission Spectrometry (ICP-OES)*

Inductive coupled plasma optical emission spectrometry (ICP-OES) has been used to analyse the total metal composition of the catalysts after ultrasonic extraction in $HNO_3$ (5%) using Thermo Scientific iCAP6300 model.

This technique applies optical emission principles of excited atoms to quantitatively determine the concentration of metals present in the sample. The instrument utilises argon gas that flows through three quartz tubes in order to generate an inductive plasma initiated by a spark from a Tesla coil, which is then coupled with a magnetic field at the end of the torch by passing a high frequency electric current. The liquid sample is nebulised and introduced into the centre of the plasma, where sample atoms get excited and relax by emitting light at a specific wavelength for each element. The intensity of the emitted light is detected and compared to the standards.[133]

Unless stated otherwise, ICP-OES analysis was performed by David McKendry, (Manchester Metropolitan University, UK).

### *1.6.7 Gas Chromatography (GC)*

Gas chromatography (GC) was utilised for the analysis of the products after catalytic reactions, using a Hewlett Packard 5890 series with GS-GASPRO column (60 m x 0.32 mm) connected to a thermal conductivity detector (TCD).

The chromatographic separation involves interactions of the sample with the mobile phase and stationary phase within the column of the GC.

The mobile phase, usually inert gas, slowly carries the sample through the column, which continuously adsorbs and desorbs molecules present in the stationary phase in the column. The affinity of a specific molecule within the stationary phase defines the retention time of the component of the sample in the column. Each constituent travels to the column at the same rate and elutes (exits) within the specific time for the component. Hence, molecules present in the sample exhibit different retention times.[138, 139]

The typical column consists of a tube of small diameter with a thin film of high-molecular weight polymer inside (stationary phase). As each component exits the column, it goes into the detector, in this case a TCD, which contains four identical heated filaments, as shown within *Figure 1.14*.

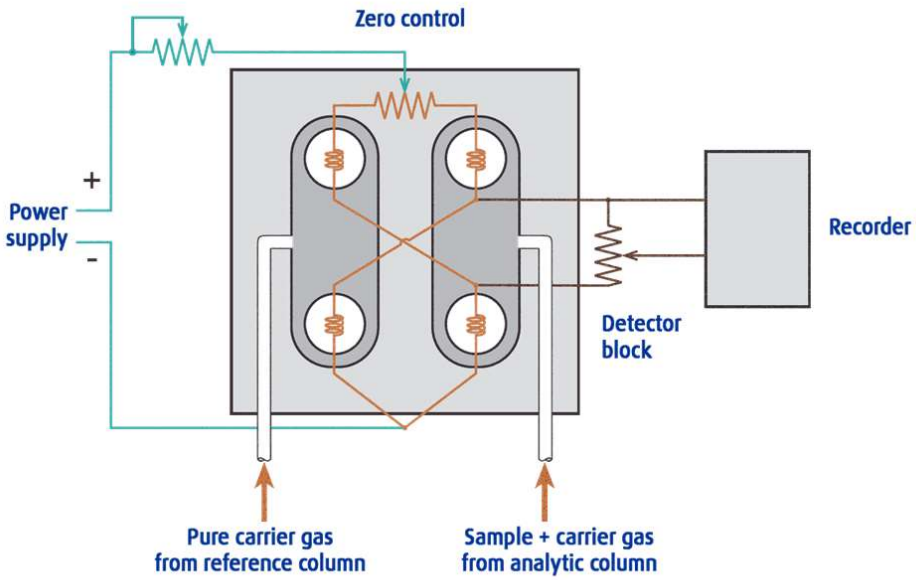


***Figure 1.14*** *Principle of thermal-conductivity detector (TCD), reproduced from reference* [140]

Two filaments analyse the column content whereas another two are placed in the gas stream ahead of the sample injection point, and any imbalance is recorded. Following this principle, the TCD compares the heat rate loss from the filament into the

gas and determines changes within the thermal conductivity of the eluted gas when compared to the carrier gas.

In fact, most of the components have much lower thermal conductivity to that of carrier gas, usually helium, hence eluted analytes produce the detectable signals.[133,140]

### *1.6.8 Thermogravimetric Analysis (TGA)*

Thermogravimetric analysis (TGA) has been conducted to analyse carbon deposition after the performed catalytic reactions, using a Perkin Elmer 4000 instrument heated at 10°C $min^{-1}$ over the ramp of temperatures in 40 mL $min^{-1}$ flowing air.

This technique monitors the loss of the mass of the sample upon heating as a function of time in a controlled atmosphere. It consists of a sample pan that is heated throughout the experiment, and supported by a precision balance. Any weight loss of the sample is detected throughout the ramp of the temperature.[141]

## 1.7 References


1. D. J. Wuebbles and K. Hayhoe, *Earth-Science Reviews*, 2002, **57**, 177-210.
2. S. Faramawy, T. Zaki and A. A. E. Sakr, *Journal of Natural Gas Science and Engineering*, 2016, **34**, 34-54.
3. A. Rojey, N. Marshall and R. N. Maddox, *Natural gas : production, processing, transport*, Editions Technip, Paris, 1997.
4. A. R. Lauder, I. G. Enting, J. O. Carter, N. Clisby, A. L. Cowie, B. K. Henry and M. R. Raupach, *International Journal of Greenhouse Gas Control*, 2013, **12**, 419-429.
5. *Journal*, 1999.
6. T. Gold, *Annual Review of Energy*, 1985, **10**, 53-77.
7. *Fuel and Energy Abstracts*, 2003, **44**, 143.
8. J. G. Speight, in *Shale Gas Production Processes*, Gulf Professional Publishing, Boston, 2013, DOI: https://doi.org/10.1016/B978-0-12-404571-2.00004-2, pp. 101-119.
9. S. M. Hamilton, S. E. Grasby, J. C. McIntosh and S. G. Osborn, *Hydrogeology Journal*, 2015, **23**, 719-739.
10. T. Kanduč, M. Markič, S. Zavšek and J. McIntosh, *International Journal of Coal Geology*, 2012, **89**, 70-83.
11. K. A. Kvenvolden, *Organic Geochemistry*, 1995, **23**, 997-1008.
12. J. Gao, Y. Wang, Y. Ping, D. Hu, G. Xu, F. Gu and F. Su, *RSC Advances*, 2012, **2**, 2358-2368.

13. Y. Li, S. Y. Park and J. Zhu, *Renewable and Sustainable Energy Reviews*, 2011, **15**, 821-826.
14. K. Deivanai, Kasturi and R. Bai, *Bioresource Technology*, 1995, **52**, 93-94.
15. M. Krishania, V. Kumar, V. K. Vijay and A. Malik, *Fuel*, 2013, **106**, 1-9.
16. N. Bardiya, D. Somayaji and S. Khanna, *Bioresource Technology*, 1996, **58**, 73-76.
17. Viridor - transforming waste, http://www.viridor.co.uk/).
18. V. Jaiganesh, P. K. Nagarajan and A. Geetha, *Renewable and Sustainable Energy Reviews*, 2014, **40**, 432-437.
19. *Journal*, 2017.
20. W. Mazyan, A. Ahmadi, H. Ahmed and M. Hoorfar, *Journal of Natural Gas Science and Engineering*, 2016, **30**, 487-514.
21. Where does UK gas come from?, https://www.britishgas.co.uk/the-source/our-world-of-energy/energys-grand-journey/where-does-uk-gas-come-from).
22. S. Kumar, H.-T. Kwon, K.-H. Choi, W. Lim, J. H. Cho, K. Tak and I. Moon, *Applied Energy*, 2011, **88**, 4264-4273.
23. A. Hegab, A. La Rocca and P. Shayler, *Renewable and Sustainable Energy Reviews*, 2017, **70**, 666-697.
24. Semin and R. A. Bakar, *American Journal of Engineering and Applied Sciences*, 2008, **1**, 302-311.
25. T. Korakianitis, A. M. Namasivayam and R. J. Crookes, *Progress in Energy and Combustion Science*, 2011, **37**, 89-112.
26. B. B. Sahoo, N. Sahoo and U. K. Saha, *Renewable and Sustainable Energy Reviews*, 2009, **13**, 1151-1184.
27. J. B. Heywood, *Internal combustion engine fundamentals*, New York, 1988.
28. EU: Heavy-Duty Truck and Bus Engines, https://www.dieselnet.com/standards/eu/hd.php#stds, 2017).
29. J. Shemshad, S. M. Aminossadati and M. S. Kizil, *Sensors and Actuators B: Chemical*, 2012, **171–172**, 77-92.
30. J. H. Park, J. H. Cho, Y. J. Kim, E. S. Kim, H. S. Han and C. H. Shin, *Applied Catalysis B: Environmental*, 2014, **160–161**, 135-143.
31. Q. Gao, Y. Zhang, J. Yu, S. Wu, Z. Zhang, F. Zheng, X. Lou and W. Guo, *Sensors and Actuators A: Physical*, 2013, **199**, 106-110.
32. C. P. C. Bong, L. Y. Lim, W. S. Ho, J. S. Lim, J. J. Klemeš, S. Towprayoon, C. S. Ho and C. T. Lee, *Journal of Cleaner Production*, 2017, **146**, 149-157.
33. A. M. Thompson, K. B. Hogan and J. S. Hoffman, *Atmospheric Environment. Part A. General Topics*, 1992, **26**, 2665-2668.
34. S. Anand, R. P. Dahiya, V. Talyan and P. Vrat, *Environment International*, 2005, **31**, 469-482.
35. H. Wu, J. Zhang, H. H. Ngo, W. Guo and S. Liang, *Journal of Cleaner Production*, 2017, **147**, 152-156.
36. C. Maucieri, A. C. Barbera, J. Vymazal and M. Borin, *Agricultural and Forest Meteorology*, 2017, **236**, 175-193.
37. A. Olajossy, *International Journal of Mining Science and Technology*, 2017, **27**, 321-326.
38. C. Martins, P. M. Fearnside, A. Gomes Bandeira and R. Wassmann, *Chemosphere*, 1996, **33**, 517-536.
39. F. A. E. Roland, F. Darchambeau, C. Morana, S. Bouillon and A. V. Borges, *Chemosphere*, 2017, **168**, 756-764.
40. A. Vasileva and K. Moiseenko, *Atmospheric Environment*, 2013, **71**, 115-121.
41. M. J. Ortiz-Llorente and M. Alvarez-Cobelas, *Atmospheric Environment*, 2012, **59**, 328-337.

42. K. R. Newman, M.-H. Cormier, J. K. Weissel, N. W. Driscoll, M. Kastner, E. A. Solomon, G. Robertson, J. C. Hill, H. Singh, R. Camilli and R. Eustice, *Earth and Planetary Science Letters*, 2008, **267**, 341-352.
43. R. O. Yusuf, Z. Z. Noor, A. H. Abba, M. A. A. Hassan and M. F. M. Din, *Renewable and Sustainable Energy Reviews*, 2012, **16**, 5059-5070.
44. L. Chapman, *Journal of Transport Geography*, 2007, **15**, 354-367.
45. R. P. Wayne, in *Low-Temperature Chemistry of the Atmosphere*, eds. G. K. Moortgat, A. J. Barnes, G. Le Bras and J. R. Sodeau, Springer Berlin Heidelberg, Berlin, Heidelberg, 1994, DOI: 10.1007/978-3-642-79063-8_2, pp. 21-48.
46. M. A. H. Khan, M. M. N. Hoque, S. S. Alam, M. J. Ashfold, G. Nickless and D. E. Shallcross, *Journal of Environmental Sciences*, 2011, **23**, 60-64.
47. K. Kaiho and S. Koga, *Global and Planetary Change*, 2013, **107**, 91-101.
48. *Journal*, 2008.
49. R. Horn and R. Schlögl, *Catalysis Letters*, 2015, **145**, 23-39.
50. Y. Masuyama, Y. Sugioka, S. Chonan, N. Suzuki, M. Fujita, K. Hara and A. Fukuoka, *Journal of Molecular Catalysis A: Chemical*, 2012, **352**, 81-85.
51. Y. Feng, H. Yin, D. Gao, A. Wang, L. Shen and M. Meng, *Journal of Catalysis*, 2014, **316**, 67-77.
52. Z. Liu, Q. Shi, R. Zhang, Q. Wang, G. Kang and F. Peng, *Journal of Power Sources*, 2014, **268**, 171-175.
53. M. Rotko, A. Machocki and G. Slowik, *Applied Catalysis B-Environmental*, 2014, **160**, 298-306.
54. I. H. Son, S. J. Lee, I. Y. Song, W. S. Jeon, I. Jung, D. J. Yun, D. W. Jeong, J. O. Shim, W. J. Jang and H. S. Roh, *Fuel*, 2014, **136**, 194-200.
55. P. Gélin and M. Primet, *Applied Catalysis B: Environmental*, 2002, **39**, 1-37.
56. M. Lyubovsky and L. Pfefferle, *Catalysis Today*, 1999, **47**, 29-44.
57. S. Sokolov, J. Radnik, M. Schneider and U. Rodemerck, *International Journal of Hydrogen Energy*, DOI: http://dx.doi.org/10.1016/j.ijhydene.2017.01.013.
58. T. R. Baldwin and R. Burch, *Applied Catalysis*, 1990, **66**, 359-381.
59. K. Tao, L. Shi, Q. Ma, D. wang, C. Zeng, C. Kong, M. Wu, L. Chen, S. Zhou, Y. Hu and N. Tsubaki, *Chemical Engineering Journal*, 2013, **221**, 25-31.
60. L. Zhou, Y. Guo, H. Kameyama and J.-M. Basset, *International Journal of Hydrogen Energy*, 2014, **39**, 7291-7305.
61. J. Au-Yeung, K. Chen, A. T. Bell and E. Iglesia, *Journal of Catalysis*, 1999, **188**, 132-139.
62. C. Shi and P. Zhang, *Applied Catalysis B: Environmental*, 2012, **115**, 190-200.
63. T. Guo, J. Du, J. Wu, S. Wang and J. Li, *Chemical Engineering Journal*, 2016, **306**, 745-753.
64. S. Okada, R. Manabe, R. Inagaki, S. Ogo and Y. Sekine, *Catalysis Today*, DOI: https://doi.org/10.1016/j.cattod.2017.05.079.
65. Q. Huang, W. Li, Q. Lin, X. Zheng, H. Pan, D. Pi, C. Shao, C. Hu and H. Zhang, *Journal of the Energy Institute*, DOI: https://doi.org/10.1016/j.joei.2017.05.008.
66. M. M. Barroso-Quiroga and A. E. Castro-Luna, *International Journal of Hydrogen Energy*, 2010, **35**, 6052-6056.
67. J.-S. Chang, D.-Y. Hong, X. Li and S.-E. Park, *Catalysis Today*, 2006, **115**, 186-190.
68. Z. Hao, Q. Zhu, Z. Jiang, B. Hou and H. Li, *Fuel Processing Technology*, 2009, **90**, 113-121.
69. S. Tomiyama, R. Takahashi, S. Sato, T. Sodesawa and S. Yoshida, *Applied Catalysis A: General*, 2003, **241**, 349-361.
70. H. Y. Wang and E. Ruckenstein, *Applied Catalysis A: General*, 2000, **204**, 143-152.

71. R. Kumar Singha, A. Shukla, A. Yadav, S. Sain, C. Pendem, L. N. S. Kumar Konathala and R. Bal, *Molecular Catalysis*, 2017, **432**, 131-143.
72. S. M. Stagg-Williams, F. B. Noronha, G. Fendley and D. E. Resasco, *Journal of Catalysis*, 2000, **194**, 240-249.
73. A. D. Ballarini, S. R. de Miguel, E. L. Jablonski, O. A. Scelza and A. A. Castro, *Catalysis Today*, 2005, **107**, 481-486.
74. L. F. Liotta, G. Di Carlo, G. Pantaleo and G. Deganello, *Catalysis Communications*, 2005, **6**, 329-336.
75. Z. Hao, Q. Zhu, Z. Jiang and H. Li, *Powder Technology*, 2008, **183**, 46-52.
76. H. Y. Wang and E. Ruckenstein, *Applied Catalysis A: General*, 2001, **209**, 207-215.
77. P. Djinović, I. G. O. Črnivec, J. Batista, J. Levec and A. Pintar, *Chemical Engineering and Processing: Process Intensification*, 2011, **50**, 1054-1062.
78. L. Zhou, L. R. Enakonda, M. Harb, Y. Saih, A. Aguilar-Tapia, S. Ould-Chikh, J.-l. Hazemann, J. Li, N. Wei, D. Gary, P. Del-Gallo and J.-M. Basset, *Applied Catalysis B: Environmental*, 2017, **208**, 44-59.
79. L. Tang, D. Yamaguchi, N. Burke, D. Trimm and K. Chiang, *Catalysis Communications*, 2010, **11**, 1215-1219.
80. H.-C. Wu, L.-C. Liu and S.-M. Yang, *Applied Catalysis A: General*, 2001, **211**, 159-165.
81. T. Sugaya, A. Ishikawa, S. i. Komai, A. Satsuma, T. Hattori and Y. Murakami, in *Advanced Materials '93*, Elsevier, 1994, DOI: http://dx.doi.org/10.1016/B978-1-4832-8380-7.50031-6, pp. 103-106.
82. K. Tõnsuaadu, K. A. Gross, L. Plūduma and M. Veiderma, *Journal of Thermal Analysis and Calorimetry*, 2012, **110**, 647-659.
83. F. Ren, X. Lu and Y. Leng, *Journal of the Mechanical Behavior of Biomedical Materials*, 2013, **26**, 59-67.
84. V. Uskoković and D. P. Uskoković, *Journal of Biomedical Materials Research Part B: Applied Biomaterials*, 2011, **96B**, 152-191.
85. F. Yao, J. P. LeGeros and R. Z. LeGeros, *Acta Biomaterialia*, 2009, **5**, 2169-2177.
86. T. Kawasaki, M. Niikura and Y. Kobayashi, *Journal of Chromatography A*, 1990, **515**, 91-123.
87. D. Bellucci, A. Sola, M. Gazzarri, F. Chiellini and V. Cannillo, *Materials Science and Engineering: C*, 2013, **33**, 1091-1101.
88. M. Šupová, *Ceramics International*, 2015, **41**, 9203-9231.
89. S. V. Dorozhkin, *Biomaterials*, 2010, **31**, 1465-1485.
90. H. P. Wiesmann, U. Plate, K. Zierold and H. J. Höhling, *Journal of Dental Research*, 1998, **77**, 1654-1657.
91. B. S. Moonga and D. W. Dempster, *Journal of Bone and Mineral Research*, 1995, **10**, 453-457.
92. S. Kongsri, K. Janpradit, K. Buapa, S. Techawongstien and S. Chanthai, *Chemical Engineering Journal*, 2013, **215–216**, 522-532.
93. M. Vila, S. Sánchez-Salcedo and M. Vallet-Regí, *Inorganica Chimica Acta*, 2012, **393**, 24-35.
94. N. Gupta, A. K. Kushwaha and M. C. Chattopadhyaya, *Journal of the Taiwan Institute of Chemical Engineers*, 2012, **43**, 125-131.
95. T. A. Salah, A. M. Mohammad, M. A. Hassan and B. E. El-Anadouli, *Journal of the Taiwan Institute of Chemical Engineers*, 2014, **45**, 1571-1577.
96. Y. Zhang, Y. Liu, X. Ji, C. E. Banks and W. Zhang, *Materials Letters*, 2012, **78**, 120-123.
97. Q. Zhang, Y. Liu, Y. Zhang, H. Li, Y. Tan, L. Luo, J. Duan, K. Li and C. E. Banks, *Analyst*, 2015, **140**, 5235-5242.
98. S. K. Ghosh, S. K. Roy, B. Kundu, S. Datta and D. Basu, *Materials Science and Engineering: B*, 2011, **176**, 14-21.

99. S. K. Padmanabhan, A. Balakrishnan, M. C. Chu, Y. J. Lee, T. N. Kim and S. J. Cho, *Particuology*, 2009, **7**, 466-470.
100. K. Mori, T. Hara, T. Mizugaki, K. Ebitani and K. Kaneda, *Journal of the American Chemical Society*, 2004, **126**, 10657-10666.
101. A. Indra, C. S. Gopinath, S. Bhaduri and G. Kumar Lahiri, *Catalysis Science & Technology*, 2013, **3**, 1625-1633.
102. D. Özhava and S. Özkar, *International Journal of Hydrogen Energy*, 2015, **40**, 10491-10501.
103. M. Gruselle, *Journal of Organometallic Chemistry*, 2015, **793**, 93-101.
104. N. Cheikhi, M. Kacimi, M. Rouimi, M. Ziyad, L. F. Liotta, G. Pantaleo and G. Deganello, *Journal of Catalysis*, 2005, **232**, 257-267.
105. D. Miao, A. Goldbach and H. Xu, *ACS Catalysis*, 2016, **6**, 775-783.
106. S. Sugiyama, T. Minami, H. Hayashi, M. Tanaka and J. B. Moffat, *Journal of Solid State Chemistry*, 1996, **126**, 242-252.
107. C. Boucetta, M. Kacimi, A. Ensuque, J.-Y. Piquemal, F. Bozon-Verduraz and M. Ziyad, *Applied Catalysis A: General*, 2009, **356**, 201-210.
108. J. H. Park, D.-W. Lee, S.-W. Im, Y. H. Lee, D.-J. Suh, K.-W. Jun and K.-Y. Lee, *Fuel*, 2012, **94**, 433-439.
109. S. C. Oh, Y. Wu, D. T. Tran, I. C. Lee, Y. Lei and D. Liu, *Fuel*, 2016, **167**, 208-217.
110. N. Takarroumt, M. Kacimi, F. Bozon-Verduraz, L. F. Liotta and M. Ziyad, *Journal of Molecular Catalysis A: Chemical*, 2013, **377**, 42-50.
111. D. Chlala, M. Labaki, J.-M. Giraudon, O. Gardoll, A. Denicourt-Nowicki, A. Roucoux and J.-F. Lamonier, *Comptes Rendus Chimie*, 2016, **19**, 525-537.
112. Z. Qu, Y. Sun, D. Chen and Y. Wang, *Journal of Molecular Catalysis A: Chemical*, 2014, **393**, 182-190.
113. Z. Boukha, J. González-Prior, B. d. Rivas, J. R. González-Velasco, R. López-Fonseca and J. I. Gutiérrez-Ortiz, *Applied Catalysis B: Environmental*, 2016, **190**, 125-136.
114. Z. Opre, J. D. Grunwaldt, M. Maciejewski, D. Ferri, T. Mallat and A. Baiker, *Journal of Catalysis*, 2005, **230**, 406-419.
115. Z. Opre, D. Ferri, F. Krumeich, T. Mallat and A. Baiker, *Journal of Catalysis*, 2006, **241**, 287-295.
116. K. Zhao, B. Qiao, J. Wang, Y. Zhang and T. Zhang, *Chemical Communications*, 2011, **47**, 1779-1781.
117. J. H. Jun, T.-J. Lee, T. H. Lim, S.-W. Nam, S.-A. Hong and K. J. Yoon, *Journal of Catalysis*, 2004, **221**, 178-190.
118. J. H. Jun, T. H. Lim, S.-W. Nam, S.-A. Hong and K. J. Yoon, *Applied Catalysis A: General*, 2006, **312**, 27-34.
119. Z. Boukha, M. Kacimi, M. Ziyad, A. Ensuque and F. Bozon-Verduraz, *Journal of Molecular Catalysis A: Chemical*, 2007, **270**, 205-213.
120. B. Yan, L.-Z. Tao, Y. Liang and B.-Q. Xu, *ACS Catalysis*, 2014, **4**, 1931-1943.
121. V. C. Ghantani, S. T. Lomate, M. K. Dongare and S. B. Umbarkar, *Green Chemistry*, 2013, **15**, 1211-1217.
122. J. T. Kozlowski and R. J. Davis, *ACS Catalysis*, 2013, **3**, 1588-1600.
123. L. Silvester, J.-F. Lamonier, J. Faye, M. Capron, R.-N. Vannier, C. Lamonier, J.-L. Dubois, J.-L. Couturier, C. Calais and F. Dumeignil, *Catalysis Science & Technology*, 2015, **5**, 2994-3006.
124. T. Tsuchida, T. Yoshioka, S. Sakuma, T. Takeguchi and W. Ueda, *Industrial & Engineering Chemistry Research*, 2008, **47**, 1443-1452.
125. K. H. Kim, S. Y. Lee and K. J. Yoon, *Korean Journal of Chemical Engineering*, 2006, **23**, 356-361.

126. S. Sugiyama, T. Minami, H. Hayashi, M. Tanaka, N. Shigemoto and J. B. Moffat, *Energy & Fuels*, 1996, **10**, 828-830.
127. S. Sugiyama, T. Minami, T. Moriga, H. Hayashi, K. Koto, M. Tanaka and J. B. Moffat, *Journal of Materials Chemistry*, 1996, **6**, 459-464.
128. S. Sugiyama, T. Minami, T. Moriga, H. Hayashi and J. B. Moffat, *Journal of Solid State Chemistry*, 1998, **135**, 86-95.
129. S. Sugiyama, Y. Iguchi, H. Nishioka, T. Minami, T. Moriga, H. Hayashi and J. B. Moffat, *Journal of Catalysis*, 1998, **176**, 25-34.
130. Z. Boukha, M. Kacimi, M. F. R. Pereira, J. L. Faria, J. L. Figueiredo and M. Ziyad, *Applied Catalysis A: General*, 2007, **317**, 299-309.
131. J. C. D. Brand, *Lines of Light: The Sources of Dispersive Spectroscopy, 1800-1930*, Gordon & Breach Publ., 1995.
132. K. F. Lim and S. W. Lewis, in *Encyclopedia of Forensic Sciences*, ed. J. A. S. J. S. M. Houck, Academic Press, Waltham, 2013, DOI: http://dx.doi.org/10.1016/B978-0-12-382165-2.00255-5, pp. 627-634.
133. W. Merritt and D. Settle, *Instrumental Methods of Analysis*, CBS Publishers & Distributors, India, 7th edition edn., 1986.
134. J. Kulczyk-Malecka, PhD Thesis, Manchester Metropolitan University, 2014.
135. A. M. Valenzuela-Muniz, presented in part at the Russ College of Engineering and Technology, 2012.
136. V. Z. Williams, *Journal of Chemical Education*, 1945, **22**, 572.
137. M. J. Pelletier, *Analytical Applications of Raman Spectroscopy*, Blackwell Science Ltd, Oxford, 1999.
138. T. D. Rapson and H. Dacres, *TrAC Trends in Analytical Chemistry*, 2014, **54**, 65-74.
139. J. Kamieniak, E. P. Randviir and C. E. Banks, *TrAC Trends in Analytical Chemistry*, 2015, **73**, 146-157.
140. Thermal conductivity detector (TCD), http://hiq.linde-gas.com/en/analytical_methods/gas_chromatography/thermal_conductivity_detector.html, (accessed 10/05/2017).
141. T. Wang, A. Dorner-Reisel and E. Müller, *Journal of the European Ceramic Society*, 2004, **24**, 693-698.

# Chapter 2: Preparation of Hydroxyapatite: Synthesis of the Support of the Catalyst

# 2.1 Introduction

In this chapter, the utilisation of less toxic components in the synthetic route for the synthesis of HAP *via* a wet chemical precipitation method without any template was first studied. Then, a soft-template approach was also explored, with the assistance of three different surfactants, and its influence on the porosity and crystallinity on the resulting HAP was investigated. Furthermore, carbon nanorods (CNRs) were synthesised using three different silica templates and were further employed for the first time as a hard-template to enhance the porosity of HAP. Full characterisation of all prepared materials, including templates as well as HAP, was performed in order to analyse their characteristic features and morphology. Results within this chapter have been published in Catalysts, 2016, 6(8), 119; Ceramics International, 2017, 43(7), 5412-5416 and Catalysis Letters, 2017, 147(8), 2200-2208.

## *2.1.1 Typical synthetic routes for HAP*

The synthesis of hydroxyapatite have been extensively studied by researchers from different fields. The physicochemical properties of HAP are highly sensitive to the preparation technique and small changes to the technique can lead to significant changes in these properties, therefore it still remains a subject of scrutiny. Hence, over the past two decades, a variety of different procedures have been developed to synthesise HAP, including wet chemical[1-3], sol-gel[4], hydrolysis[5], microwave irradiation[6], hydrothermal methods[7-9], spray pyrolysis[10], emulsion processing[11], solid state[12], electrospraying[13], electrospinning[14], mechanochemical[15], plasma deposition[16] and flux-cooling method[17]. All reported methods, however, carry advantages as well as disadvantages due to the aforementioned highly sensitive process of formation of HAP. For example, the mechanochemical protocol allows the stoichiometry of the final product to be precisely fixed, but long reaction times and high annealing temperatures are the main downside.[18]

On the other hand, the major disadvantage of a solid state methodology lies in the difficulty of producing uniform nano-sized particles by this means, yet non-uniform crystals favour biological responses, hence such a feature is desirable for biomedical applications.[19]

In view of that, finding the optimum conditions for controllable synthesis of HAP with a specific morphology and crystallinity presents a worthwhile research challenge.[20] Nevertheless, most of the stated techniques require complicated setups, such as reflux or autoclave systems that involve high temperatures and pressures; thus, due to its low cost, simplicity and reduced energy consumption the most utilised procedure is wet chemical precipitation. This methodology involves the direct precipitation of HAP particles from the solution or suspension of $Ca^{2+}$ and $HPO_4^{2-}$ precursor salts. Moreover, during this protocol, HAP forms crystals with high edge free surface/interfacial energies, that is indicative of the difficulty of its formation. A direct experimental result of such tension is a wide distribution of particle sizes, specifically attributed to an aggregation mechanism of crystal growth, highly irregular particle shapes as well as slow crystallisation, which causes an overlap between diffusional crystal growth and nucleation.

In fact, the morphological and chemical properties of HAP formed *via* a wet chemical approach can be tailored by variations of the synthesis conditions, such as temperature, pressure, pH and rate of reagent addition.[21] To maintain a stable pH during the precipitation process, a number of different solvents have been explored in the literature. However, as presented in *Table 2.1*, most of them involve toxic substrates that can cause environmental damage as well as introduce impurities into the final product. Thus there is a need to employ simpler, cheaper and more environmental friendly substrates to control pH throughout the synthesis.

***Table 2.1*** *Different approaches for wet chemical synthesis of HAP reported in the literature, including solvents employed and yields where applicable*

| Solvent used to maintain pH during the synthesis | Yield % | Comments | Time | Temperature of synthesis / °C | Reference |
|---|---|---|---|---|---|
| **Tris hydroxyl methyl amino methane** | 27-36 | - | Not stated | 300-500 | [22] |
| **Ammonia** | Not stated | Yield stated as high, however no specific value mentioned | ~30 hours | 37 | [23] |
| **Ammonia** | >75 | Starch used to prevent agglomeration of nanoparticles | ~40 hours | 85 | [24] |
| **Potassium hydroxide** | Not stated | Yield stated as high, however no specific value mentioned | ~30 hours | 70 | [25] |
| **Ammonia** | Not stated | Yield not stated | ~8 days | 25-100 | [26] |
| **Orthophosphoric acid** | Not stated | Yield not stated | ~30 hours | 18-22 | [18] |
| **Ammonia and deionised water** | Not stated | Yield not stated | >70 hours | 18-22 | [27] |
| **Ammonia** | Not stated | Yield not stated | ~50 hours | 95 | [28] |
| **Ammonia** | Not stated | Yield not stated | ~40 hours | 18-22 | [29] |
| **Phosphoric acid** | Not stated | Yield not stated | ~80 hours | 18-22 | [30] |

All chemical methods utilise synthetic chemicals that typically involve calcium and phosphate as the main reaction components. However, due to the similar structure of HAP to that of bone tissue, different natural waste products with high calcium content have been under investigation recently to synthesise HAP to replace synthetic calcium precursors, such as fish scale[31], gypsum[32], mussel shells[33], oyster shell[34, 35], eggshells[2, 36] or fruit waste[7].

### *2.1.2 Utilisation of templates during the synthesis of HAP*

Besides the aforementioned synthesis conditions, to obtain tunable sizes, shapes and pore structures of HAP, numerous other additives in the precipitation process have been studied, which are divided into soft-templates and hard-templates, according to their different structures. The utilisation of templates during synthesis has been developed since the 1990s and is an easy protocol to implement.[37] The most generalised definition of a template is a pattern to replicate letters, shapes or designs.[38] In another words, it is particular molecule, which helps to generate or design porosity in the matrix, thus it is a structure directing agent. The synthesis route when utilising a template is generally divided into three steps. The first step involves the preparation of the template, followed by a common synthetic approach *i.e.* wet chemical precipitation, under the function of a template. Finally, the template is removed with an appropriate method so that the obtained physical and chemical properties of targeted material are not affected. Depending on the desired properties of the synthesised material, different templates can be utilised.

Hard-templates are stable and rigid materials that directly determine the morphology and size of the particles. Because of their special structure and very specific effect on particle size, they play an important role in many different fields and are usually employed for the synthesis of materials with the shape of nanorods, nanowires, nanotubes and nanobelts.[37] Numerous hard-templates have been developed, such as porous carbon, polymer microspheres, ion exchange resin, anodic aluminium oxide or porous silicates which include MCM-41, MCM-48 and SBA-15. During syn-

thesis, the special structure of a hard-template significantly restricts the crystallisation or aggregation of the material after its surface or pores are filled with the precursor, which now exhibits the opposite features to that of the template after its removal.[37] In another words, to obtain nanorod shaped materials, the required template needs to exhibit nanotube features, *etc*. However, in many cases the utilisation of hard-templates leads to the collapse of part of the pore structure after template removal, affecting the performance of the product in its application.

On the other hand, soft-templates do not exhibit fixed rigid structures. During synthesis, due to intermolecular and intramolecular interaction forces, an aggregate is formed that possesses certain structural features. Then, using these aggregates, inorganic species are deposited onto its surface forming specific shapes and particle sizes. The most common soft-templates involve surfactants, polymers and biopolymers and the main advantage of utilising them is their good reproducibility and simplicity. Nevertheless, the main downside of soft-templates is their poor stability and the fact, that they require certain synthetic systems, where the precursor must be able to form a strong interaction with the template, which consequently needs to form a stable structure that will not collapse after the removal of the template.

Surfactants are amphiphilic molecules that are capable of forming ordered micelles, vesicles or polymers by van der Waals or/and ionic forces.[37] They consist of hydrophilic, polar 'heads' and hydrophobic, non-polar 'tails', that are organised within its structure *via* self-assembly. The hydrophobic component of the surfactant can solubilise organic species, while the hydrophilic species interact with charged inorganic precursors to direct the formation of the inorganic framework.[38] In the aqueous media, at the concentration when the surface is saturated with the surfactant, which is called the Critical Micelle Concentration (CMC), each component interacts with its favoured environment forming micelles that condense and create the template, shown later in *Figure 2.7*. Surfactants can be generally divided into ionic and non-ionic, depending upon the dissociation of the surfactant molecule in aqueous media. Ionic surfactants dissociate in water into anion or cation (anionic or cationic surfactants, respectively) and non-ionic do not dissociate because their hydrophilic component is non-dissociable *e.g.* alcohol, ether or amide.[38]

For the sake of attaining the structural features in HAP synthesis, different soft-templates have been explored, such as cetyltrimethyl ammonium bromide (CTAB)[39], nonaoxyethylene dodecyl ether ($C_{12}EO_9$)[40], polyoxyethylene(20) sorbitan monostearate (Tween 60)[40] and poly(acrylic acid)[41].

### *2.1.3 Mechanism of formation of HAP via wet chemical precipitation*

The exact mechanism of the formation of HAP during the precipitation method is still subject to uncertainty. However, this process is known to be highly sensitive and the chemical pathways leading to the formation of HAP as the final and only phase present are subject to change, depending on the mildest modification of the initial experimental conditions. Thus, it attracts extreme attention to fully understand the mechanism behind it.[42]

In accordance to Ostwald-Lussac's rule, which predicts the highest nucleation rate for the least stable phase for which the supersaturation limit is exceeded under given conditions, amorphous calcium orthophosphate (CAP) is most likely to precipitate first under most circumstances, followed by phase transformation to octacalcium phosphate (OCP) and finally to HAP. It also implies that the secondary phase present may be $Ca(OH)_2$ or tricalcium phosphate (TCP), depending on the exact stoichiometric ratio between Ca and P. The reason for this behaviour is that the thermodynamic barrier posed between the state occupied by dissolved ionic species and the solid phase will be the lowest for the thermodynamically most unstable phase *i.e.* most soluble phase.

Furthermore, an important contributor to this effect is the surface/interfacial energy, which is the work that is necessary to enhance the surface area of a substance by one area unit. Thus it creates a difficulty to overcome when the solid phase is formed. In fact, the amorphous phase is less ordered and hence will have a lower interfacial energy than the crystalline phase, it is, therefore, favourable to be precipitated first, prior to phase transformation into the more stable and crystalline HAP. Furthermore, there is more evidence collected recently to support the theory of growth of crystals *via* linking and reorganising amorphous precursors.[43]

It is interesting to note, that according to the rule first reported by Ostwald, when a substance begins to separate from the solution and makes its first appearance as a new phase, it always makes its appearance as a liquid first. Invoking this mechanism, it is accepted that HAP forms through aggregation of subunits. Subsequently, the large number of phase compositions, *i.e.* stages of which the precipitate has to pass through before reaching HAP symmetry, implies that the formation of the HAP crystals is expected to proceed in many steps.[42]

One of the major parameters to control and optimise the formation of HAP is the pH during the synthesis because of its influence on the amount of free hydroxyl groups and phosphate species available for the reaction. Shifting to a lower pH causes a decrease in the concentration of OH groups and, at the same time, shifts the balance of phosphate species from $PO_4^{3-}$ to $HPO_4^{2-}$ to $H_2PO^{4-}$ and finally $H_3PO_4$. In other words, with lower pH more phosphate groups are protonated and this leads to precipitation becoming less favoured.[42]

On the other hand, the solubility of the transitory phases are also influenced by variations of the pH. It has been shown that OCP is the more stable phase above pH 6.7 and OCP is accepted as being a transient phase in the precipitation of HAP. According to Ostwald-Lussac's rule, in consequence this implies that the transformation of the amorphous phase to HAP follows the OCP→ dicalcium phosphate dihydydrate (DCPD)→HAP route at a pH lower than 6.7 and DCPD→OCP→HAP at a pH>6.7. In fact, formation of the amorphous phase is accompanied by a mild decrease in pH due to higher alkalinity of $Ca^{2+}$ ions when compared to the acidity of the phosphate species. Subsequently, the formation of HAP is followed by a more significant drop of pH caused by $OH^-$ ions being incorporated in the crystal lattice.

The first stage of pH change is similar to the first mild slope in pH and is assigned to stabilisation of the final phase transformation.[44, 45] On the other hand, pH drop during the precipitation of HAP is in agreement with the chemical reaction that takes place during this process. Specifically, for each unit cell of HAP formed, eight protons are released into the solution (*Equation 2.1*).

$$10Ca^{2+} + 6HPO_4^{2-} + 2H_2O \rightarrow Ca_{10}(PO_4)_6(OH)_2 + 8H^+ \qquad 2.1$$

It is also assumed that, as the amorphous phase matures at a stable pH and its molar ratio of Ca/P adjusts to the values that correspond to stoichiometry of HAP, the transformation process will occur faster at higher pH in the range of 7 to 10. Finally, however, it is still unclear if the aforementioned phase transformations take place *via* an internal structural rearrangement of a metastable phase or by dissolution followed by re-precipitation.[42]

The other important parameter during the formation of HAP is the Ca/P ratio. As described before, stoichiometric HAP exhibits a molar ratio between Ca and P equal to 1.67. Hence, different initial Ca/P ratios present in the solution may trigger the formation of a secondary phase or specific phase combination and induce particular pathway in the phase transformation. Ca/P ratios lower than 1.5 would require the removal of two calcium atoms from the stoichiometric HAP followed by protonation of two phosphate groups, hence $Ca_8(HPO_4)_2(PO_4)_4$ would be formed with an empty halide and hydroxyl groups to maintain hexagonal structure, which requires charge neutrality.[46, 47]

Additionally, the mixing rate of the precursors involved in the precipitation of HAP is also crucial. Minor changes in the rate at which the reactants are introduced to each other can often have a drastic effect on the identity of the precipitate. In other words, immediate mixing can lead to irreversible formation of nuclei and premature precipitation under uncontrolled reaction conditions. The classical nucleation theory suggests that, when the induction time is reduced, nucleation density is increased by lowered interfacial tension in the solution.[48] Hence, it is important to maintain a low rate at which the reactants are mixed to precipitate HAP.

# 2.2 Experimental

## *2.2.1 Template free synthesis of HAP*

$(NH_4)_2HPO_4$ (0.4 M, 100 mL) was stirred at room temperature (18–22°C) in a 2 L beaker with $Ca(NO_3)_2$ (0.6 M, 100 mL) added dropwise over one hour, resulting in a "milky" suspension of HAP. The Ca/P molar ratio was kept at 1.67, corresponding to stoichiometric HAP. The pH was maintained through the addition of NaOH (0.1 M) within the range 9.4–9.5. This "milky" suspension was then stirred overnight at room temperature using a magnetic stirring bar.

The obtained precipitate was filtered, cleaned three times alternately with water and ethanol, dried in an oven at 65°C for 6 hours, and then calcined at 550°C for a further 2 hours, making full synthesis complete within less than 24 hours.

## *2.2.2 Fabrication of HAP via Soft-template approach*

To synthesise mesoporous HAP different soft-templates were employed, such as cetyl trimethylammonium bromide (CTAB, 8.74 g), polyoxyethylene(20) sorbitan monostearate (Tween 60, 26.0 g), nonaoxyethylene dodecyl ether ($C_{12}EO_9$, 10.66g) or a mixture of Tween 60 and $C_{12}EO_9$.[40] $Ca(NO_3)_2$ (7.88 g) was mixed with $KH_2PO_4$ (2.72 g), dissolved in deionised water (26.6 mL) and acidified by concentrated $HNO_3$ (13.60 mL) to avoid precipitation of $Ca_2(PO_4)_3$. This acidic solution was then added to a template and heated to 60°C with stirring until a clear solution was formed. The solution was cooled to room temperature and treated with NaOH (0.1 M) added dropwise to precipitate HAP at a basic pH of around 9.4-9.5. The suspension was stirred overnight, filtered, washed with ethanol and water, dried and calcined in air for 5 hours at 550°C.

## 2.2.3 Utilisation of Hard-templates for HAP synthesis

### 2.2.3.1 Carbon nanorods

To synthesise carbon nanorods (CNRs), several highly ordered and mesoporous silicates were utilised, such as SBA-15, MCM-41 and MCM-48. The SBA-15 was synthesised and provided by Dr Talib Albayati, University of Technology in Baghdad, Iraq, and the method was as follows. Pluronic P123 (structure-directing agent, 6.0 g) was dissolved into a solution of deionised water (45 mL) and HCl (180 g, 2M), followed by stirring at 35–40°C for 20 mins. Then, tetraethyl orthosilicate (TEOS, 12.8 g) was added and the solution was stirred continuously for a further 20 hours. The entire contents were then transferred into a PTFE bottle and the mixture was aged for a further 24 hours at 90°C under static conditions. The resulting white powder was filtered and purified *via* washing with ethanol and deionized water. The product was calcined at 550°C for 12 hours using a heating ramp rate of 2°C $min^{-1}$.

Another silica template, MCM-41, was synthesised by dissolving cetyl trimethylammonium bromide (CTAB, 10 g) together with NaOH (1.0 g) in deionised water (90.0 mL) producing a clear solution. Next, TEOS (11.0 mL) was added and the mixture was heated up to 35°C and stirred at this temperature for 30 mins, during which time a white precipitate formed, which was then filtered, washed with deionised water, dried and calcined at 550°C for 5 hours using a ramp rate of 2°C $min^{-1}$.

Finally, MCM-48 was synthesised following the same procedure as MCM-41, but instead of filtration of the precipitate that formed, the entire content was placed in a PTFE lined stainless steel autoclave and heated under static conditions for 24 hours at 150°C. The autoclave was cooled down to room temperature under a flow of cold water. The white precipitate obtained, MCM-48, was then recovered by filtration and washed with deionised water, dried and calcined at 550°C for 5 hours using a ramp rate of 2°C $min^{-1}$.

To synthesise CNRs, the calcined silica template (1.0 g) was impregnated with an aqueous solution containing sucrose (1.25 g), concentrated $H_2SO_4$ (78.9 µL) and deionised water (5.0 mL).

The mixture was placed in a drying oven for 6 hours at 100°C and a further 6 hours at 160°C. The sample, which turned dark brown due to partially carbonised sucrose, was impregnated again with a solution of sucrose (0.8 g), concentrated $H_2SO_4$ (50.7 µL) and deionised water (5.0 mL) and dried in the oven using the same procedure as described above. The carbonisation was completed by pyrolysis at 800°C under the flow of helium (50 mL $min^{-1}$). The obtained powder was washed twice with NaOH (50:50 ethanol:water) at 100°C to remove the silica template, then filtered and dried at 120°C.

#### *2.2.3.2 Synthesis of HAP on CNRs*

Synthesised CNRs (0.3 g) were suspended in deionised water (6.0 mL) using an ultrasonic bath, then added to a solution of $(NH_4)_2HPO_4$ (0.4 M, 100 mL), which was stirred at room temperature (18-22°C) in a 2 L beaker. $Ca(NO_3)_2$ (0.6 M, 100 mL) was then added dropwise over one hour, resulting in a 'milky' suspension of HAP. The Ca/P molar ratio was kept at 1.67, corresponding to the stoichiometry of HAP. The pH was maintained through the addition of NaOH (0.1 M) within the range 9.4-9.5. This 'milky' suspension was then stirred overnight at room temperature using a magnetic stirring bar. The resulting precipitate was filtered, cleaned three times alternately with water and ethanol, and then dried at 65°C for six hours. To eliminate CNRs the calcination process was extended to 48 hours at 550°C with a heating rate of 1°C $min^{-1}$.

## 2.3 Results and discussion

### *2.3.1 Surfactant free*

Hydroxyapatite (HAP) was synthesised as described in the experimental section (*2.2.1*), which is a combination of previously reported studies (shown in *Table 2.1*) and optimisation of the solvents used to make the proposed procedure simpler and more efficient, with less environmental damage due to less toxic substrates employed to maintain a basic pH (*Equation 2.2*).

$$5Ca(NO_3)_2 + 3(NH_4)_2HPO_4 + NaOH \rightarrow Ca_5(PO_4)_3OH + 6NH_4NO_3 + NaNO_3 + 3HNO_3 \quad 2.2$$

The obtained material was characterised *via* SEM, which, as depicted *Figure 2.1A,* revealed a highly agglomerated crystalline HAP structure that is typical of crystal behaviour. The same observation of the morphology of HAP was reported by Yamini *et.al.*[49], where XRD studies also confirmed it belonged to a hexagonal crystal system. As observed on TEM image (shown in *Figure 2.1B*), the obtained HAP demonstrated a small degree of porosity, with the characteristic structural arrangements of calcium ions and oxygen atoms located parallel to each other.[50]

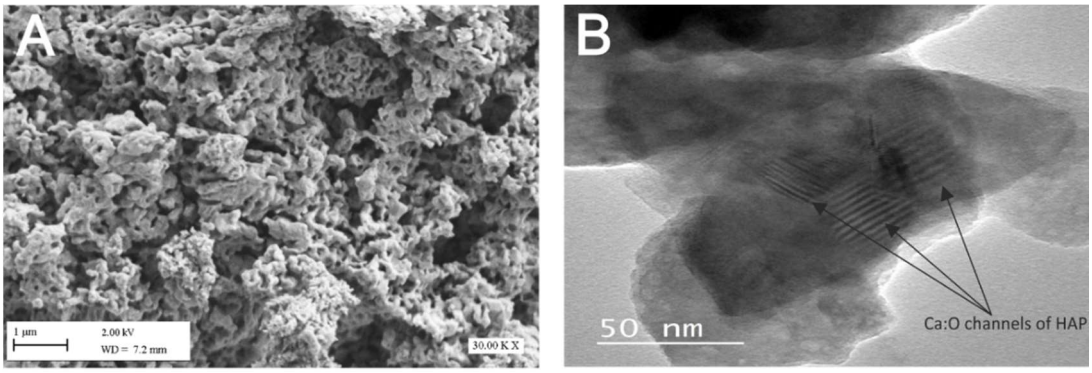


***Figure 2.1*** *SEM (A) and TEM (B) image of HAP synthesised using a template free protocol*

Following microscopic characterisation, EDX analysis was first performed to examine the elemental composition of the synthesised HAP (*Table 2.2*). Based upon these results, it is clear that the composition of the obtained powder contains the elements Ca, P, O, as expected for HAP, and they are present in the same ratio as that of the stoichiometric product. It is important to note, that the presence of sodium species are contributed by the sodium hydroxide solution used to maintain a stable pH over the course of reaction (see experimental *section 2.2.1*).

***Table 2.2*** *Elemental composition of HAP via EDX analysis*

| *Element* | *Wt%* |
|---|---|
| ***O*** | 41.34 |
| ***P*** | 18.43 |
| ***Ca*** | 34.02 |
| ***Na*** | 2.69 |

A Raman spectroscopy study was next performed to characterise the synthesised material. As shown in *Figure 2.2*, the spectrum is dominated by one sharp peak at 963 $cm^{-1}$, which represents the symmetric stretching mode ($v_3$) of the phosphate ions. The 1049 $cm^{-1}$ peak corresponds to the asymmetric stretching mode ($v_3$) of the phosphate ions, while the signal observed at 450 $cm^{-1}$ is due to the symmetric bending mode ($v_2$) of the phosphate ions. The final peak obtained at 581 $cm^{-1}$ indicates the asymmetric bending mode ($v_4$) of the phosphate groups.[18]

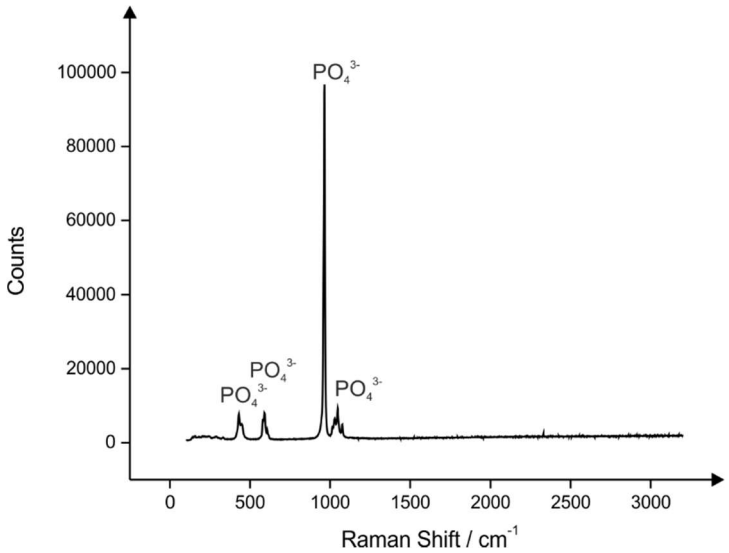


***Figure 2.2*** *Raman Spectrum of the synthesised HAP via template free method*

Subsequently, the crystallinity of HAP was investigated using XRD. The XRD pattern depicted within *Figure 2.3* showed the crystalline structure of hexagonal HAP with the $P6_3/m$ space group. This pattern revealed the successful formation of HAP without any additional phases and all major peaks observed agree with the standard JCPDS pattern of HAP (09/0432) shown in *Figure 1.11* and described in *section 1.5.1*.

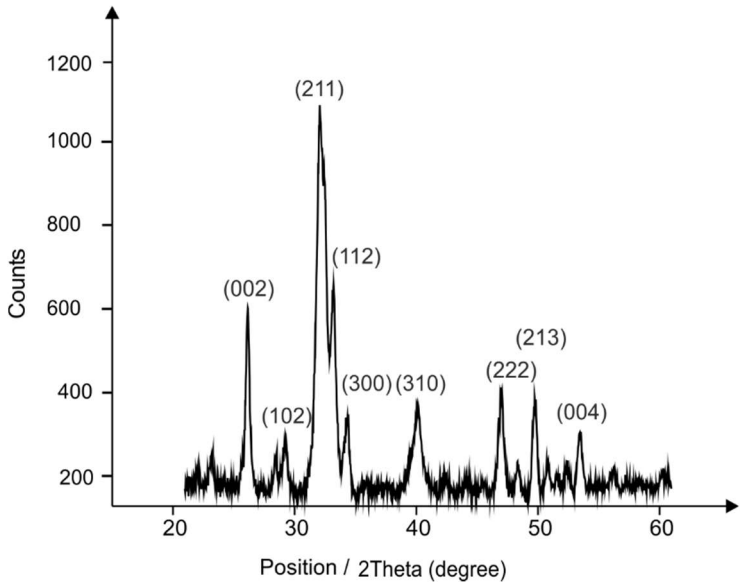


***Figure 2.3*** *XRD pattern of HAP synthesised using template free procedure*

Attention was next turned to the spectral characterisation of the HAP *via* FT-IR, using attenuated total reflectance (ATR) to indicate chemical bonding of the HAP powder and to determine any impurities, *e.g.* nitrate ions that are formed during the reaction and could cause contamination of the end product. The double peak presented at 599 $cm^{-1}$ and 603 $cm^{-1}$, as shown in *Figure 2.4*, is associated with bending modes in the P-O bonds in the phosphate groups. The peak observed at 1022 $cm^{-1}$ indicates a stretching mode in the P-O bonds within the HAP, which agrees with the reports described elsewhere.[29, 30] Therefore, the formation of the phosphate group within the synthesised HAP was also confirmed *via* FTIR studies as well as the Raman spectrum reported above. At the same time, the absence of nitro group peaks, which appear in the IR spectra in the range of 1550-1475 $cm^{-1}$ (asymmetric stretch) and 1360-1290 $cm^{-1}$ (symmetric stretch) confirmed the lack of any contamination by nitric acid, which as a by-product of the synthesised HAP was removed efficiently by multiple washing steps (using ethanol and deionised water).[49]

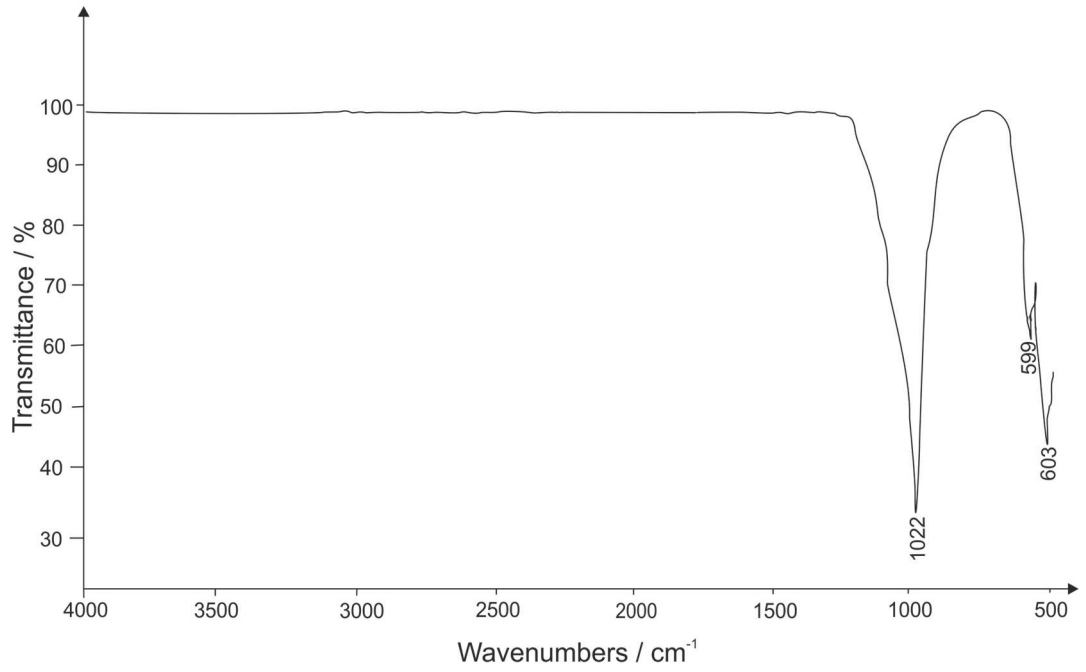


***Figure 2.4*** *FTIR characterisation of synthesised HAP using template free protocol*

Next, nitrogen adsorption isotherms were performed to measure the porosity of the synthesised HAP. The BET surface area obtained corresponded to 12.3±0.1 $m^2g^{-1}$ indicating poor porosity when compared to other supports mentioned in *Table 1.3, i.e.* not less than 100 $m^2g^{-1}$. of the material that could be a significant disadvantage in a future application as a catalyst support, where high surface area is essential to enhance the catalytic activity.

This wet synthesis approach, without any surfactant, was repeated three times with the average percentage yield found to correspond to 83.7%, which is extremely high when compared to other literature studies, as presented in *Table 2.1.* It is worth noting, however, that most of the reported studies do not mention a specific value of the yield obtained.[19, 51-55] Öner *et al.*[25] described an approach where they used less harmful components than ammonia *i.e.* potassium hydroxide, nevertheless no yield or reproducibility of the method described was specified. In comparison to previously reported strategies, summarised within *Table 2.1*, the alternative synthesis prepared in this work is more attractive, since it does not require high temperatures or pressures and, therefore, shows reduced energy consumption, homogenous mixing, nanophase particle size/shape control and higher product yield.

Obtaining high yield in the synthesis is essential to validate the proposed route and demonstrate how reliable and successful the procedure is, when compared to the theoretical equation of the reaction. However, for the application as a catalyst support for methane oxidation (which is the main objective of this project), the described methodology possesses a lack of porosity and the BET surface area is too low, therefore it is not beneficial to employ it for further catalytic applications. From this point in the thesis, HAP synthesised using this approach will be referred to as *HAP_1*.

### *2.3.2 Soft-templated approach*

To enhance the porosity and crystallinity of HAP, different silica based surfactants were employed as soft-templates, such as CTAB (cationic surfactant), Tween60 (non-ionic surfactant), $C_{12}EO_9$ (non-ionic surfactant) and a mixture of both Tween60 and $C_{12}EO_9$. All of these were previously reported as successful templates for selective control of size and shape of the synthesised particles by strongly binding to the crystal facets created. This improves the porosity and surface area of the desired product, as mentioned in *section 2.1.2*.[56]

The porosity of the resulting HAPs was studied using BET measurements. The results obtained are shown in *Table 2.3* and revealed that the porosity considerably improved from the surface area of 12.3 $m^2g^{-1}$ of sample *HAP_1,* where no surfactant was added (reported in *section 2.3.1*), to 30.9±0.2 $m^2g^{-1}$ for CTAB based HAP, 27.7±0.2 $m^2g^{-1}$ for Tween60 based HAP, 40.6±0.2 $m^2g^{-1}$ for $C_{12}EO_9$ and 84.9±0.3 $m^2g^{-1}$ when a mixture of Tween60 and $C_{12}EO_9$ was employed (samples named *HAP_2*, *HAP_3*, *HAP_4* and *HAP_5,* respectively). Regarding the surface areas obtained, it is clear that the mixture of two non-ionic surfactants was the most beneficial and significantly increased the surface area of the HAP. It can be explained by the fact that there is twice the amount of template structure present in the solution, exceeding CMC, thus providing enhanced accessibility to bind around by HAP particles.

***Table 2.3*** *BET surface area of HAP synthesised based on different soft-templates*

| Name | Surfactant used | Surface area of HAP / $m^2g^{-1}$ |
|---|---|---|
| ***HAP_2*** | CTAB | 30.9±0.2 |
| ***HAP_3*** | Tween60 | 27.7±0.2 |
| ***HAP_4*** | $C_{12}EO_9$ | 40.6±0.2 |
| ***HAP_5*** | Tween60 /$C_{12}EO_9$ (mixed) | 84.9±0.3 |

Following the porosity analysis, SEM images revealed more crystalline HAP formed using a soft-template approach, when compared to *HAP_1* (template free), however it remained highly agglomerated. As an example, a SEM image of *HAP_3* is shown in *Figure 2.5*.

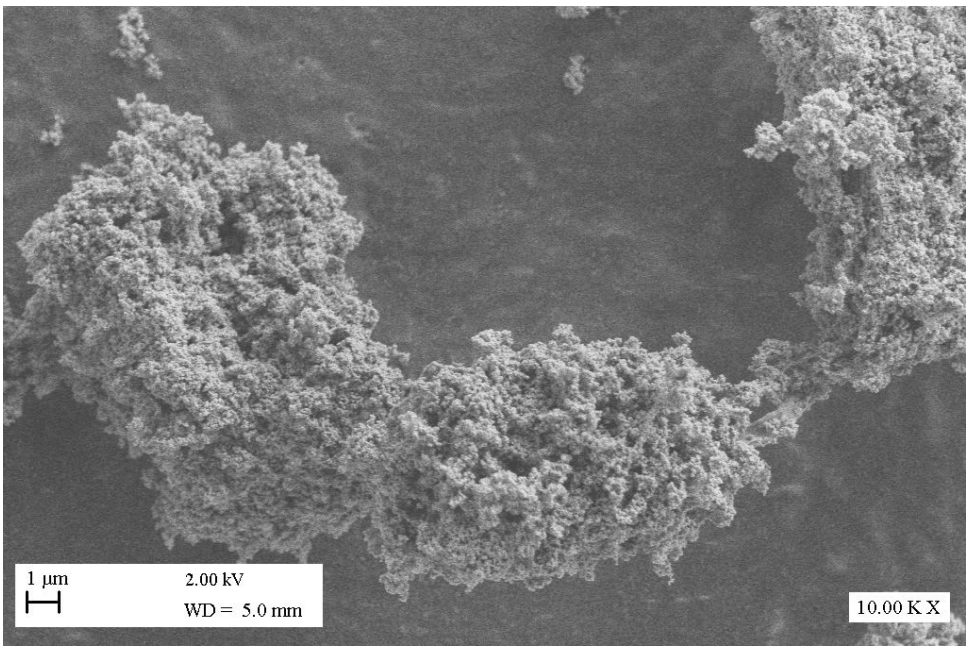


***Figure 2.5*** *SEM image of HAP_3*

Next, to investigate further changes in the crystallinity after adding the template to the system, XRD was performed. As shown in the *Figure 2.6* all samples exhibited the characteristic peaks corresponding to the $P6_3/m$ hexagonal atomic arrangement of HAP and they were in agreement with the HAP standard pattern, mentioned in *section 1.5.1*.

Moreover, the presence of sharper peaks, when compared to *HAP_1,* demonstrated the expected improvement in the crystallinity of the HAP using the soft-templating approach. Nevertheless, no major differences were observed in XRD patterns between HAPs synthesised on different silicate templates.

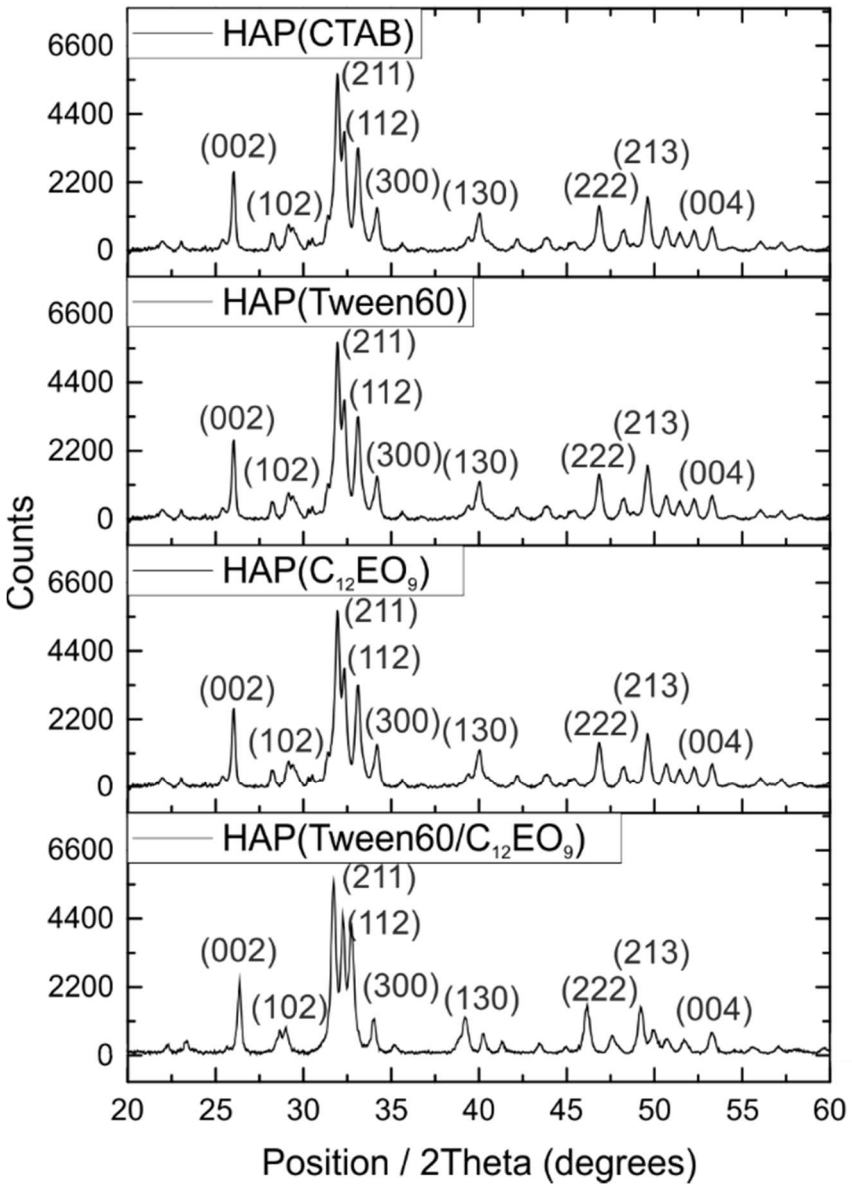


***Figure 2.6*** *XRD patterns of the synthesised HAP on different surfactants*

Finally, taking into account both the crystallinity and the porosity of the HAPs, the soft-templating methodology is an easily adaptable alternative to the standard wet chemical approach, making it a powerful tool to enhance the properties of the synthesised materials that can be significantly beneficial for future catalytic applications.

Moreover, the obtained results prove that the HAP synthesised using soft-templates is resistant to the template removal, maintaining the properties gained through this approach, which is additional advantage.

### *2.3.3 Hard-template approach*

The other and very powerful alternative to the soft-templating approach is to utilise hard-templates *i.e.* ion-exchange resins or a carbon framework. Such procedures have been extensively employed to synthesise porous spherical materials, like zeolites of macroporous silicates. For example, Tosheva *et.al.* described anion exchange resins as shape-directing macro-templates for zeolite silicate-1 synthesis, obtaining a surface area of 930 $m^2g^{-1}$ for the most porous reported sample.[57] However, zeolite-like materials are more flexible than HAP, hence they are more able to bend around the hard-template without breaking their structure. In this study, for the first time in the literature a wet chemical methodology based on the utilisation of carbon nanorods as a hard-template approach to synthesise mesoporous HAP was reported. The sketch of the procedure performed for the synthesis of HAP is presented in *Figure 2.7*.

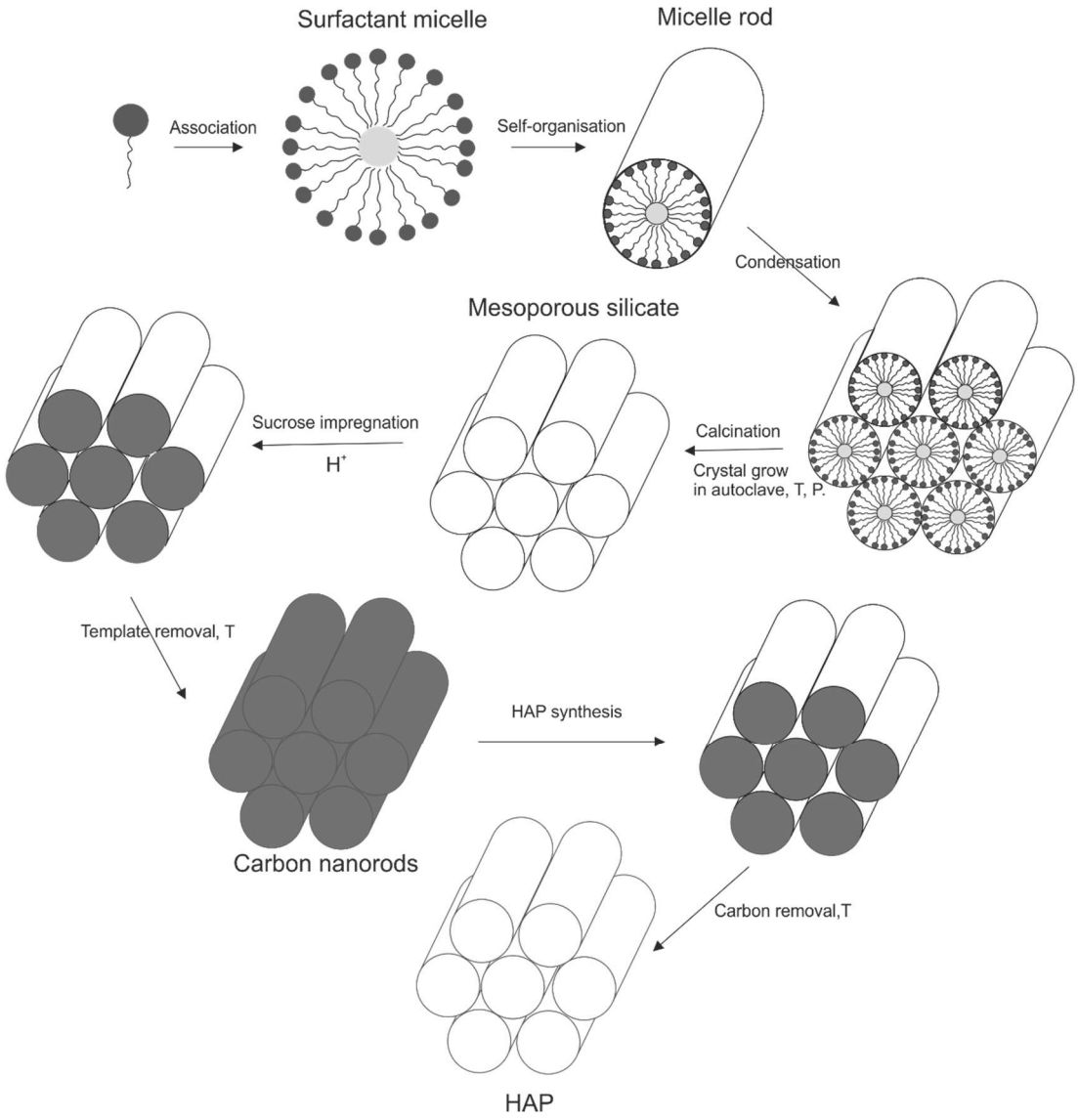


***Figure 2.7*** *Overview of the bespoke synthetic process of HAP using CNRs*

As described in *section 2.2.3.1*, the synthesis of a set of CNRs was performed simultaneously using three different mesoporous silicates; SBA-15, MCM-41 and MCM-48. Phase purity of all 3 synthesised silica was confirmed *via* XRD. Each silicate was impregnated with acidified sucrose solution and after a series of thermal treatments, a carbonisation process occurred to obtain CNRs. Then, the carbon nano-rods obtained were dispersed and utilised in the precipitation of HAP, employing a wet chemical synthetic route described in detail in *section 2.2.3.2*. After each step of the proposed procedure, subsequent products were characterised for crystallinity and porosity using several techniques.

First, hexagonal and highly ordered SBA-15 was utilised as a template for CNR synthesis. Surface characteristics were investigated and the corresponding surface area obtained using BET measurements. Consequently, the expected very high surface area of SBA-15 was found to be 667.3±4.9 $m^2g^{-1}$ with an average pore diameter of 5.1 nm, using Barrett-Joyner-Halenda (BJH) analysis, as shown in *Figure 2.8*. The surface area of the subsequently synthesised CNRs was found to correspond to 315.6±4.6 $m^2g^{-1}$ with a very similar pore diameter to that of the SBA-15. The results, therefore, suggest that the procedure employed to synthesise CNRs was highly effective. What makes this novel approach even more interesting is that the surface area of the synthesised HAP using CNRs was 242.2±2.3 $m^2g^{-1}$, which is extremely high when compared to that reported in the literature. Moreover, BJH pore size distributions of HAP revealed a mixture of pore sizes; pores with a diameter of 3.5 nm were formed due to direct templating with the CNRs, while a broad distribution of pores with an average diameter of 18.9 nm were observed due to the capillary condensation between HAP particles, as presented in *Figure 2.8*. The high porosity obtained herein considerably exceeds that described by Cheikhi *et al*., where surface areas over four times lower have been previously reported.[58]

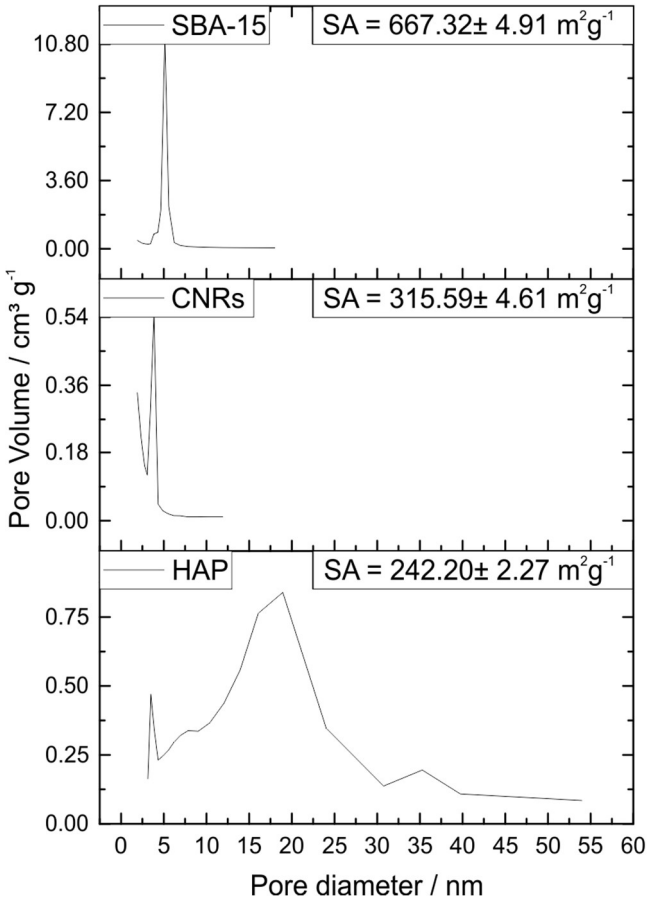


***Figure 2.8*** *BJH pore diameter distribution with corresponding BET surface area (SA) of 3-stage synthesis of HAP on CNRs obtained using SBA-15*

TEM was subsequently employed to investigate surface characteristics of the resulting products. As shown in *Figure 2.9A*, SBA-15 revealed a highly ordered hexagonal array of silica, which is in agreement with the very high surface area obtained. CNRs were then successfully formed and exhibited rod-like particles, observed in *Figure 2.9B*. Finally, hexagonal repeated structural arrangements of Ca and O atoms characteristic of HAP are shown in *Figure 2.9C.* Thus it is clear that HAP was successfully formed using this exciting approach.

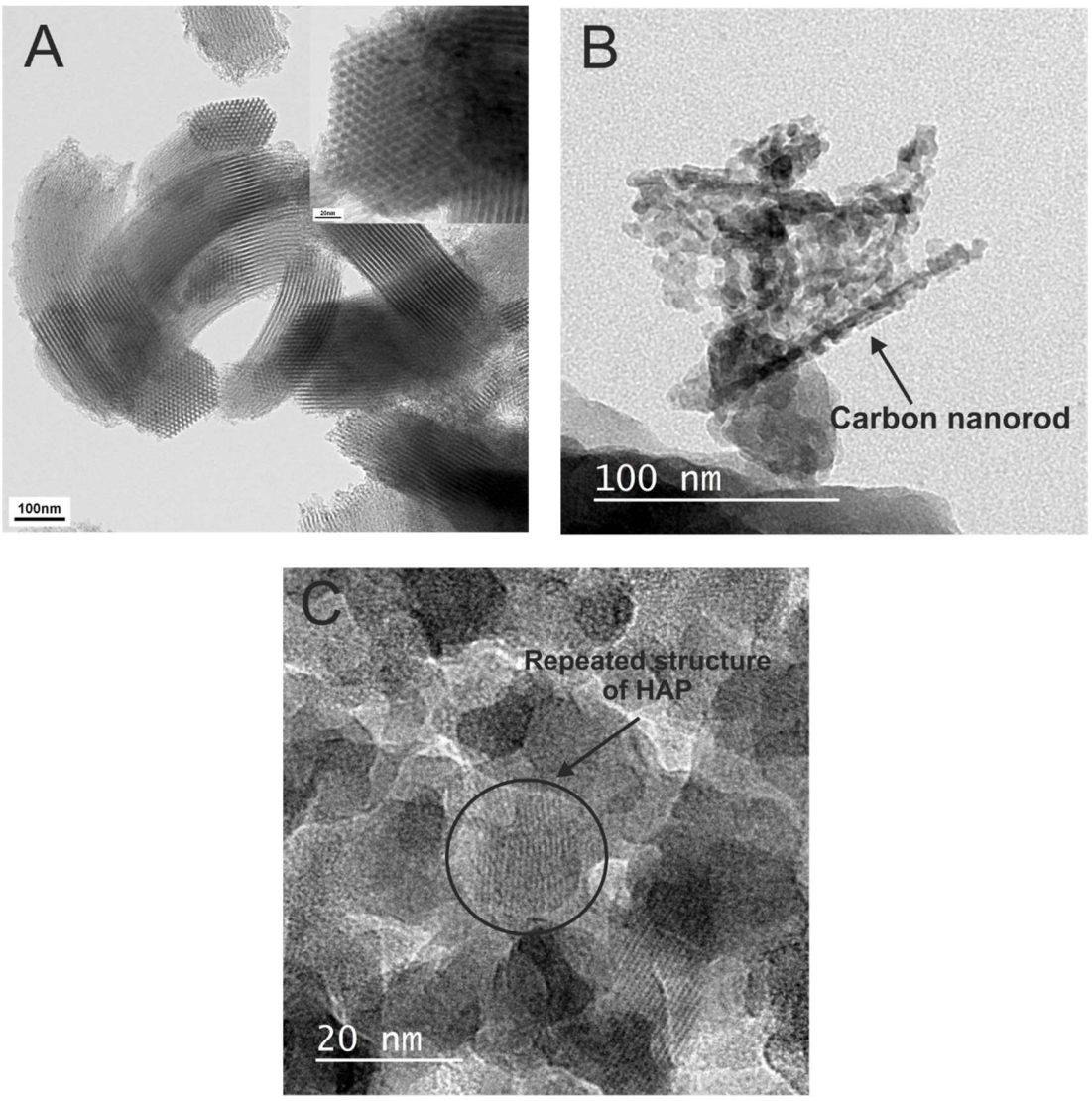


***Figure 2.9*** *TEM images of SBA-15 (A) followed by synthesised CNRs (B) and resulting HAP (C) via this approach*

Next, attention was turned to the CNRs and the HAP obtained using a different hexagonal mesoporous material; MCM-41. For synthesised MCM-41, the surface area corresponded to 1086.7±14.3 $m^2g^{-1}$ with an average pore diameter of 3.0 nm, as shown in *Figure 2.10*. However, the resulting CNRs based on MCM-41 silicate were drastically decreased in porosity, with a surface area of only 108.9±3.2 $m^2g^{-1}$ with a very high average pore diameter that was found to be out of the range of the instrument (>100 nm) and hence could not be accurately determined. It is interesting to note, that as reported by Hussain *et al.*[59] MCM-41 is hydrothermally unstable, thus high temperature during the carbonisation process caused sintering of the pores, and

therefore lead to a significant decrease in the porosity. Also, the resulting HAP revealed a surface area of 44.4±0.3 $m^2g^{-1}$ and two types of pores were observed. The first type of pores formed were around 3.0 nm in diameter, while the other type revealed wide range of sizes with an average diameter of 45.0 nm.

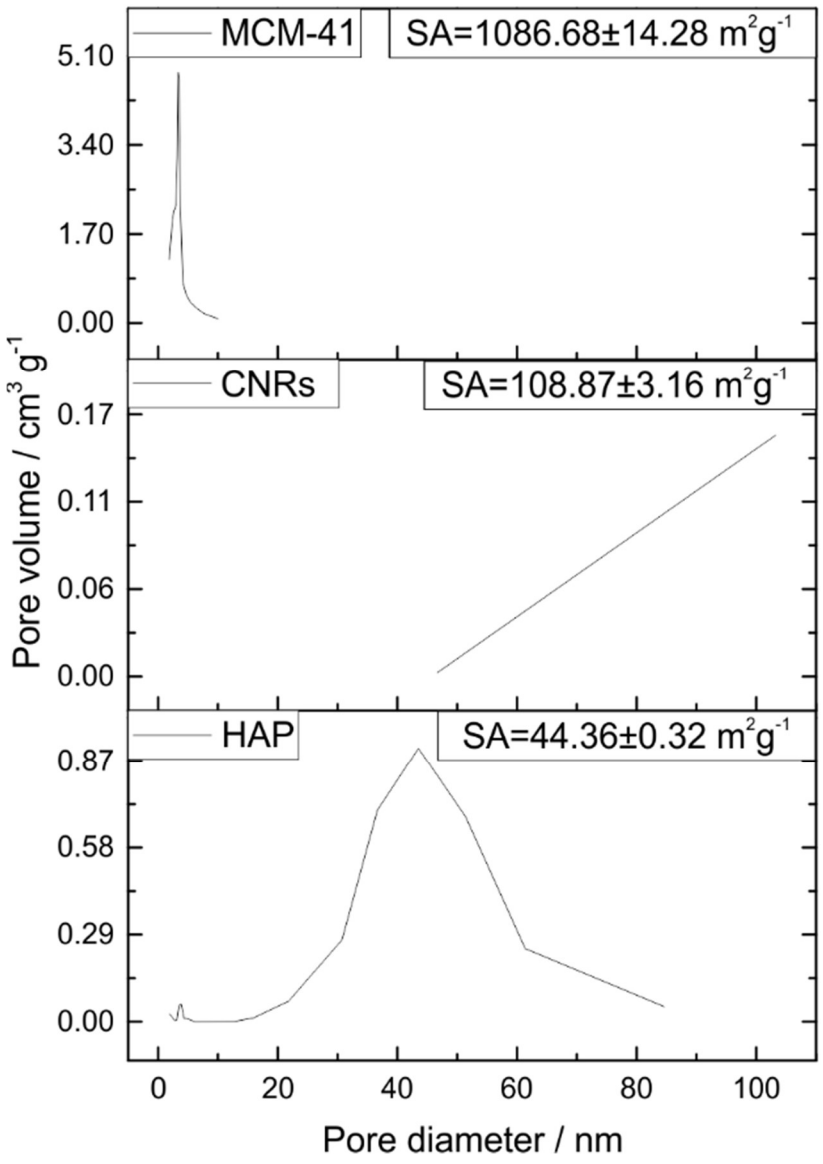


***Figure 2.10*** *BJH pore diameter distribution with corresponding BET surface area (SA) of 3-stage synthesis of HAP on CNRs using MCM-41*

Nitrogen adsorption isotherms were also employed to establish the surface characteristics of the last silicate employed in this study *i.e.* MCM-48. As shown in *Figure 2.11*, the BET surface area of the silica template, MCM-48, was found to be 987.9±44.3 $m^2g^{-1}$ with an average pore diameter < 5.0 nm.

Moreover, the resulting CNRs revealed a surface area of 258.22±5.35 $m^2g^{-1}$ and an average pore diameter of 5.0 nm, which is similar to those of MCM-48. However, much larger pores were observed in subsequent HAP, with an average pore diameter of 30.0 nm, along with small pores of an average size of < 5.0 nm. Furthermore, a high surface area was observed in the mesoporous HAP synthesised on CNRs using MCM-48, which corresponded to 97.57±1.16 $m^2g^{-1}$.

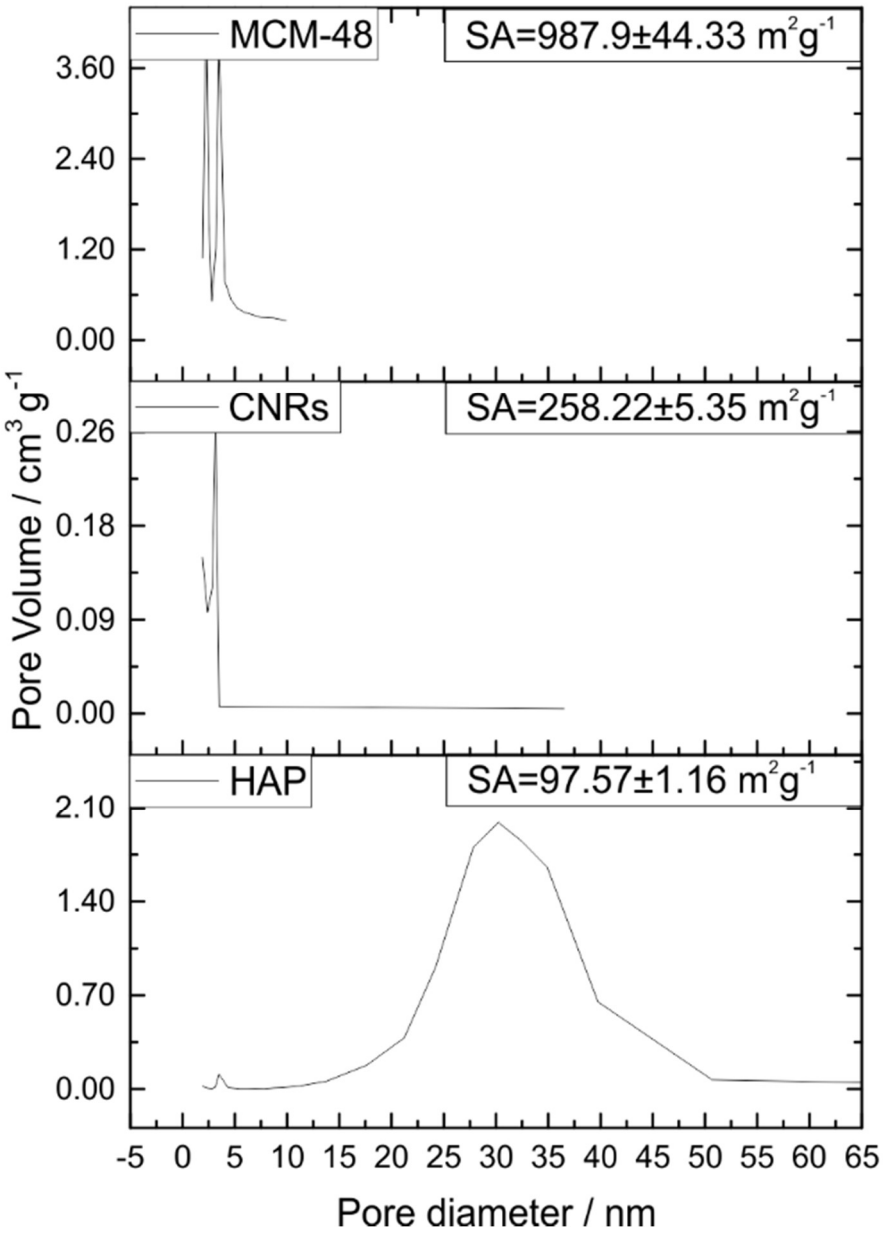


***Figure 2.11*** *BJH pore diameter distribution with corresponding BET surface area (SA) of 3-stage synthesis of HAP on CNRs using MCM-48*

Thus, a similar trend of the pores obtained was observed in all three procedures when different silicates were utilised for the synthesis of CNRs and then HAP, revealing mixture of two types of pores formed in the structure of the HAP.

XRD was employed to confirm the crystallinity of the synthesised HAPs. The XRD patterns presented in *Figure 2.12* revealed all the major peaks that correspond to the hexagonal HAP, when compared to the standard diffraction pattern. In addition, due to the hard-templating protocol exploited all, synthesised HAPs showed highly crystalline structures. However, there was no significant alterations observed in the crystal structure between the samples, suggesting that the different silicate employed for the synthesis of HAP does not influence the crystallinity of the resulting product.

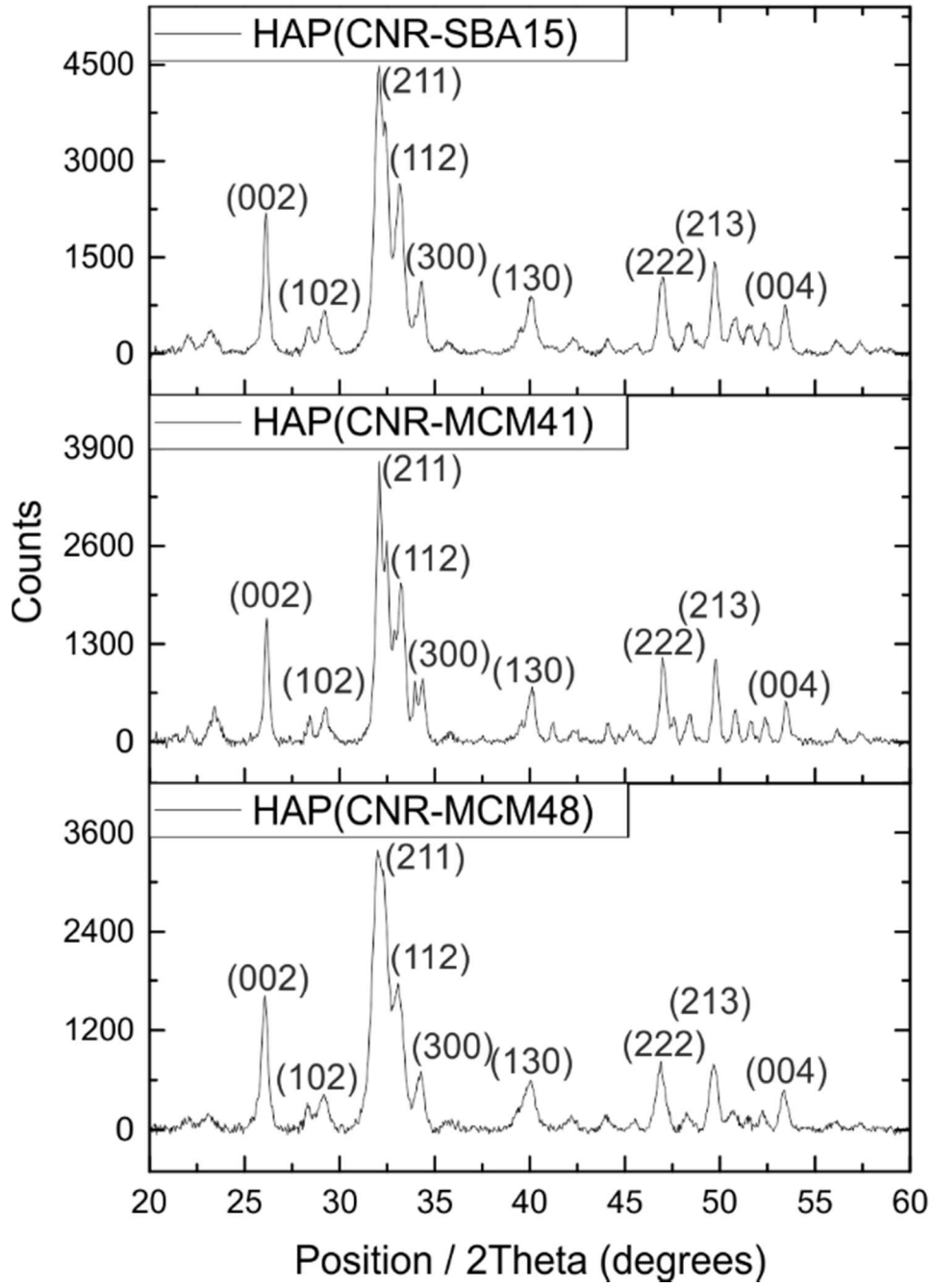


***Figure 2.12*** *XRD patterns of HAP based on CNRs synthesised on different silicates*

Finally, the obtained results revealed that the most porous sample with the highest surface area was obtained when SBA-15 was utilised for CNR synthesis. TEM images confirmed the formation of HAP and XRD patterns matched closely with the standard JCPDS of HAP.

Moreover, two different types of pores were obtained when using this hard-templating procedure, with one type of pores formed due to direct CNR templating and the other type due to the capillary condensation between HAP particles.

The hard-templating approach to synthesising single-phase mesoporous HAP, developed and reported for the first time in this section, can become a very powerful alternative methodology for the synthesis of mesoporous materials.

## 2.4 Conclusions

This chapter has reported the successful synthesis of HAP using novel, simple wet chemical approaches with less energy consumed and less toxic substrates used when compared to the literature. However, the obtained *HAP_1* lacked the porosity and high surface area necessary for catalytic applications.

Besides being easily adaptable, the soft-templating approach was also employed to enhance the porosity of the resulting HAP with the assistance of three different surfactants. The proposed soft-template synthetic route revealed a significant improvement in BET surface area from 12.3±0.1 $m^2g^{-1}$ obtained for *HAP_1* (template free) to 84.85±0.31 $m^2g^{-1}$ for *HAP_5,* which is an important feature for future catalytic applications. The attained results showed that the mixture of two non-ionic surfactants was the most beneficial and significantly increased the surface area of the HAP, due to twice the amount of the surfactant being present in the solution, providing enhanced accessibility for HAP particles to bind around it. Furthermore, the crystallinity of the resulting HAPs synthesised using soft-templates improved and was confirmed by XRD patterns.

On the other hand, a novel hard-templating approach using carbon nanorods synthesised on three different silica (SBA-15, MCM-41 and MCM-48) was reported to produce mesoporous crystal hydroxyapatite (HAP) with enhanced porosity. The crystallinity of the structure was again confirmed by XRD with no changes observed when different silicates were employed to synthesise CNRs.

Moreover, BET analysis revealed that the hexagonal SBA-15 provided the best shape-directing template for CNR synthesis and hence resulted in the successful formation of mesoporous HAP with a high surface area of 242.20± 2.27 $m^2g^{-1}$. Furthermore, two types of pores were obtained using hard-template approach; one due to direct CNRs templating and the other type due to capillary condensation between HAP particles. Also, the results obtained demonstrated that HAP is resistant to the template removal in both soft- and hard- template approaches, which is additional advantage of this procedure.

Finally, obtained results presented in this chapter demonstrated the successful synthesis of single-phase mesoporous HAP *via* soft- and hard-template approaches that can be easily adapted to well-known wet chemical routes, making it a promising protocol, and more importantly providing the exciting material that can be utilised further as a catalytic support.

## 2.5 References


1. A. Andrasekhar, S. Sagadevan and A. Dakshnamoorthy, *International Journal of Physical Sciences*, 2013, **8**, 1639-1645.
2. P. Kamalanathan, S. Ramesh, L. T. Bang, A. Niakan, C. Y. Tan, J. Purbolaksono, H. Chandran and W. D. Teng, *Ceramics International*, 2014, **40**, 16349-16359.
3. P. Wang, C. Li, H. Gong, X. Jiang, H. Wang and K. Li, *Powder Technology*, 2010, **203**, 315-321.
4. Y. Feng, H. Yin, D. Gao, A. Wang, L. Shen and M. Meng, *Journal of Catalysis*, 2014, **316**, 67-77.
5. M. E. Bahrololoom, M. Javidi, S. Javadpour and J. Ma, *Journal of Ceramic Processing Research*, 2009, **10**, 129-138.
6. J. Liu, K. Li, H. Wang, M. Zhu and H. Yan, *Chemical Physics Letters*, 2004, **396**, 429-432.
7. S.-C. Wu, H.-K. Tsou, H.-C. Hsu, S.-K. Hsu, S.-P. Liou and W.-F. Ho, *Ceramics International*, 2013, **39**, 8183-8188.
8. Y. Wang, X. Ren, X. Ma, W. Su, Y. Zhang, X. Sun and X. Li, *Crystal Growth & Design*, 2015, **15**, 1949-1956.
9. X. Ji, P. Su, C. Liu, J. Song, C. Liu, J. Li, H. Tan, F. Wu, L. Yang, R. Fu, C. Tang and B. Cheng, *Journal of the American Ceramic Society*, 2015, **98**, 1702-1705.
10. J. S. Cho and S.-H. Rhee, *Journal of the European Ceramic Society*, 2013, **33**, 233-241.
11. C.-W. Chen, R. E. Riman, K. S. TenHuisen and K. Brown, *Journal of Crystal Growth*, 2004, **270**, 615-623.
12. Y. Fang, D. K. Agrawal and D. M. Roy, *THERMAL-STABILITY OF SYNTHETIC HYDROXYAPATITE*, 1994.

13. E. San Thian, Z. Ahmad, J. Huang, M. J. Edirisinghe, S. N. Jayasinghe, D. C. Ireland, R. A. Brooks, N. Rushton, W. Bonfield and S. M. Best, *Biomaterials*, 2008, **29**, 1833-1843.
14. Y. Wu, L. L. Hench, J. Du, K.-L. Choy and J. Guo, *Journal of the American Ceramic Society*, 2004, **87**, 1988-1991.
15. I. Nikčević, V. Jokanović, M. Mitrić, Z. Nedić, D. Makovec and D. Uskoković, *Journal of Solid State Chemistry*, 2004, **177**, 2565-2574.
16. S. Xu, J. Long, L. Sim, C. H. Diong and K. Ostrikov, *Plasma Processes and Polymers*, 2005, **2**, 373-390.
17. K. Teshima, S. Lee, M. Sakurai, Y. Kameno, K. Yubuta, T. Suzuki, T. Shishido, M. Endo and S. Oishi, *Crystal Growth & Design*, 2009, **9**, 2937-2940.
18. S. Ramesh, C. Y. Tan, R. Tolouei, M. Amiriyan, J. Purbolaksono, I. Sopyan and W. D. Teng, *Materials & Design*, 2012, **34**, 148-154.
19. Y. Sargin, M. Kizilyalli, C. Telli and H. Güler, *Journal of the European Ceramic Society*, 1997, **17**, 963-970.
20. P. N. Kumta, C. Sfeir, D.-H. Lee, D. Olton and D. Choi, *Acta Biomaterialia*, 2005, **1**, 65-83.
21. W. Michał, D. Ewa and C. Tomasz, *Colloid and Polymer Science*, 2015, **293**, 1561-1568.
22. M. Kavitha, R. Subramanian, R. Narayanan and V. Udhayabanu, *Powder Technology*, 2014, **253**, 129-137.
23. V. Dhand, K. Y. Rhee and S. J. Park, *Materials Science and Engineering: C*, 2014, **36**, 152-159.
24. L. Yang, X. Ning, Y. Bai and W. Jia, *Materials Letters*, 2013, **113**, 142-145.
25. M. Öner and U. Uysal, *Materials Science and Engineering: C*, 2013, **33**, 482-489.
26. C. Kothapalli, M. Wei, A. Vasiliev and M. T. Shaw, *Acta Materialia*, 2004, **52**, 5655-5663.
27. S. K. Padmanabhan, A. Balakrishnan, M. C. Chu, Y. J. Lee, T. N. Kim and S. J. Cho, *Particuology*, 2009, **7**, 466-470.
28. E. Landi, G. Celotti, G. Logroscino and A. Tampieri, *Journal of the European Ceramic Society*, 2003, **23**, 2931-2937.
29. M. Okada and T. Furuzono, *Journal of Colloid and Interface Science*, 2011, **360**, 457-462.
30. J. Abert, C. Bergmann and H. Fischer, *Ceramics International*, 2014, **40**, 9195-9203.
31. S. Kongsri, K. Janpradit, K. Buapa, S. Techawongstien and S. Chanthai, *Chemical Engineering Journal*, 2013, **215–216**, 522-532.
32. Y. Yan, X. Dong, X. Sun, X. Sun, J. Li, J. Shen, W. Han, X. Liu and L. Wang, *Journal of Colloid and Interface Science*, 2014, **429**, 68-76.
33. E. J. M. Edralin, J. L. Garcia, F. M. dela Rosa and E. R. Punzalan, *Materials Letters*, 2017, **196**, 33-36.
34. S. Rujitanapanich, P. Kumpapan and P. Wanjanoi, *Energy Procedia*, 2014, **56**, 112-117.
35. S.-C. Wu, H.-C. Hsu, S.-K. Hsu, C.-P. Tseng and W.-F. Ho, *Advanced Powder Technology*, 2017, **28**, 1154-1158.
36. Y. Zhang, Y. Liu, X. Ji, C. E. Banks and W. Zhang, *Materials Letters*, 2012, **78**, 120-123.
37. Y. Xie, D. Kocaefe, C. Chen and Y. Kocaefe, *Journal of Nanomaterials*, 2016, **2016**, 10.
38. N. Pal and A. Bhaumik, *Advances in colloid and interface science*, 2013, **189–190**, 21-41.
39. H. Yang and Y. Wang, *Materials Science and Engineering: C*, 2016, **62**, 160-165.
40. M. Uota, H. Arakawa, N. Kitamura, T. Yoshimura, J. Tanaka and T. Kijima, *Langmuir*, 2005, **21**, 4724-4728.

41. K. K. Perkin, J. L. Turner, K. L. Wooley and S. Mann, *Nano Letters*, 2005, **5**, 1457-1461.
42. V. Uskoković and D. P. Uskoković, *Journal of Biomedical Materials Research Part B: Applied Biomaterials*, 2011, **96B**, 152-191.
43. L. B. Gower, *Chemical Reviews*, 2008, **108**, 4551-4627.
44. A. L. Boskey and A. S. Posner, *The Journal of Physical Chemistry*, 1973, **77**, 2313-2317.
45. J. Eastoe, M. J. Hollamby and L. Hudson, *Advances in colloid and interface science*, 2006, **128-130**, 5-15.
46. S. Sugiyama, T. Minami, T. Moriga, H. Hayashi, K. Koto, M. Tanaka and J. B. Moffat, *Journal of Materials Chemistry*, 1996, **6**, 459-464.
47. S. Sugiyama, T. Minami, H. Hayashi, M. Tanaka and J. B. Moffat, *Journal of Solid State Chemistry*, 1996, **126**, 242-252.
48. D. W. Oxtoby, *Journal of Physics: Condensed Matter*, 1992, **4**, 7627.
49. D. Yamini, G. Devanand Venkatasubbu, J. Kumar and V. Ramakrishnan, *Spectrochimica Acta Part A: Molecular and Biomolecular Spectroscopy*, 2014, **117**, 299-303.
50. Z. Opre, D. Ferri, F. Krumeich, T. Mallat and A. Baiker, *Journal of Catalysis*, 2006, **241**, 287-295.
51. A. P. Craig, A. S. Franca and J. Irudayaraj, in *High Throughput Screening for Food Safety Assessment*, eds. A. K. Bhunia, M. S. Kim and C. R. Taitt, Woodhead Publishing, 2015, DOI: http://dx.doi.org/10.1016/B978-0-85709-801-6.00007-1, pp. 165-194.
52. F. Mohandes, M. Salavati-Niasari, M. Fathi and Z. Fereshteh, *Materials Science and Engineering: C*, 2014, **45**, 29-36.
53. S. R. Ramanan and R. Venkatesh, *Materials Letters*, 2004, **58**, 3320-3323.
54. A. Javadi, A. Shockravi, M. Koohgard, A. Malek, F. A. Shourkaei and S. Ando, *European Polymer Journal*, 2015, **66**, 328-341.
55. K. T. Arul, J. R. Ramya, G. M. Bhalerao and S. N. Kalkura, *Ceramics International*, 2014, **40**, 13771-13779.
56. Y. Wan and Zhao, *Chemical Reviews*, 2007, **107**, 2821-2860.
57. L. Tosheva, V. Valtchev and J. Sterte, *Microporous and Mesoporous Materials*, 2000, **35–36**, 621-629.
58. N. Cheikhi, M. Kacimi, M. Rouimi, M. Ziyad, L. F. Liotta, G. Pantaleo and G. Deganello, *Journal of Catalysis*, 2005, **232**, 257-267.
59. M. Hussain, S.-K. Song and S.-K. Ihm, *Fuel*, 2013, **106**, 787-792.

# Chapter 3: Chemical, Thermal and Mechanical Stability of Mesoporous HAP

# 3.1 Introduction

In this chapter, synthesised mesoporous HAP (*HAP_5*, described in detail in Chapter 2) was explored for its stability under various treatments, simulating what happens to the catalyst in the exhaust of a HGV during running on roads. First, chemical stability was studied through treating previously prepared HAP in a wide range of pH (2 to 12) using a Britton-Robinson buffer solution, devoting special attention to acidic media, which is found in exhausts due to fume gases. Then, since engine operation temperatures are rather high, thermal stability was investigated by exposing HAP to different temperatures and studying changes in characteristics within the structure of HAP *via* SEM, XRD and BET. Moreover, HAP was subjected to mechanical disturbances by using ultrasound in order to explore its structural stability, exceeding the nature of the turbulences that a catalyst experiences in an exhaust system over numerous hours on the roads. Results within this chapter have been submitted for publication in Journal of Inorganic and Organometallic Polymers and Materials and are under review.

## *3.1.1 Stability of Hydroxyapatite*

The chemical, thermal and mechanical stability of HAP is of significant importance and a lack of stability through undesirable influences on the material can be detrimental in its applications.

The most described studies in the literature are those on the thermal stability of HAP, *i.e.*, studies of the influence of temperature on the structure. The decomposition of HAP, which most likely occurs at high temperatures, includes dehydroxylation followed by further decomposition.[1] Dehydroxylation leads to a loss of OH groups, in consequence producing oxyhydroxyapatite ($Ca_{10}(PO_4)_6O_x(OH)_{2-2x}$, OHAP) as a transition product, followed by oxyapatite ($Ca_{10}(PO_4)_6O$, OAP).[2, 3] Although the presence of OHAP has been the subject of controversy throughout the years, its existence is now accepted even though the behaviour of OHAP is still not fully understood.

In view of that, there are numerous contradictory results in the literature, mainly due to the lack of methods to quantitatively determine the residual water content in dehydrated samples.[2] Many researchers have investigated the thermal stability of apatites, however their results for the initial temperatures that cause dehydroxylation and decomposition are divergent, depending on the purity, crystallinity and the stoichiometry of HAP, as well as the conditions employed in those investigations.[4] In general, dehydroxylation of HAP proceeds through conversion stages that correspond to different kinetic mechanisms. According to the calculated activation-energy-conversion degree plot, such processes relate to four successive routes with different activation energies, such as $OH^-$ diffusion through HAP; $OH^-$ debonding from the HAP lattice; lattice constitution of OAP and loss of surface water by the reaction interface represented in *Equation 3.1*.[4]

$$2OH^- \rightarrow H_2O \uparrow + O^{2-} \qquad 3.1$$

Therefore, the decomposition of HAP has been described as a process of continuous reactions, in which the degree of dehydroxylation can strongly influence the critical temperature of further decomposition reactions that will take place. That is, for instance, in the presence of water vapour dehydroxylation is inhibited, hence the critical temperature of the decomposition increases when compared to the temperature at which dehydroxylation takes place without any hindering factors.[3]

Following dehydroxylation, decomposition of HAP directly correlates with thermal treatments and results in the production of various calcium phosphates, such as β-tricalcium phosphate (β-TCP), calcium oxide or tetracalcium phosphate (TTCP). It is interesting to note, that both dehydroxylation and decomposition of HAP are described as reversible under controlled cooling and heating processes. For this reason, performing kinetic studies on the behaviour of HAP during thermal treatments remains challenging.[5]

During transformations of HAP under thermal treatments, there have been numerous possible physical changes described in the literature that can take place, mainly through a process called sintering. This consists of conversion of the powder into a dense solid after heat treatments. [6]

It is generally known that the driving force of sintering is the elimination of internal surface area associated with the porosity of a material, in order to reduce the surface free energy. Although the decrease of such energy is relatively small when compared to chemical processes, sintering is effective and occurs at reasonable rates.

Three stages of sintering are recognised: the initial stage begins as soon as there is some degree of mobility of the atoms within the material, caused by the temperature and, as a consequence, sharply concave necks are produced between the two particles. This stage leads to small linear shrinking of 5%. Then, in the intermediate stage, the high curvatures created in the initial stage are moderated forming interpenetrating networks of solid particles, yielding a ˜5-10% of change in porosity. At this stage, the increased size of the grains and pores starts to become significant. As sintering progresses, in the final stage the pores break down into isolated and closed voids, which is associated with extensive grain growth.[7]

There are several mechanisms of sintering described, which are divided into two groups; non-densifying (though vapour transport, surface diffusion or lattice (volume) diffusion), where microstructural changes can be observed with no shrinking, shown as mechanisms 1-3 in *Figure 3.1*; and densifying (grain boundary diffusion and dislocation motion), where material is removed from the grain boundary region and leads to shrinking (mechanisms 4 and 5 in *Figure 3.1*).

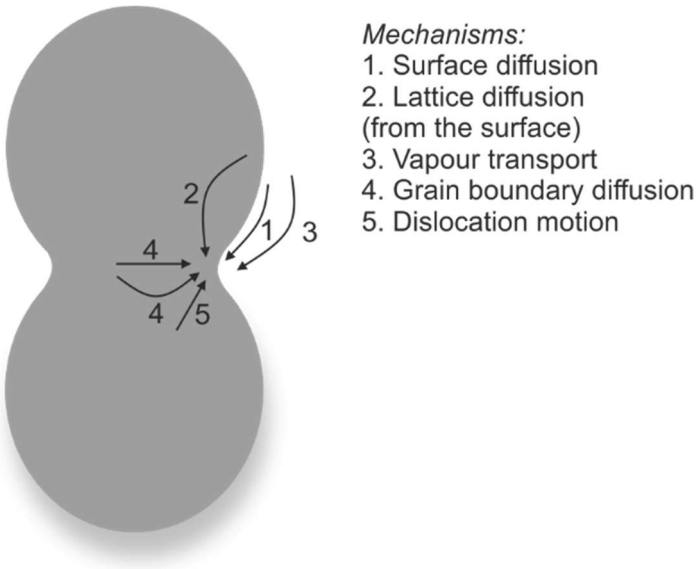


***Figure 3.1*** *Schematic representation of the sintering mechanisms between two particles*

One of the important sintering processes involves coarsening, referred to as Ostwald ripening, and it is an observed phenomenon of phase transformation of particles at different sizes, where the system aims to lower its overall energy through diffusion of small particles (which are energetically unfavourable) and attaching them to the surface of larger particles (*Figure 3.2*).[8] In general, since mesoporous materials exhibit high surface area, thermodynamic equilibrium is not obtained. Thus, *via* Ostwald ripening, the number of small particles constantly decreases at higher temperatures, while at the same time larger particles are formed in order to become more thermodynamically stable.[9] In fact, various sintering mechanisms can occur independently, thus there is a competition between coarsening and densification of the material.[7]

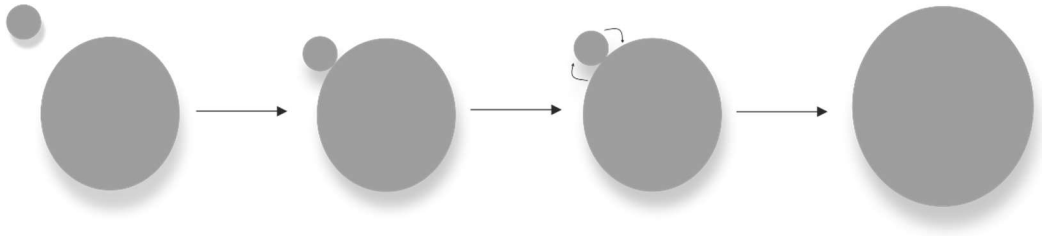

***Figure 3.2*** *Schematic representation of simplified Ostwald ripening*

Apart from thermal stability, chemical stability of HAP is significant from both a scientific and application point of view. It has been described that, inside the exhaust there is a slightly acidic environment due to the presence of $CO_2$, $NO_2$ and $SO_2$ gases. This is caused by unburnt diesel species and also NG residues, which after being released into the atmosphere, lead to the formation of acid rains. However, from the catalytic point of view, a catalyst placed in the exhaust is constantly exposed to an acidic environment, which can negatively influence not only its structure, but also its catalytic performance. In consequence, the catalytic support employed for any exhaust treatments must be resistant to any changes of pH, especially when pH is below 7.[10] Nevertheless, there are no published reports that investigate the influence of different pH on the structure of HAP and its performance in different applications.

It is also interesting to note that all HGVs transport cargo via different surfaces and different conditions of roads, thus they constantly experience many mechanical disturbances. In view of that, over the course of many hours on roads, a catalyst placed in the exhaust is involved in various vibrations, shaking, *etc*. with different intensity levels. The exposure of the catalysts to such mechanical disturbances remain unexplored due to the difficulty of accurately reproducing the road conditions. However, it is clear that the catalyst is required to be resistant to any physical degradation under mechanical stress. In view of that, by exposing HAP to ultrasound, which is known as a drastic technique to break down materials, its mechanical stability can be explored.

## 3.2 Experimental

### *3.2.1 Chemical stability*

To study the chemical stability of HAP, *HAP_5* (0.3 g) was added to Britton-Robinson buffer solutions (20 mL) covering the full range of pH. Different pH (2, 4, 6, 8, 10, 12) buffers were prepared using adequate amounts of NaOH (0.2 M). The mixtures were stirred for 3 hours at room temperature, the solid was recovered by filtration and dried at 60°C in the oven for further analysis using SEM, XRD, FTIR and BET techniques.

### *3.2.2 Thermal stability*

To investigate thermal stability, a set of *HAP_5* samples (0.3 g) were placed in crucibles and heated in a furnace (OMEGALUX LMF-3550) to a range of temperatures between 550-900°C for 3 hours with a heating rate of 10°C $min^{-1}$. Each sample was then cooled to room temperature and further analysed *via* SEM, XRD, FTIR and BET.

### *3.2.3 Mechanical stability*

To examine HAP for its mechanical stability, *HAP_5* (0.1 g) was mixed with deionised water (1 mL) in a volumetric flask. Mixtures were placed in an ultrasonic bath (Ultrawave Limited, Cardiff, UK) for different periods of time, from 10 min to 1 hour. All samples were recovered by filtration and dried at 60°C in the oven prior to further analysis employing SEM, XRD and BET.

# 3.3 Results and Discussion

## *3.3.1 Influence of pH on stability of HAP*

The influence of pH media on HAP was investigated using Britton-Robinson buffers at various pH. SEM images shown in *Figure 3.3* revealed no detectable morphological changes in HAP after it was treated in either extreme acidic (pH 2) or alkaline (pH 12) conditions.

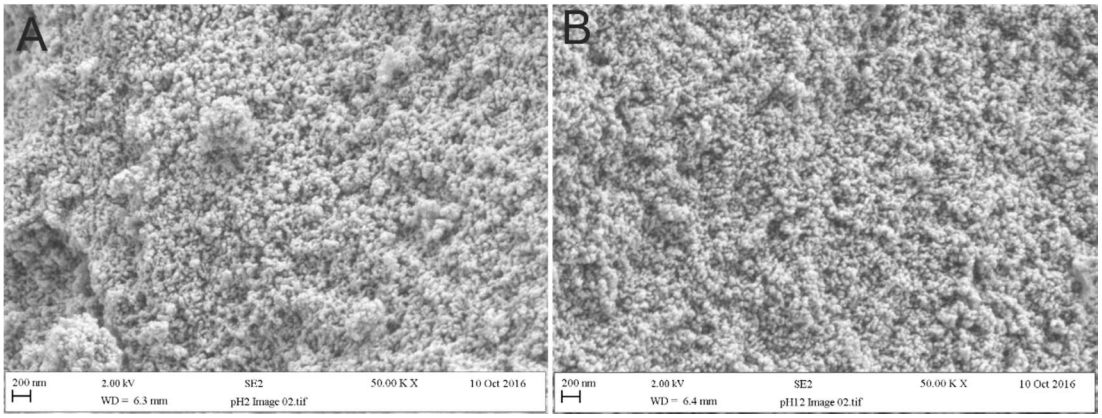


***Figure 3.3*** *SEM images of HAP_5 treated in highly acidic (A) and alkaline (B) conditions*

Subsequently, XRD analysis was performed to investigate any phase changes or fluctuations within the crystallinity after pH treatments. The obtained patterns shown in *Figure 3.4* remained identical throughout all pH values tested, confirming that the hexagonal HAP phase was unaffected after exposure to aqueous buffer solutions over the whole pH range.

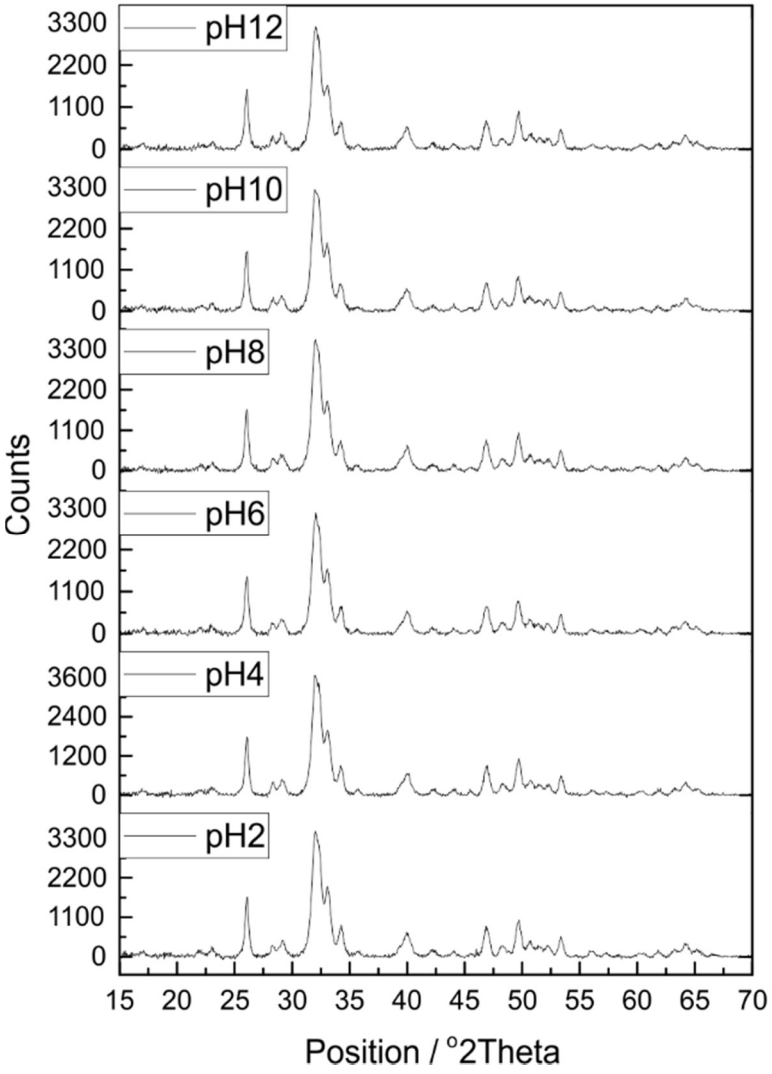


***Figure 3.4*** *XRD patterns of HAP_5 after treatment at full range of pH*

Next, attention was turned to FTIR and the fundamental vibrations modes of HAP. As shown in *Figure 3.5,* the most intense peak at 1021 $cm^{-1}$ and another peak at 1089 $cm^{-1}$ corresponded to the $v_3$ P-O stretching bond. The band at 962 $cm^{-1}$ was attributed to the $v_1$ P-O stretching bond and the relatively weak signal at 3568 $cm^{-1}$ was assigned to the OH group.[11]

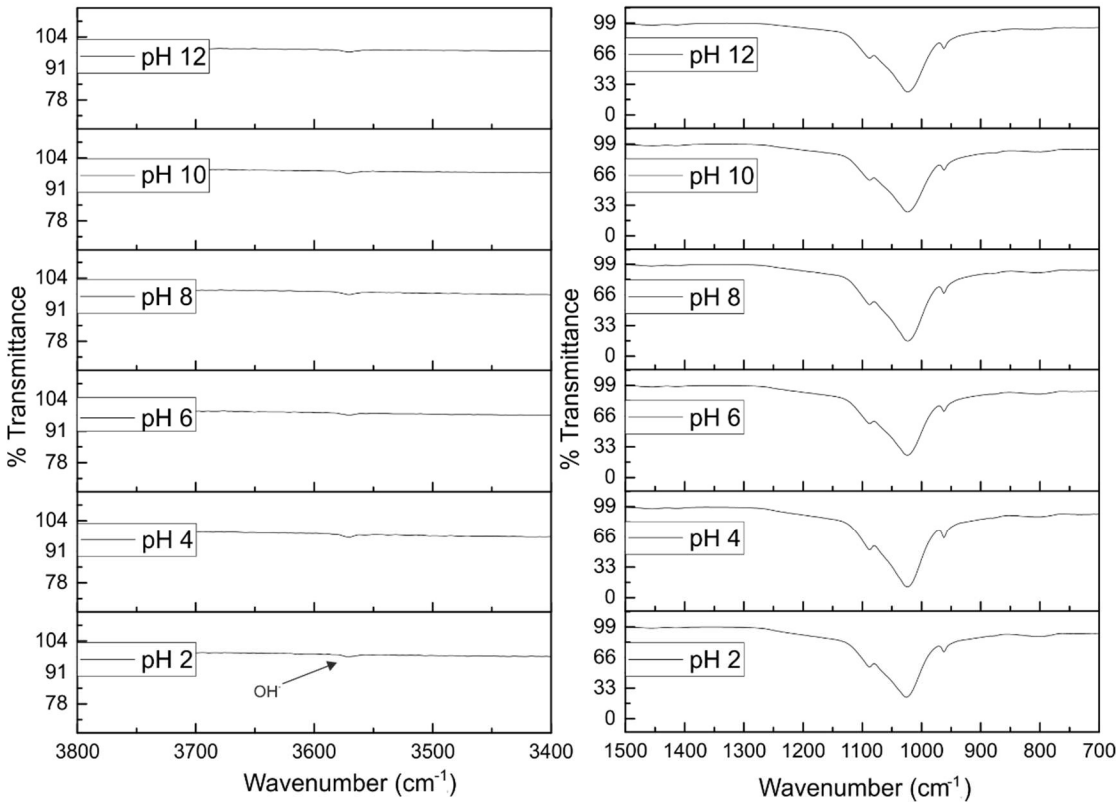


***Figure 3.5*** *FTIR spectra of HAP_5 after chemical treatment at different pH*

Following SEM and XRD analysis, the FTIR spectra provided further evidence of the stability of HAP to acid/alkaline solutions by the presence of identical spectra over the entire pH range. However, it is important to note that the solubility of HAP in different pH varies, but even though the solubility of HAP increases by a factor of approximately $10^4$, the absolute values of solubility product are extremely low across the pH scale, which makes HAP practically insoluble.[12, 13] This suggests that any changes to the apatite structure due to dissolution would be negligible, which was confirmed by the identical XRD spectra recorded (*Figure 3.4*).

Subsequently, BET surface area and pore volumes were studied to analyse any change after pH treatments. As shown in *Table 3.1,* the surface area of HAP increased after HAP was treated in acidic media and decreased after treatment in basic media, while pore volume remained relatively steady, which was the result of the higher concentrations of $OH^-$ ions at progressively higher pH. It has been well described in *Chapter 2* that surface $OH^-$ ions are required for the crystallisation and growth of HAP.[14] In view of that, the results obtained imply that $OH^-$ ions remaining from pH

treatments could cause further reactions of the HAP during the heating step (300°C) that was required by BET surface area analysis, which ultimately initiated some agglomeration of particles with an associated reduction in surface area. The extent of this reaction increased with higher pH, due to the increase in $OH^-$ concentration.

***Table 3.1*** *Nitrogen adsorption porosimetry of HAP after pH treatments*

| pH | Surface Area /$m^2g^{-1}$ | Total Pore Volume /$cm^3g^{-1}$ |
|---|---|---|
| **As synthesised** | 84.9±0.3 | 0.49 |
| **2** | 121.9±0.8 | 0.56 |
| **4** | 105.4±0.7 | 0.44 |
| **6** | 87.8±0.6 | 0.46 |
| **8** | 79.6±0.8 | 0.42 |
| **10** | 62.7±0.3 | 0.42 |
| **12** | 55.4±0.2 | 0.46 |

All the aforementioned results revealed that HAP remained stable in all values of pH. This is a very important feature, since there is a possibility of slightly acidic conditions in the exhaust of the engine as has been previously described.[10]

### *3.3.2 Influence of temperature on stability of HAP*

Mesoporous HAP (*HAP_5*) was examined for resistance to high temperatures, as described in *section 3.2.2*. First, any morphological changes were investigated *via* SEM. The obtained images revealed significant crystal growth as the temperature increased. Heating in air caused the transformation of rod like crystals with well-defined edges into larger agglomerated spherical particles, observed from 700°C as shown in *Figure 3.6*. This sintering of particles and the associated increase in particle size is typical of Ostwald ripening behaviour, described in *section 3.1.1*. These observations agree with those reported in the literature. For example, Savino *et al.* reported that the heat treatment of HAP coatings to 700°C in dry air caused the edges of the crystals to become more rounded.[15] On the other hand, Sun *et al.* showed that the particle size and shape of HAP were unchanged after heating to 600°C, but the HAP building units sintered together after heating at 800°C.[14]

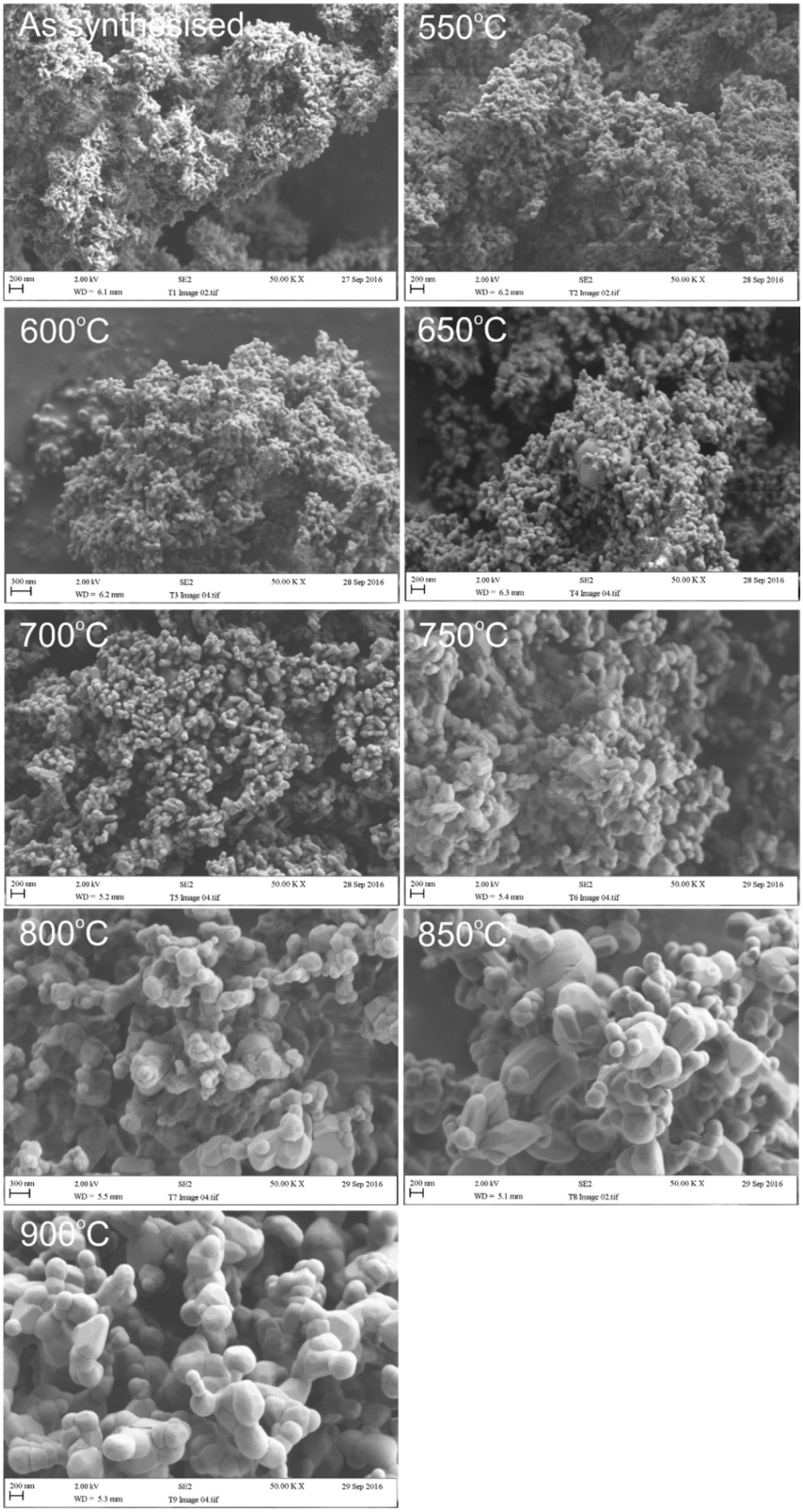


***Figure 3.6*** *SEM images of HAP_5 after thermal treatments at different temperatures*

Then, crystallinity and changes within the phases of HAP were investigated *via* XRD. As presented in the *Figure 3.7,* diffraction peaks became sharper as temperature increased, thus higher temperatures caused improvements in the crystallinity of HAP. However, as described by Rapacz-Kmita *et al.* HAP undergoes dehydroxylation to oxyhydroxyapatite (OHAP), which lead to further decomposition into several calcium phosphates, such as TTCP or β-TCP.[16]

From the obtained diffraction patterns, OHAP peaks started to appear at 650°C, which indicates that, at this temperature, the dehydroxylation process took place in a small proportion. Also, as expected, this process became more significant when the temperature increased from 700°C to 900°C, where the characteristic peaks of OHAP appeared around 31 and 33 °2Theta(degrees), as marked in red in *Figure 3.7*. Further decomposition of HAP to β-TCP was simultaneously observed from 750°C where a small peak appeared at 47 °2Theta(degrees), highlighted in blue in *Figure 3.7*, however it was not fully separated from another peak that belonged to HAP.

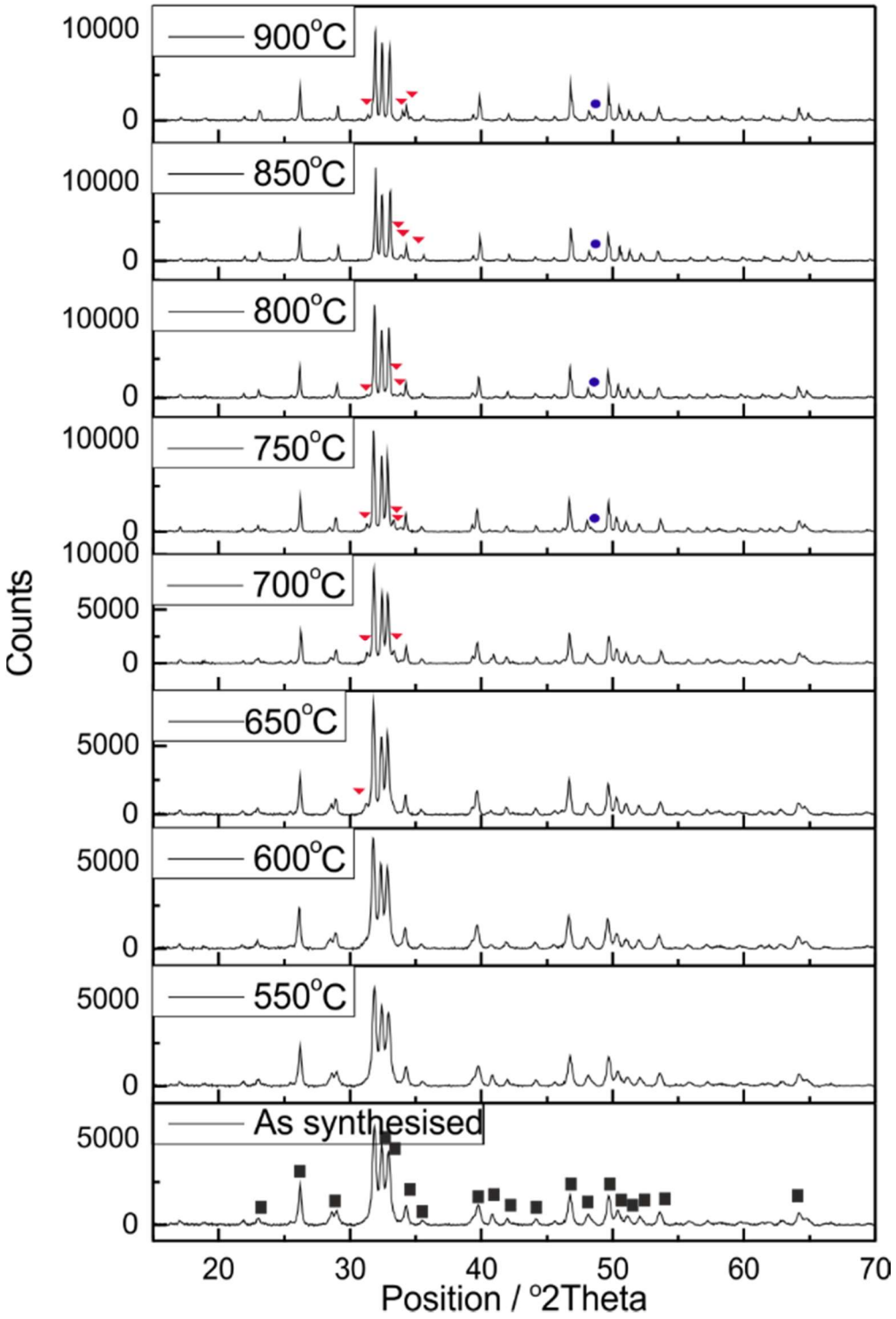


***Figure 3.7*** *XRD patterns of HAP_5 after different temperature treatments.* ■ *- HAP;* ▼ *- OHAP;* ● *- β-TCP*

Furthermore, the phenomena of dehydroxylation and decomposition processes within HAP can be distinguished *via* FTIR studies. As observed in *Figure 3.8*B, the P-O vibration band at 1082 $cm^{-1}$ became broader as the temperature increased, suggesting the transformation of HAP to β-TCP.[11] According to the report by Savino *et al.,* where HAP was electrochemically functionalised with fluoride to increase the thermal resistance of the material, unmodified HAP decomposed to β-TCP at 600°C, which was lower than that reported here.[15] Following this, the weak O-H band at 3567 $cm^{-1}$ disappeared due to the preliminary dehydroxylation process and subsequent formation of OHAP (*Figure 3.8* A).

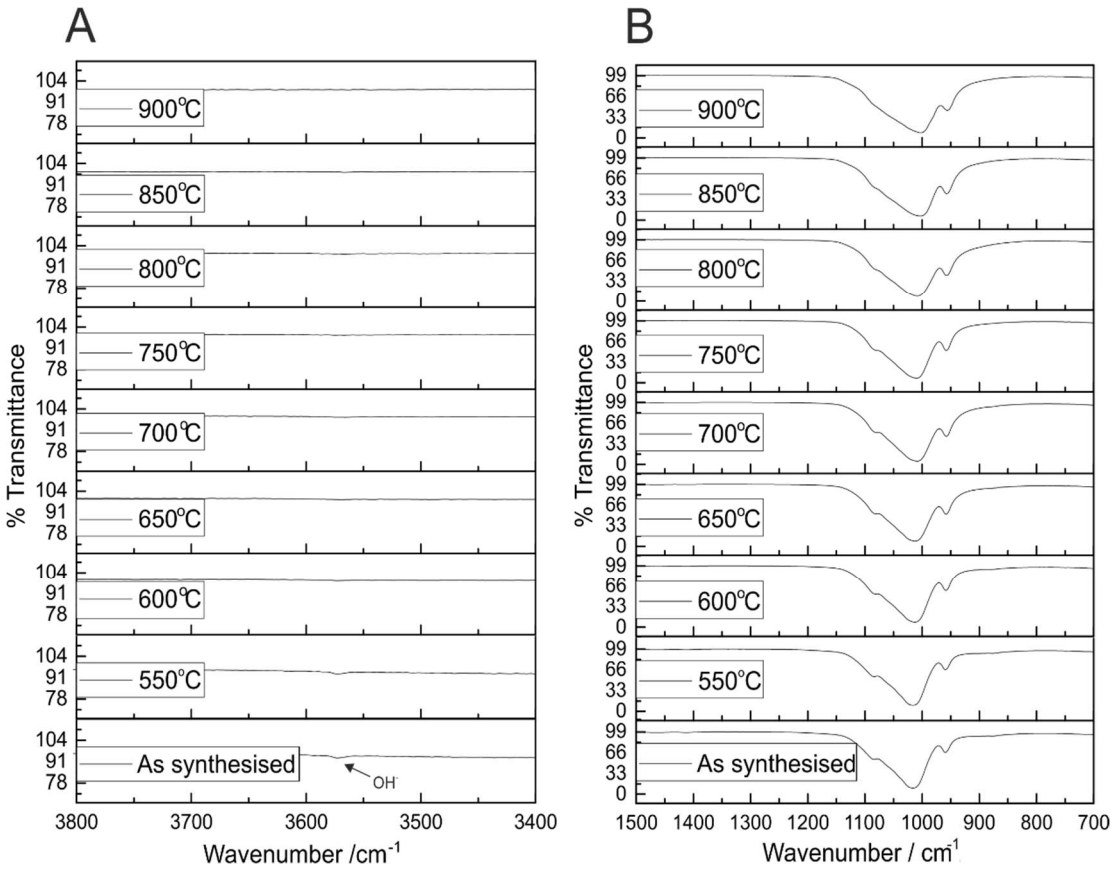


***Figure 3.8*** *FTIR spectra of HAP_5 treated at different temperatures focused on OH group (A) and phosphate group (B)*

Nitrogen adsorption isotherms confirmed type IV adsorption behaviours, which is a characteristic feature of mesoporous materials, as shown in *Figure 3.9A*. The only detectable amounts of nitrogen adsorbed by capillary condensation occurred above a relative pressure of approximately 0.95.

This behaviour can be explained by the adsorption that occurred between HAP particles. However, the absence of any capillary condensation below 0.95 confirmed that mesopores were not present within the particles.[17, 18] The pressure at which capillary condensation occurred increased further with increasing temperature treatment of HAP, and reached a maximum of 0.98 after treatment at 900°C.

Consequently, the BJH pore size distributions, shown in *Figure 3.9B,* provided additional confirmation of the presence and dimensions of mesopores within HAP. The sample treated at 550°C contained mesopores with an approximate mean diameter of 50 nm, which is the upper limit of the mesopore classification and corresponds to the dimensions at which it is possible to confirm the porosity between particles.

Thereafter, the mean pore diameter increased with temperature, while the surface areas were significantly reduced. Taken together these trends resulted from the greater distances between the larger particles that formed after heating at progressively higher temperatures, and it agrees well with the SEM images (*Figure 3.6*). This effect was particularly evident for the sample prepared at 900°C, where the mean pore diameter was so high it appeared beyond the BJH operating range.

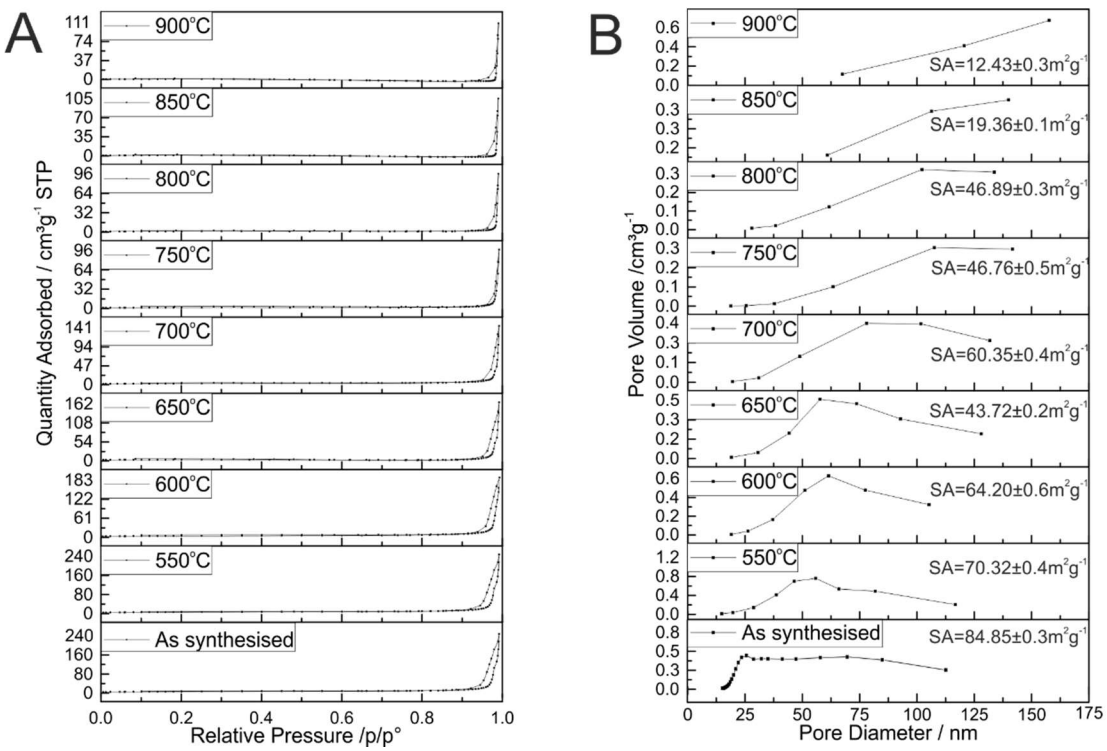


***Figure 3.9*** *Nitrogen adsorption isotherms (A) and BJH pore diameters of HAP treated in range of temperatures (B), with corresponding BET surface areas (SA)*

Taking into consideration that the running temperatures of an engine are usually below 600°C and the results described above, it is fair to say that, for this particular application, HAP is relatively stable and will not undergo dehydroxylation or/and de-composition at these temperatures.

### *3.3.3 Stability of HAP under mechanical disturbances*

In the last study, ultrasound was employed to introduce mechanical disturbances to HAP, and its influence on the stability of the material was examined. Based on the SEM images shown in *Figure 3.10*, it was clear that the morphology of HAP remained stable after 1 hour continuous exposure to ultrasonic treatment.

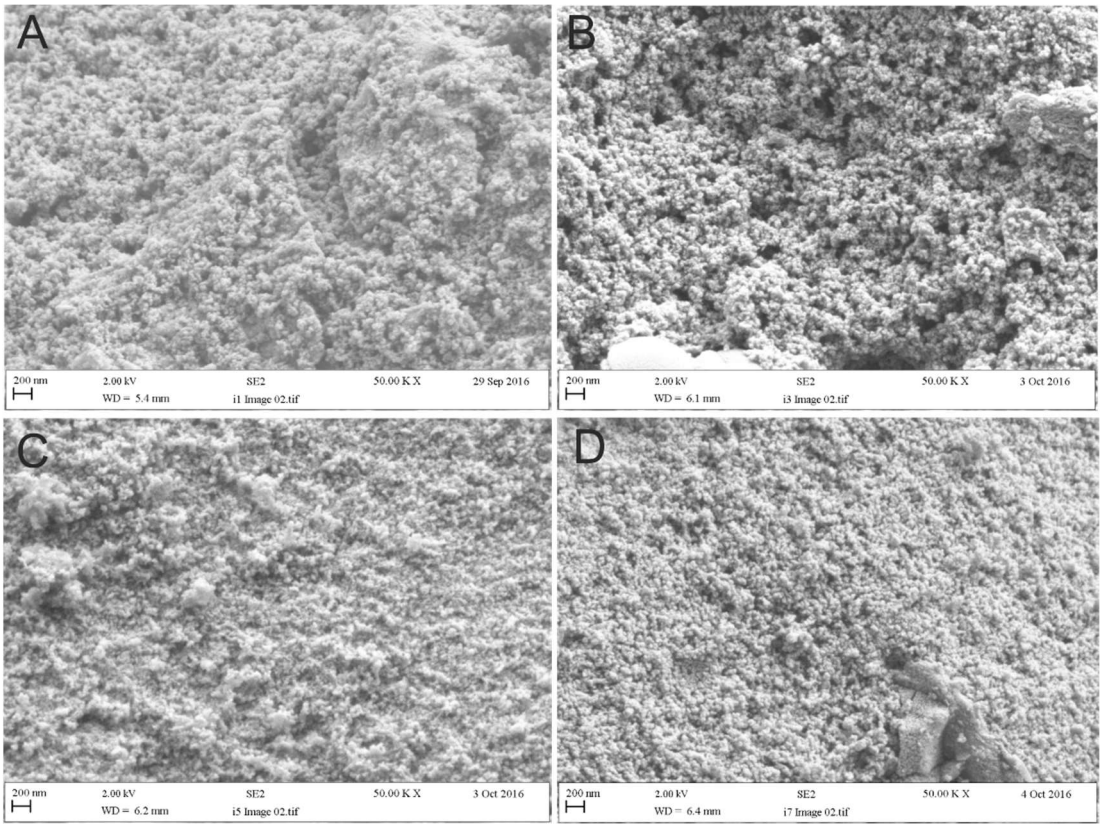


***Figure 3.10*** *SEM images of HAP (A) and after ultrasound treatment for 20 min (B), 40 min (C) and 60 min (D)*

Based on XRD patterns obtained (shown within *Figure 3.11*) it was also clear that HAP is fully stable and none of the secondary phases were observed. Moreover, the crystallinity of HAP remained the same throughout all ultrasonic exposure times.

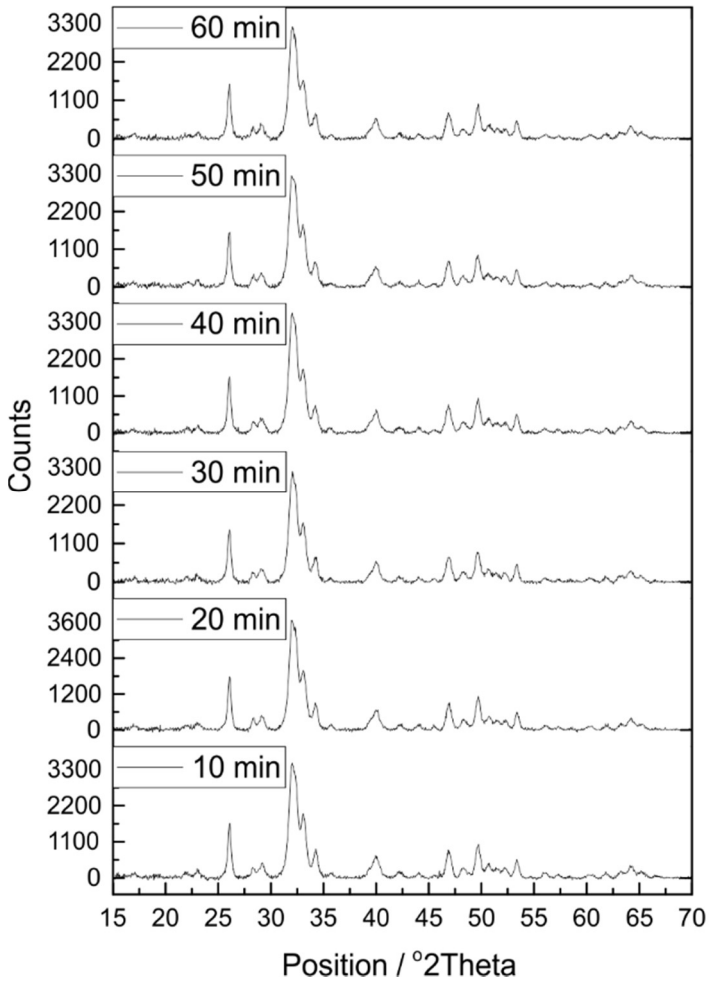


***Figure 3.11*** *XRD patterns of HAP after different times of ultrasonic treatments*

On the other hand, the surface areas of the treated samples varied by less than 1% over the full range of ultrasound used. The results obtained are in agreement with those reported in the literature. For example, the mechanical stability of HAP scaffolds, prepared by a sponge replica method, was evaluated by a uniaxial compression test, which calculates the strength of HAP by measuring the stress value at failure. Results obtained showed that the mechanical strength of this HAP was practically unchanged following 28 days' immersion in simulated body fluid.[19] Moreover, in a different study, where HAP was deposited on titanium substrates, the coating was sufficiently strong to the point that scratching with a diamond indenter was required to physically remove HAP.[20] In view of that, the obtained results proved that *HAP_5* is stable after the severity of a 1 hour ultrasonic treatment, thus it supports the choice of utilisation of HAP as a catalytic base for the metals in a dual-fuel engine.

## 3.4 Conclusion

This chapter has reported the investigation of the stability of mesoporous HAP after pH, thermal and mechanical treatments. It was found that HAP is fully stable under mechanical disturbances as well as when it is exposed to different pH. This was confirmed by SEM, BET and XRD.

On the other hand, under temperature treatments HAP started to dehydroxylate above 650°C to OHAP with further decomposition to β-TCP and TTCP above 750°C. Also, SEM revealed a significant growth of crystals after exposure to the high temperatures. Nevertheless, preliminary dehydroxylation and resulting phase transformations of HAP began from 650°C. Therefore, since this is above the operating temperature of dual-fuel engines, the obtained results confirmed the suitability of HAP as a catalyst support.

## 3.5 References


1. Y. Fang, D. K. Agrawal and D. M. Roy, *THERMAL-STABILITY OF SYNTHETIC HYDROXYAPATITE*, 1994.
2. P. Alberius-Henning, E. Adolfsson, J. Grins and A. Fitch, *Journal of Materials Science*, 2001, **36**, 663-668.
3. K. A. Gross, C. C. Berndt, P. Stephens and R. Dinnebier, *Journal of Materials Science*, 1998, **33**, 3985-3991.
4. T. Wang, A. Dorner-Reisel and E. Müller, *Journal of the European Ceramic Society*, 2004, **24**, 693-698.
5. C.-J. Liao, F.-H. Lin, K.-S. Chen and J.-S. Sun, *Biomaterials*, 1999, **20**, 1807-1813.
6. in *Ceramic Materials: Science and Engineering*, Springer New York, New York, NY, 2007, DOI: 10.1007/978-0-387-46271-4_24, pp. 427-443.
7. L. C. D. Jonghe and M. R. Rahaman, in *Handbook of Advanced Ceramics*, Elsevier, USA, 2003, DOI: http://home.agh.edu.pl/~nmos1/TPCP/spring2015/Sintering.pdf, ch. 4, pp. 187-194.
8. D. V. Alexandrov, *Journal of Physics and Chemistry of Solids*, 2016, **91**, 48-54.
9. A. Baldan, *Journal of Materials Science*, 2002, **37**, 2171-2202.
10. A. Kuang, M. Kuang, H. Yuan, G. Wang, H. Chen and X. Yang, *Applied Surface Science*, 2017, **410**, 505-512.
11. S. Kannan and J. M. F. Ferreira, *Chemistry of Materials*, 2006, **18**, 198-203.
12. M. J. Larsen and S. J. Jensen, *Arch Oral Biol*, 1989, **34**, 957-961.

13. S. Larsen, *Nature*, 1966, **212**, 605-605.
14. R. Sun, K. Chen, Z. Liao and N. Meng, *Materials Research Bulletin*, 2013, **48**, 1143-1147.
15. K. Savino and M. Z. Yates, *Ceramics International*, 2015, **41**, 8568-8577.
16. A. Rapacz-Kmita, C. Paluszkiewicz, A. Ślósarczyk and Z. Paszkiewicz, *Journal of Molecular Structure*, 2005, **744–747**, 653-656.
17. C. T. Kresge, M. E. Leonowicz, W. J. Roth, J. C. Vartuli and J. S. Beck, *Nature*, 1992, **359**, 710-712.
18. D. Zhao, J. Feng, Q. Huo, N. Melosh, G. H. Fredrickson, B. F. Chmelka and G. D. Stucky, *Science*, 1998, **279**, 548.
19. F. Gervaso, S. K. Padmanabhan, F. Scalera, A. Sannino and A. Licciulli, *Materials Letters*, 2016, **185**, 239-242.
20. A. V. Zavgorodniy, O. Borrero-López, M. Hoffman, R. Z. LeGeros and R. Rohanizadeh, *Journal of Biomedical Materials Research Part B: Applied Biomaterials*, 2011, **99B**, 58-69.

# Chapter 4: Dry Reforming of Methane over Pd, Ni and PdNi/Hydroxyapatite

# 4.1 Introduction

This chapter describes how Pd and Ni metals were first loaded on the surface of previously prepared HAP *via* two standard procedures: Ion Exchange (IE) and Incipient Wetness Impregnation (IW). Changes in the structure of HAP were studied as a consequence of metal loading and any sources of interaction between the metal and the support were also investigated. A catalytic testing rig was built in-house in order to reproduce the oxygen lean conditions present in the engine and $CO_2$ was used as an oxidant for $CH_4$ reforming. The catalytic activity of all prepared samples was then explored in the dry reforming of methane (DRM) over a ramp of temperatures. The most active catalyst was further investigated for its stability in on stream reactions. After the catalytic tests, the coking process was studied as a major cause of deactivation of the catalysts. Results within this chapter have been published in Fuel, 2017, 208, 314-320.

## *4.1.1 Mechanism of Dry Reforming of Methane*

Dry reforming of methane is a well-studied reaction with scientific as well as industrial importance and was first reported in 1928 by Fisher and Tropsch over Ni and Co catalysts.[1] It has received special attention in recent years as a potential technique to reduce greenhouse gas (GHG) emissions *i.e.* $CH_4$ and $CO_2$, the two most important GHGs. Furthermore, the reaction product is a synthesis gas (syngas), which is a mixture of $H_2$ and CO and is the key intermediate in the chemical industry and can be extensively used to produce higher alkanes, ammonia or methanol as well as for the Fisher-Tropsch process, summarised in *Figure 4.1*.[2]

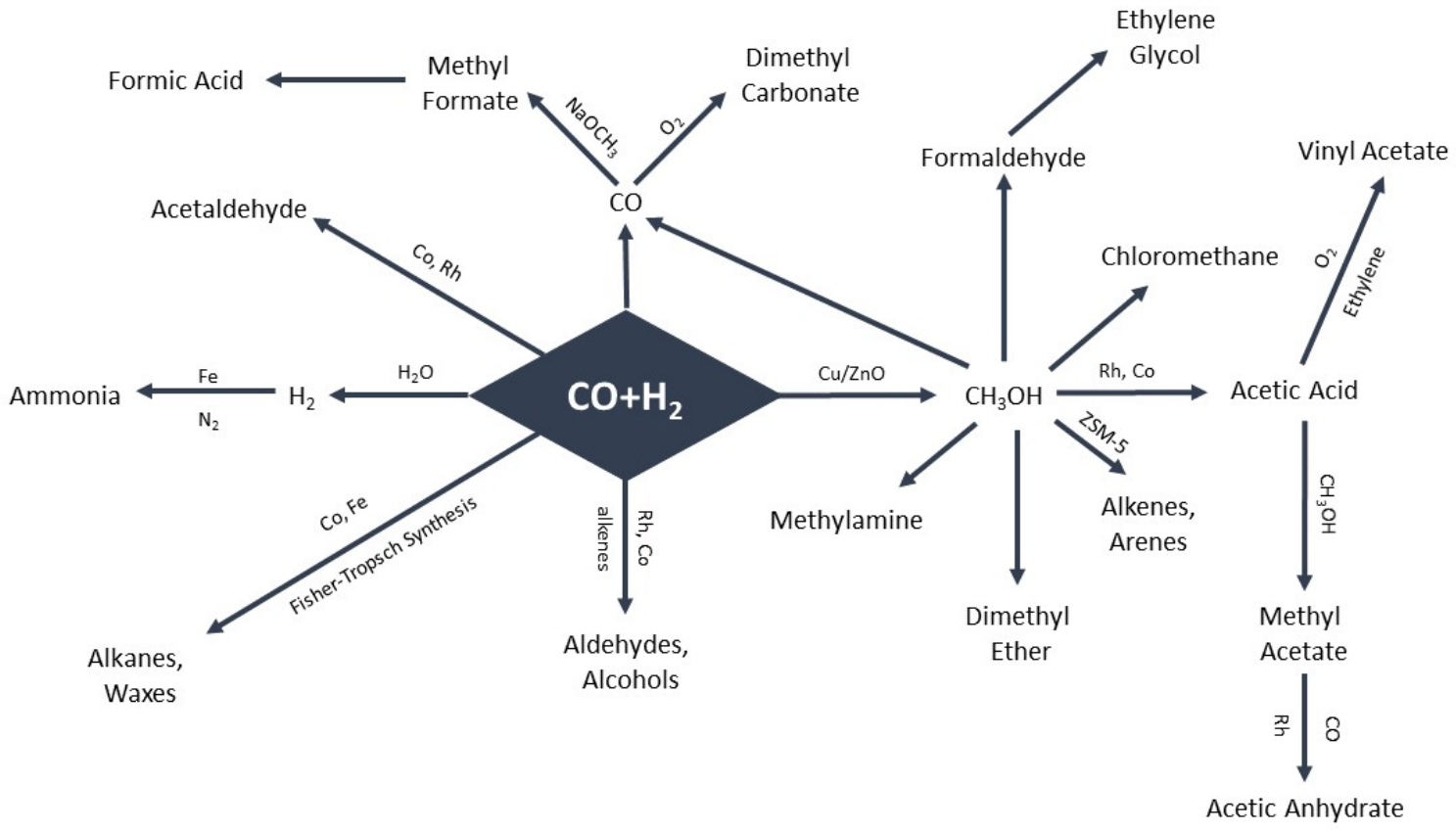


***Figure 4.1*** *Selected industrial applications of synthesis gas*

However, since $CO_2$ exhibits good thermal stability, DRM is an extremely endothermic reaction (*Equation 4.1*), thus it requires an external energy source to attain high equilibrium conversions to syngas.

$$CH_4 + CO_2 \leftrightarrow 2CO + 2H_2, \quad \Delta H^\circ = 247\ kJ\ mol^{-1} \qquad 4.1$$

It is well known that the theoretical equilibrium conversions can be calculated *via* the Gibbs free energy minimisation method in order to understand and optimise the conditions required for DRM. A reaction is thermodynamically favourable when ΔG<0. Therefore, according to the ΔG calculations, DRM is not spontaneous at temperatures lower than 643°C, as below this temperature ΔG is positive. However, in real applications the required operating temperature to convert over 80% of $CH_4$ and $CO_2$ in a molar ratio of 1:1 was found to be 800°C.[3, 4] For this reason, catalysts have been employed to reduce the activation energy and enhance the DRM reaction at lower temperatures.

Noble metals, mostly Pt, Pd, Rh, Ru and Ir have been extensively studied on numerous supports, and have reported high activity towards DRM, as summarised in a comprehensive recent review.[5] Nevertheless, due to the high cost and limited accessibility of noble metals, various transition metals, like Ni, Fe, Zr and Co have also been investigated. Regarding catalytic activity towards methane, from a comparison of various noble and transition metals, Pd and Ni have been found to be the most active for this reaction.

There is an agreement in the literature that the mechanism of DRM is a bifunctional process: $CH_4$ is activated on metal and $CO_2$ is activated on the acid/basic sites of the support.[1] Nevertheless, the most kinetically significant and important step in the DRM reaction is the activation of $CH_4$, which happens by dissociation of $CH_4$ on the metal of the catalyst. In view of this, there are two possible ways that $CH_4$ dissociates; direct and indirect *via* the formation of intermediates with oxygen from the oxidant or, what is very interesting, from the support. Thus, the presence of oxygen species in the lattice of the support directly helps in the $CH_4$ dissociation

process. This suggests that the activation of $CH_4$ during DRM occurs at the metal-support interfacial sites, not the metal alone.

Nevertheless, it is generally believed that activation of methane at lower temperatures (<550°C) proceeds through an indirect route and begins to dissociate directly at higher temperatures.[1] This hypothesis is supported by density functional theory (DFT), based on which methane dissociates into surface $CH_x$ species ($CH_4 \leftrightarrow CH_3 \leftrightarrow CH_2 \leftrightarrow CH$) and surface H atoms, followed by oxidation into $CH_xO$, which based on the calculations is more favoured than dissociation into C and H. Finally, oxidised $CH_xO$ species subsequently decompose to CO and $H_2$. Moreover, isotopic studies suggest that the dissociation of C-H bonds is the rate determining step in the DRM.[6] In fact, most of the studies agree that DRM is typically a first order reaction and the activation of $CH_4$ is independent of $CO_2$ concentration; *i.e.* $r = kP_{CH_4}^{a}$ .[7, 8] However, in the absence of $CO_2$, methane is more likely to undergo thermal cracking, rather than dissociation, due to the high temperatures involved. In consequence, observations of other researchers maintain that the rate of dissociation and formation of CO and $H_2$ strongly depends on the concentration of $CO_2$ as well as $CH_4$, also in order to form pure syngas without any impurities.[9, 10]

### *4.1.2 Influence of metal precursors and methods for the preparation of catalysts*

The preparation method of a metal based catalyst has a strong influence over its physicochemical properties and consequent catalytic activity. Their higher catalytic activity is the result of the strong interaction between the metal and the support and the higher dispersion of metal particles, which in addition leads to lower carbon deposition, thus increasing the lifetime of the catalyst.

The two main experimental approaches employed to load the metal upon the surface of the support are ion exchange (IE) and incipient wetness impregnation (IW) due to their simplicity and high efficiency. The IE method occurs in solution and involves constant stirring of the support together with the metal precursor, usually for several days, at room temperature.

On the other hand, a typical IW methodology employs drop casting of metal, previously dispersed in a minimum amount of water, onto the solid support, hence this approach ensures that 100% yield of the metal used is deposited on the support, since no solutions are involved. Nevertheless, the main downside of IW protocol is that there is no direct control over the metal dispersion, which can result in the formation of non-uniform surface metal aggregates. In fact, it has been agreed that higher catalytic performance is exhibited by metal doped samples prepared using the IE approach and is due to the incorporation of metal oxide ions with the support present in the solution, where better dispersed and smaller particles are formed.[11]

Recently, newly developed techniques have been introduced to overcome the problems reported with conventional chemical methods. An example of a novel approach involves plasma treatment, which has been reported to form strong metal-support interactions, as well as highly dispersed and small metal particles that may improve the stability and activity of the catalyst. Moreover, plasma treatments exclude any residue contaminations from metal precursors and sample loss after recovery from the solution, as happens in conventional chemical methods.[12]

However, the main disadvantages of employing plasma are that it requires high energy consumption, involves complicated setups and is more expensive when compared to simple preparation techniques, making it more difficult to employ on an industrial scale.

Another important aspect to consider in the preparation of metal based catalysts is the metal precursor employed, because the nature of the metal precursor can influence the interaction between the metal and the support, but also can affect the dispersion of the metal on the surface.[13] Kim *et al.* investigated various Ni salts to load γ-$Al_2O_3$ and showed that the catalysts were strongly dependent upon the salt employed. Since nitrate salts exhibited higher solubility when compared to other salts, it formed smaller particles that were better distributed on the support, hence showed higher activity in hydrochlorination reactions.[14]

On the other hand, the influence of halogens, like $Cl^-$ ions, originating from the precursor salt has been described as a possible poisoning effect on the catalysts for various methane reactions. This is due to the application of metal chloride salts upon the support, and often conventional activation treatments, like calcination or metal reduction in the flow of a reducing agent, do not allow the complete removal of chloride ions.[15] However, the mechanism by which $Cl^-$ ions would act as strong inhibitors is not yet clearly established. It is generally agreed, that regardless of the origin of the $Cl^-$ ions, they are mainly localised on the support after activation treatments. During the catalytic reaction towards methane, Cl ions desorb and form HCl, which then competes with the reactants for the active sites of the catalyst, blocking its availability and hence inhibiting the activity.[16]

Another type of chloride ions has been proposed to be located in the metal-support interface as a bridging species that can directly and negatively influence the adsorptive and catalytic properties of the metal. In fact, since small amounts of Cl species are present, this type is believed to be predominant in the inhibition of the catalytic activity *via* electronic effects that may affect the surface properties.[17]

Simone *et al.* reported Pd supported γ-$Al_2O_3$ for the oxidation of methane and clearly evidenced that the $Pd(NO_3)_2$ exhibited higher $CH_4$ conversions than $PdCl_2$, however $PdCl_2$ provided a smaller particle size and better dispersion of the metal throughout the support.[18] Moreover, it has been shown that the combination of excessive washing during the preparation process and reduction treatments before performing the reaction could slowly remove residual chloride and exhibit catalytic activity similar to that when nitrate salts are employed.[19]

Besides different metal precursors, the amount of metal applied on the surface of the support also plays a key role. It is interesting to note, that after a certain amount of metal loading, there was no expected increase in the conversion rate observed with increasing metal content, as reported by Bitter *et al*.[20]

Pretreatment of the metal also has a significant role in the formation of active sites, hence influencing the performance of the catalysts. Because the metallic form is described as being an active form in the dissociation of $CH_4$, various reducing atmospheres have been investigated, mostly involving $H_2$, He, $N_2$ or mixtures of those prior to the reaction. However, scientists from The University of Tokushima, Japan, proposed a redox reaction that occurs between the metal oxide and the reduced metal during the catalysis reaction, suggesting that the presence of metal oxide or a mixture of oxides and reduced metal can beneficially affect activity of the catalyst.[21]

### *4.1.3 Catalytic experimental setup*

The catalytic experimental setup typically involves the reactor where the reaction occurs over the catalyst and a detector that is usually an analytical instrument. Since the DRM has been demonstrated to be a highly endothermic reaction, isothermal operations are required to perform the reaction. There are a few reactor setups that have been investigated for this purpose, including fixed bed reactors, fluidised bed reactors, magnetised bed reactors, hollow fibre membrane reactors and microreactors.[5] Surprisingly, employing different reactors can influence the catalytic activity *via* varying the number of metallic active sites of the catalyst, but also the carbon deposition rate, explained in detail in *section 4.1.4*. Nevertheless, each reactor exhibits some limitations and differences in ease of operation, cost and maintenance. For example, a fluidised bed reactor, which consists of a suspended solid catalyst in a gas or liquid fluid, showed better $CH_4$ conversions when compared to a fixed bed reactor, where a cylindrical tube is filled with a solid catalyst and the reaction components are flowing through it. However, the fluidisation quality of the nanoparticles are the main downside of the design, which leads to inaccurate analysis.[22]

On the other hand, an obstacle for fixed bed reactors lies in handling small particles due to strong cohesive forces, however this limitation can be overcome by using a pellet press. Other reactors require higher pressures, which for the DRM can be disadvantageous from an equilibrium point of view, but on an industrial scale it is more likely that high pressure is involved. In recent years solar energy received much

attention as an unlimited energy source with no pollution involved, which could be utilised for the DRM reaction instead of conventional heating sources.[23] What makes solar cells even more exciting is the fact that hydrogen produced in the DRM reaction could be potentially stored and re-used as a main component of solar fuel. However, the main challenge regarding solar energy is its storage on a large scale without the interruptions caused by cloudiness.[24]

Besides the reactor, different detectors have also been investigated to analyse the products of DRM, including infrared, Raman spectroscopy and gas chromatography. However, each technique carries its own set of advantages and disadvantages. Infrared spectroscopy is a simple to operate and inexpensive technique that is capable of performing online measurements throughout the reaction, which is an important advantage. However, not all products of the reaction can be detected using this system.

On the other hand, gas chromatography exhibits an excellent limit of detection for the components of DRM when coupled to a thermal conductivity detector (TCD), which measures the difference in the conductivity of the gases, improving the intensity of the acquired signal. However, online measurements cannot be performed, but the sample collected from the reactor in the injector loop is analysed at the time of collection.

Even though both methodologies are the most widely employed to study the reaction components from DRM, taking into account the excellent limit of detection of GC, it is probably the superior technique to analyse the products of DRM, when tests are performed on a lab scale.[25]

### *4.1.4 Carbon deposition*

The deactivation of the catalyst remains a serious obstacle for scaling up the catalytic reforming system, with the main problem arising with the coking process. Since both $CH_4$ and $CO_2$ are carbon containing molecules, carbon is inevitably formed and deposited upon the catalysts during the DRM reaction, blocking the availability of the metal to perform the reaction (*Equations 4.2-4.5*).

$$2CO \rightarrow CO_2 + C, \Delta H = -172\ kJ\ mol^{-1} \quad 4.2$$

$$CH_4 \rightarrow 2H_2 + C, \Delta H = 75\ kJ\ mol^{-1} \quad 4.3$$

$$H_2 + CO \rightarrow H_2O + C, \Delta H = -131\ kJ\ mol^{-1} \quad 4.4$$

$$2H_2 + CO_2 \rightarrow 2H_2O + C, \Delta H = -90\ kJ\ mol^{-1} \quad 4.5$$

There are various possible reactions that take place during the coking process, such as CO disproportionation called as Boudouard reaction (*4.2*), $CH_4$ cracking (*4.3*), reverse water gas shift (*4.4*) and steam formation *via* $CO_2$ reforming (*4.5*). Moreover, $CH_4$ cracking is endothermic while the others are exothermic. In consequence, exothermic reactions are favoured to proceed at lower operating temperatures, while $CH_4$ cracking is feasible at higher temperatures. Hence, catalysts can undergo severe deactivation due to the coking process regardless the operating temperature. It is interesting to note, however, that CO disproportionation (*4.2*) is energetically more favourable, thus it is generally believed that it makes a more important contribution to the coking process.

Moreover, Wang *et al.* inferred, based on free Gibbs energy values, that the coking process is favoured to occur in the range 557-700°C, thus there is a significant urge to develop a catalyst with enhanced activity below these temperatures.[26]

On the other hand, various studies have also demonstrated that noble metals are more resistant to carbon deposition than transition metals. Moreover, supports that exhibit basic sites within the structure showed better stability towards carbon deposition than acidic supports.[1] Thus, utilisation of HAP as a support of the catalyst brings additional advantages.

Coke can be formed in three different forms. The first form is monoatomic $C_\alpha$ that is deposited around 380°C and can be oxidised at a temperature higher than 600°C. Another form is whisker carbon, $C_\beta$, which can be formed directly by the oxidation of $C_\alpha$ and the last is graphitic carbon, $C_\gamma$, which is the most stable out of all carbon species. In view of that, it is agreed that $C_\alpha$ and $C_\beta$ are the main carbon forms that induce deactivation of the catalyst.[27]

# 4.2 Experimental

## *4.2.1 Preparation of metal doped HAP*

To apply metals upon the surface of the synthesised HAP, two standard approaches were employed: Ion exchange (IE) and Incipient Wetness impregnation (IW). For IE catalysts, in order to achieve ˜3 wt% metal on surface of HAP, which has been described as the most active in catalytic reactions REF, 50 mg of metal salt ($PdCl_2$, $Pd(NO_3)_2$, $Ni(NO_3)_2$ or NiO) was dissolved in 100 mL of deionised water, then added to HAP (1 g) and the resulting mixture was stirred for three days at room temperature, filtered, dried at 60°C for 3 hours and calcined at 550°C for further 3 hours.

For the IW procedure, 50 mg of metal salt was dissolved in a minimal amount of deionised water and dripped onto 1 g of calcined HAP, carefully mixed, dried at 60°C for 3 hours and calcined at 550°C for further 3 hours.

## *4.2.2 Catalyst testing reactor*

The catalytic activity of each sample was studied *via* an in-house built catalysis testing rig using a quartz fixed bed reactor, shown in *Figure 4.2*, placed inside a temperature controlled furnace (Carbolite type 3216, Tempatron, PID500/110/330).

A sample of catalyst (0.2 g) was placed in a quartz tube (10 mm diameter, 1 mm thickness) between quartz wool plugs. $CH_4$ and $CO_2$ gases were supplied from lecture bottles (CKGAS filled to 200 Bar at 15°C) and regulated using single stage CONCOA 302 series gas regulators. The pressure of each gas was set to 1.0 bar. The $CO_2$ line was heated (red line) to prevent dry ice formation, and hence line blockage due to pressure changes from the bottle and regulator. Helium was provided from the main line stream available at a pressure of 3.45 bar and $H_2$ was supplied from a hydrogen generator (Balston, Parker Filtration 75-32-220) with an initial pressure of 3.0 bar. Referring to the schematic in *Figure 4.2*, the flow of each gas was maintained using

mass flow controllers (MFC, Bronkhorst UK model F-201CV), controlled through the FLOW-BUS software *(1).*

A feed mixture *(2)* of 100 mL $min^{-1}$ comprising $CH_4$:$CO_2$:He equal to 5:5:90 was used in all catalytic tests. The mixture of gases were then directed either to a bypass *(4)* to obtain a control response for each gas input, or reactor *(3)* where the catalyst was placed. The line after the reactor (5) was heated to 120°C using glass webbing tape (XtremeFlex, Briskheat GW25x1.5) that was adjusted *via* a Tempatron PID500 controller to prevent condensation of water in the line.

The reaction products were monitored by a Hewlett Packard 5890 series II gas chromatograph equipped with a GS-GASPRO column (60 m x 0.32 mm), connected to a thermal conductivity detector (TCD) *via* a 6-way gas sampling valve with a 1mL loop. Helium was employed as a carrier gas and was set to 1.37 bar, the injector temperature was set to 210°C with an oven built around the injector and set to 120°C using Tempatron PID500 controller; the temperature of the detector was fixed at 250°C. The GC program was set as follows: the initial oven temperature was set to 35°C and maintained for 10 min, then increased up to 240°C with a heating rate of 10°C $min^{-1}$ for 5 min to clear any gas excess from all the gas lines. After the GC analysis, data was collected *(6)* and the gas remains were led to the extractor *(7)*.

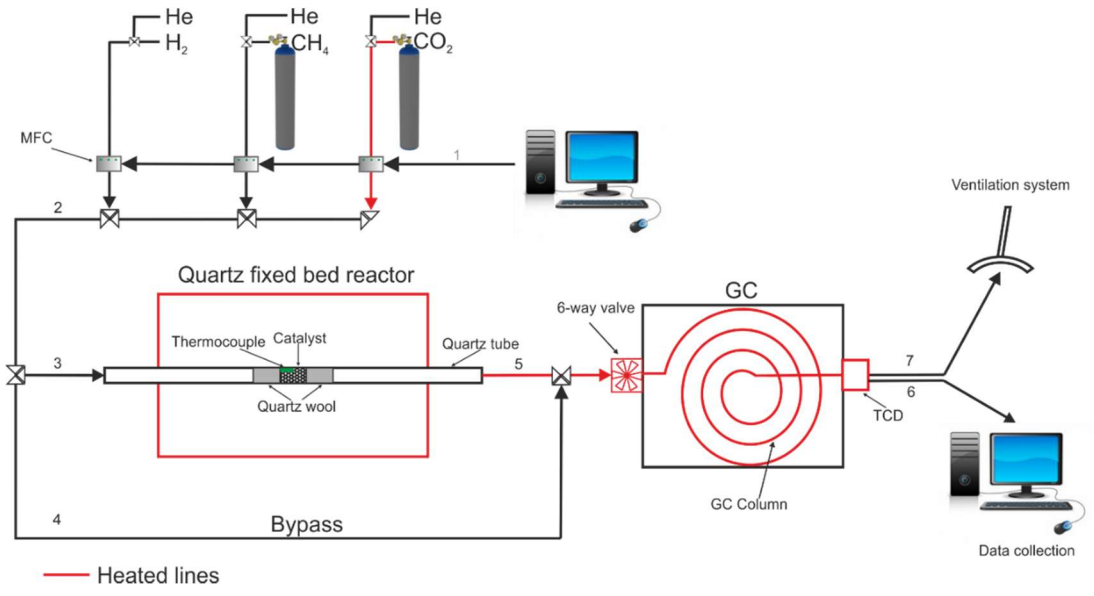

***Figure 4.2*** *Schematic representation of designed and built in-house catalyst testing reactor*

Prior to the reaction, the catalyst was reduced with a flow of $H_2$ of 30 mL $min^{-1}$ for 1 hour at 300°C. Measurements were recorded at 50°C intervals (after holding at that temperature for ~5 min) between 200 and 650°C using a heating rate of 10°C $min^{-1}$. All methane conversions were calculated using the equation below:

$$CH_4 conversion\ (\%) = \frac{(CH_4)_{in} - (CH_4)_{out}}{(CH_4)_{in}} x100 \quad 4.6$$

### *4.2.3 Stability of Pd based catalysts*

Following catalysis testing, various stability tests were performed on the sample *Pd_14.* First, the same experimental conditions were employed over a ramp of temperatures in 4 different days without any treatments between tests. Then, a continuous 24 hours stability study was carried out using the same catalyst at 300°C, monitoring conversions of $CH_4$ and $CO_2$ every one hour.

Finally, the last study was conducted in the stream of reaction at 300°C for 8 hours, whereby hourly measurements were recorded. After this time the reactor was cooled down to room temperature with a flow of He of 30 mL $min^{-1}$ and then the system was kept closed overnight maintaining an inert atmosphere.

The next day the reactor was heated back to 300°C at 10°C $min^{-1}$ in a He atmosphere and the same reaction procedure was repeated for a total of 10 consequent days, giving a total of 88 hours catalysis testing.

## 4.3 Results and Discussion

### *4.3.1 Preparation of metal doped HAP catalysts*

After the preparation of the support for the catalyst, HAP, described in *Chapter 2*, many different approaches were performed using different methods to load metals, different metal salts as precursors and HAP synthesised *via* different protocols to prepare a set of catalysts, summarised in *Table 4.1*. Metal loading corresponded to an average of 3 wt% and was confirmed semi quantitatively by using EDX. Then, the obtained materials were characterised *via* SEM.

As an example, *Figures 4.3A and B* show the agglomerated and crystalline nature of the catalyst, which remained the same after the addition of Pd onto the surface of the HAP. However, Ni doped samples (*Figure 4.3C and D*) showed a different surface morphology, with higher particle dimensions. Moreover, the surface of the Ni based materials was much smoother, suggesting different interactions between Ni and HAP.

The distribution of Pd on the surface of HAP was also studied *via* TEM. As observed in *Figure 4.4*, it is clear that Pd metal was present on the surface of HAP and did not disturb the regular arrangements of the HAP, which were described in detail by Opre *et al.*[28] Moreover, Pd particles deposited on the surface of HAP using IE protocol were nanosized and evenly distributed, as shown in *Figure 4.4B*.

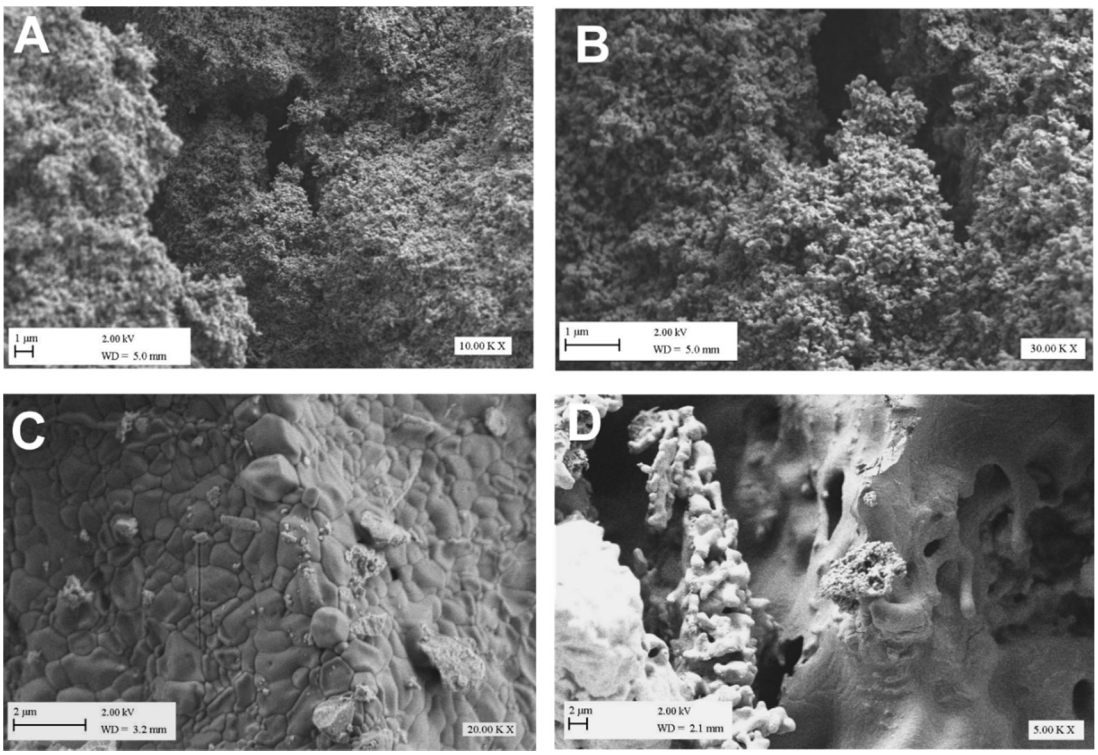

***Figure 4.3*** *Typical SEM images of Pd doped HAP (A, B) and Ni doped HAP (C, D)*

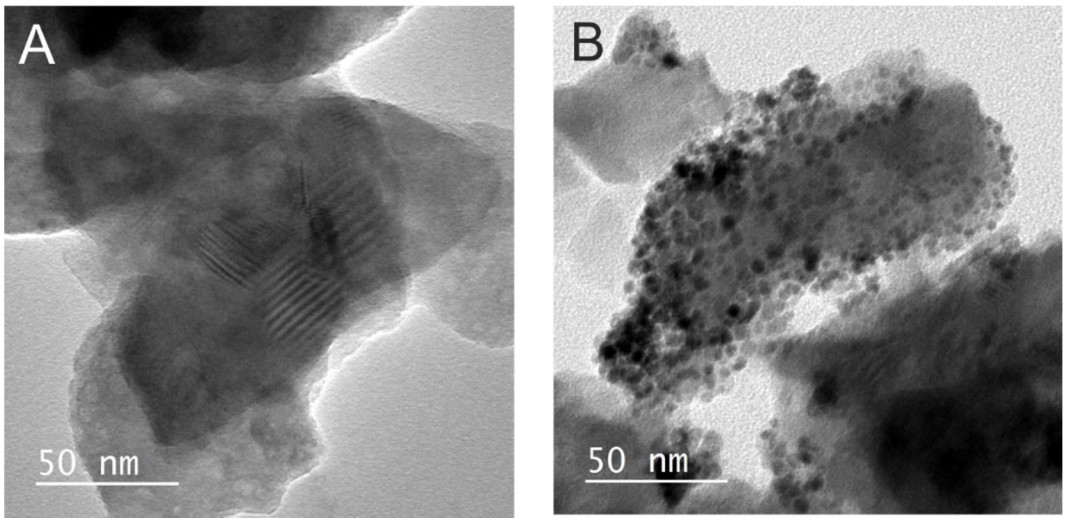


***Figure 4.4*** *TEM image of HAP without any metal (A) and with Pd upon its surface using IE (B)*

Nitrogen adsorption isotherms were employed to establish surface characteristics and related surface area of the different catalysts prepared. The values obtained are summarised in *Table 4.1,* together with the metal loading approach employed in each case, sample names, HAP utilised and the metal salt used as a metal precursor.

Note that *Comme_1* refers to a commercially available catalyst for methane, provided by G-Volution Plc., the company sponsoring the present project. Note also that the different HAP names used in the discussion below allude to the different HAP supports explained in *Chapter 2*, which were synthesised using different surfactants, as summarised in *section 2.3* and *Table 2.3*. From the results obtained, it is clear that the porosity of Ni based samples significantly decreased when compared to bare HAP, described in *Chapter 2* and altered from 25.2 to < 1 $m^2g^{-1}$. This drastic drop in surface area suggested that Ni metal created clusters that blocked the pores present in the HAP. This observation was in agreement with SEM, where Ni doped catalysts exhibited smoother surfaces, when compared to Pd based samples.

It is interesting to note that all Pd based samples revealed higher surface areas than that of bare HAP, from 24.5 to 114 $m^2g^{-1}$. This was due to the formation of polycrystalline PdO that led to a roughening of the particle surface and, in consequence, increasing total surface area of the material.[29]

The highest porosity was obtained in the sample *Pd_14* with a surface area exceeding 114 $m^2g^{-1}$, followed by samples prepared on HAP on CNRs (*Pd_16, Pd_17*).

High surface area was also observed for the sample that contains both Pd and Ni metals, possibly due to a synergistic effect.[30] Nevertheless, the results obtained were in agreement with observations of the SEM images and these differences may be crucial in the catalytic performance of the catalysts.

***Table 4.1*** *Preparation procedures of the metal loaded HAP with corresponding BET surface areas*

| *Sample* | *HAP* | *Loading method* | *Metal Salt* | *Surface Area / $m^2g^{-1}$* |
|---|---|---|---|---|
| *Pd_1* | No Surfactant | IE | $Pd(NO_3)_2$ | 24.5 |
| *Pd_2* | CTAB | IE | $Pd(NO_3)_2$ | 43.9 |
| *Pd_3* | CTAB | IW | $Pd(NO_3)_2$ | 33.3 |
| *Pd_4* | Tween60 | IE | $Pd(NO_3)_2$ | 34.6 |
| *Pd_5* | Tween60 | IW | $Pd(NO_3)_2$ | 45.6 |
| *Pd_6* | Tween60 | IE | $PdCl_2$ | 46.4 |
| *Pd_7* | Twee60 | IW | $PdCl_2$ | 44.0 |
| *Pd_8* | $C_{12}EO_9$ | IE | $Pd(NO_3)_2$ | 53.4 |
| *Pd_9* | $C_{12}EO_9$ | IW | $Pd(NO_3)_2$ | 36.4 |
| *Pd_10* | $C_{12}EO_9$ | IE | $PdCl_2$ | 27.7 |
| *Pd_11* | $C_{12}EO_9$ | IW | $PdCl_2$ | 46.5 |
| *Pd_12* | Tween60+ $C_{12}EO_9$ | IE | $Pd(NO_3)_2$ | 34.6 |

| | | | | |
|---|---|---|---|---|
| *Pd_13* | Tween60+ $C_{12}EO_9$ | IW | $Pd(NO_3)_2$ | 46.2 |
| *Pd_14* | Tween60+ $C_{12}EO_9$ | IE | $PdCl_2$ | 114.6 |
| *Pd_15* | Tween60+ $C_{12}EO_9$ | IW | $PdCl_2$ | 27.3 |
| *Pd_16* | CNR(SBA-15) | IE | $Pd(NO_3)_2$ | 59.5 |
| *Pd_17* | CNR(SBA-15) | IE | $PdCl_2$ | 67.4 |
| *Ni_1* | Tween60 | IE | $Ni(NO_3)_2$ | <1 |
| *Ni_2* | Tween60 | IW | $Ni(NO_3)_2$ | 25.2 |
| *Ni_3* | Tween60 | IE | NiO | 19.7 |
| *Ni_4* | Tween60 | IW | NiO | 16.6 |
| *Ni_5* | Tween60+ $C_{12}EO_9$ | IE | $Ni(NO_3)_2$ | 16.5 |
| *Ni_6* | Tween60+ $C_{12}EO_9$ | IW | $Ni(NO_3)_2$ | 14.4 |
| *Ni_7* | Tween60+ $C_{12}EO_9$ | IE | NiO | 15.4 |
| *Ni_8* | Tween60+ $C_{12}EO_9$ | IW | NiO | 12.2 |
| *Pd/Ni_1* | CNR(SBA-15) | IE | $Pd(NO_3)_2$, $Ni(NO_3)_2$ | 72.6 |
| *Comme_1* | - | - | Pd | 40.6 |

Next, XRD analysis was performed to examine any changes in the crystallinity after metal doping upon the surface of HAP. As an example, samples *Pd_5* and *Ni_6* are presented within *Figure 4.5,* which indicated that the crystallinity of the HAP was preserved and unaffected after both metal treatments in all samples. Subsequently, XRD Rietveld analysis was performed to explore the interaction between Pd and the support. Based on the lattice parameters obtained, it is clear that after Pd doping the morphology of HAP remained stable and the introduction of the metal did not disturb the structure, therefore suggesting that Pd was adsorbed onto the surface of HAP.

It is interesting to note, that this observation differed from that reported in the literature. For example, Boukha *et al.* described Pd loaded HAP for butan-2-ol conversion showing that calcium ions were replaced by Pd *via* cation exchange.[31] Also Indra *et al.* reported substitution of $Ca^{2+}$ with $Pd^{2+}$ on HAP for the Suzuki-Miyaura cross-coupling reaction, however detailed analysis of the structural changes in the HAP were not described.[32]

On the other hand, for Ni based samples there were disturbances in the HAP lattice parameters observed in Rietveld analysis, which suggested that Ni metal created different interactions with HAP, when compared to Pd, also confirmed by SEM described earlier.

However, it is worth noting that the sample with both metals present in the structure of HAP revealed no interruptions within the HAP, therefore Pd preserved its crystal structure, possibly due to a synergistic effect. Nevertheless, the metal particles deposited on the surface of HAP were nanosized, thus there was no visible peaks for Pd and Ni within the XRD pattern, since they appear at the same position as peaks of HAP.

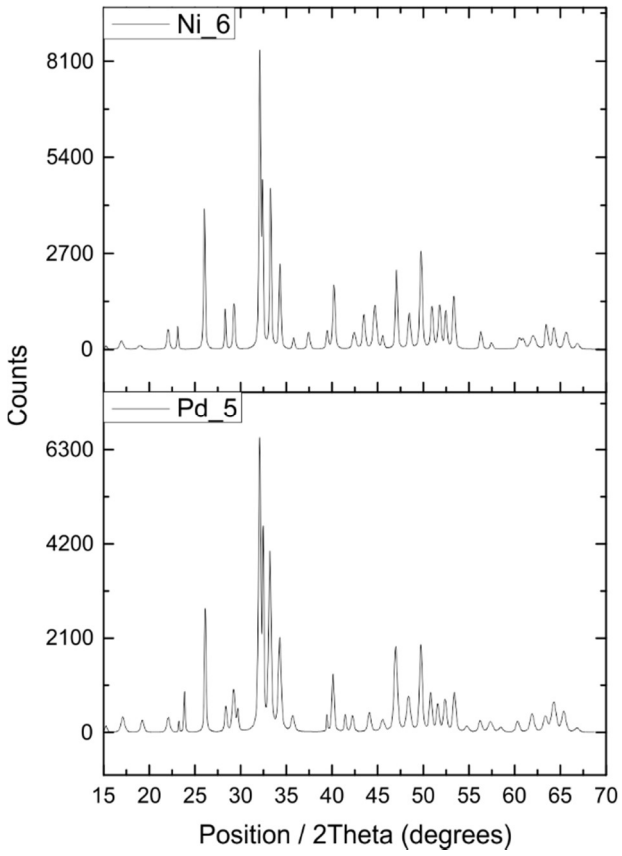


***Figure 4.5****Typical XRD patterns after metal treatments on HAP*

## *4.3.2 Catalytic performance in $CO_2$ reforming*

The set of synthesised catalysts was investigated to determine their activity for methane decomposition under lean conditions using an in-house built catalysis rig, that employed a quartz bed reactor, where all the products of the catalysis reaction were analysed using GC-TCD, as described in details in *section 4.2.2*.

The performance of all the catalysts was assessed in terms of the % of conversion of methane as a function of temperature (*Equation 4.6*). The signals obtained and resolved *via* GC-TCD were $CH_4$ and $CO_2$ as substrates and CO and $H_2$ as products (*Equation 4.1*).

Production of hydrogen is becoming a very valuable tool for the transport industry, because it can be stored, transformed and further utilised in the engine. However in this study hydrogen production was not quantified.

In a typical chromatogram, the retention time of the $CH_4$ signal corresponded to 2.7 min, the $CO_2$ signal appeared at 3.9 min, CO at 2.55 min and in the case when $H_2$ was produced, it appeared as a negative peak at 2.45 $min^{-1}$. As an example, the evolution of the reaction through different temperatures is presented in *Figure 4.6.*

As the reaction proceeded to higher temperatures, the $CH_4$ signal decreased together with $CO_2$, which indicated their conversion starting between 200-250°C as shown in *Figure 4.6*. At the same time, an increase of the CO peak could be observed as CO was produced. All conversion calculations were based on the bypass reading. In this specific example, the hydrogen peak could not be integrated.

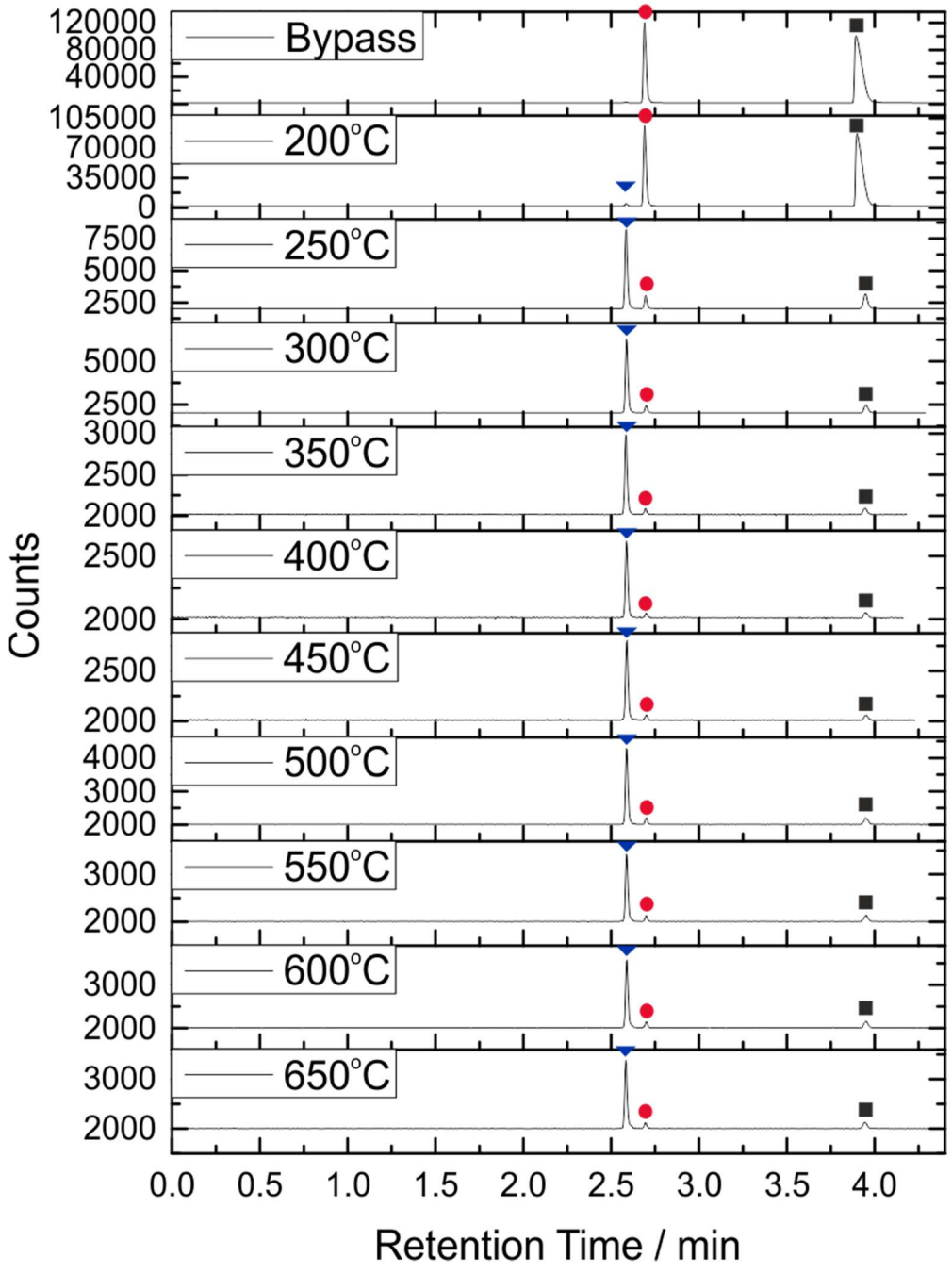


***Figure 4.6*** *Example of chromatograms of the Pd_14 sample at different temperatures,* ●*-$CH_4$,* ■*-$CO_2$,* ▼*-CO*

In order to validate the employed method and GC response, 20 injections were repeated with the same ratio of reactants following the same conditions, and obtained %error corresponded to 0.01%.

Conversions obtained for all catalysts are shown in *Figure 4.7* and grouped based on the HAP utilised. Results were then compared against the commercial catalyst available in the market, Co*mme_1,* which was also tested under the same conditions. It is worth noting that the texture of the commercial sample was not a powder state, but thin corrugated metal sheet coated with a brown paste. This suggested that the sheet of metal used most probably as a substrate is capable of conducting heat from the reactor, thus enhancing its catalytic performance.

First, Pd catalysts based on *HAP_1* and *HAP_2* showed activity no higher than 20% conversion through different temperatures (*Figure 4.7A*). This can be explained by the HAP employed that exhibited poor porosity, hence a limited number of active sites were exposed to the reaction.

As the porosity of the HAP increased, due to utilisation of a single surfactant as a soft-template, the catalytic performance escalated to a maximum of 60% conversion for *HAP_3* and 50% for *HAP_4* based catalysts, as presented in *Figure 4.7B* and *C*. In these cases, even though all the catalysts demonstrated some degree of porosity according to BET surface area measurements, samples *Pd_7* and *Pd_11*, were prepared using the IW approach to load $PdCl_2$ and revealed the lowest catalytic activity. This observation suggested that the IW approach did not provide highly distributed metal particles on the surface of HAP, and will be further investigated in *Chapter 5*.

Furthermore, since $PdCl_2$ was used as a metal precursor, as described in *section 4.1.2*, chloride impurities could negatively influence the catalytic performance by poisoning the sample. Chloride residue was investigated *via* EDX analysis and its presence was confirmed, giving an average of 1.99 wt% for *Pd_7* and 1.60 wt% for *Pd_11*. On the other hand, samples *Pd_4* and *Pd_8* showed the highest conversions in this set of catalysts, and were both synthesised *via* the IE procedure, using $Pd(NO_3)_2$.

Subsequently, samples based on *HAP_5*, which employed both surfactants, were studied and shown in *Figure 4.7D*, revealed the expected higher conversions when compared to the single surfactant approach. The lowest conversion was exhibited by *Pd_15*, synthesised *via* IW and $PdCl_2$, which followed the same trend observed in the

other surfactants, with an average chloride species content of 1.48 wt%, according to EDX. However, catalyst *Pd_14* revealed extremely high catalytic activity, converting 100% of $CH_4$ at a low temperature of 250°C. In addition, this sample exhibited the highest porosity, with a corresponding BET surface area of 114.6 $m^2g^{-1}$, which is more than double the next most porous sample.

As a metal doping protocol, standard IE was utilised for the preparation of catalyst *Pd_14*, which was an additional advantage of this catalyst, since it resulted in excellent metal distribution. Although $PdCl_2$ was employed as a precursor, EDX analysis revealed an absence of chloride species in this sample, hence all chloride species were successfully removed *via* washing and calcination processes. This outstanding catalytic performance greatly exceeded the *Comme_1* sample (*Figure 4.7H*), which at 250°C showed less than 5% conversion and conversion over 50% was only observed above 500°C. In consequence, sample *Pd_14* was studied further to determine its stability.

Following this, high catalytic activity was also observed for the samples based on HAP that was synthesised on CNRs on SBA-15, which showed nearly 100% $CH_4$ conversion over the full range of temperatures tested, as presented in *Figure 4.7E*. A slightly lower conversion profile, yet still significant, was exhibited by the sample with two metals on the surface of the HAP.

After Pd based catalysts, attention was turned to Ni based samples, which were studied using the same procedure. This time, in order to avoid any chloride poisoning effects, $Ni(NO_3)_2$ and NiO were utilised as metal precursors. From samples based on *HAP_3* (*Figure 4.7F*), the highest conversion of 90% was shown by sample *Ni_3*. This was in agreement with the Pd based samples, since *Ni_3* was doped using the more reliable IE approach. However, the lowest conversion was obtained from catalyst *Ni_4* probably due to irregular metal distribution as IW was employed. In the last set of catalysts that consisted of Ni metal prepared on *HAP_5*, *Ni_6* obtained the highest $CH_4$ conversion of 90% and *Ni_8* the lowest out of this set of less than 5% (shown in *Figure 4.7G*).

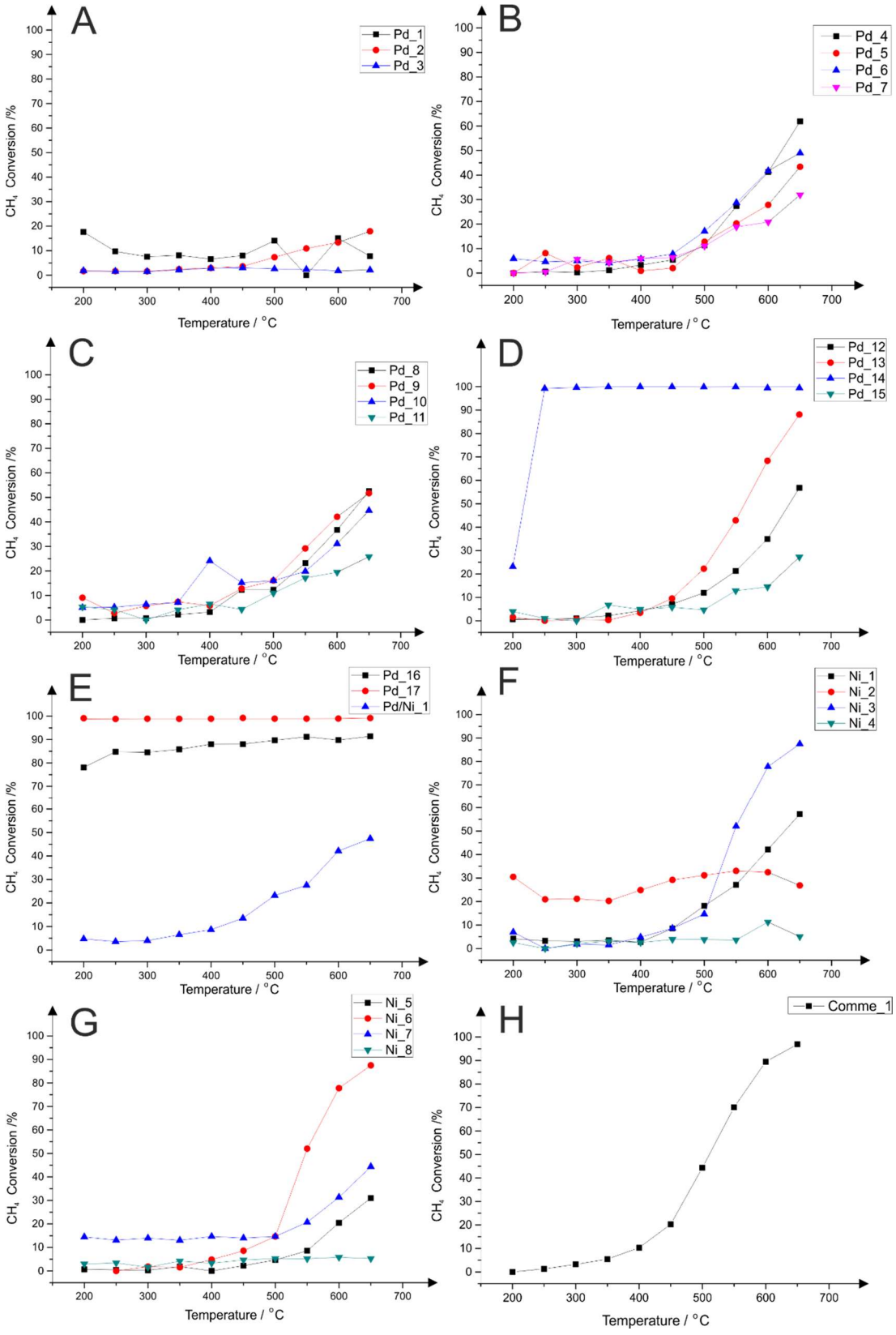


***Figure 4.7*** *Catalytic performance of the synthesised Pd (A-E) and Ni (E-G) based catalysts as a function of $CH_4$ conversion at different temperatures compared to commercially available catalyst (H)*

Subsequently, $CH_4$ and $CO_2$ conversions were plotted at the highest tested temperature of 650°C (*Figure 4.8)*. It is interesting to note, that the $CO_2$ conversions vary from lower, same or higher when compared to $CH_4$ conversion for the same sample.

As described in the literature, in the case when $CO_2$ conversions were greater than $CH_4$, it implies that the production of syngas was influenced by the occurrence of the reverse water-gas shift reaction (*Equation 4.7*).[2] Simultaneous occurrence of this reaction caused a decrease in the $H_2$/CO ratio to values >1, thus the hydrogen signal was barely noticeable. Note that it is not the same reaction as the water-gas shift reaction described in *section 4.1.4,* since there is no carbon produced here and the reaction is exothermic, while during carbon deposition the reaction (*Equation 4.4*) is not just endothermic, but also requires CO rather than $CO_2$ as a reactant.

$$CO_2 + H_2 \leftrightarrow CO + H_2O, \Delta H = 41 kJ mol^{-1} \quad 4.7$$

At the scenario when $CO_2$ and $CH_4$ conversions were equal, as DRM took place in a 1:1 molar ratio of $CO_2$ and $CH_4$, it suggests that the reaction attained high equilibrium conversions to supply high yields of syngas without any other products or side reactions. Thus, from the hydrogen production point of view, catalysts that exhibited this particular $CH_4/CO_2$ conversion ratio can become the most beneficial and powerful. Lastly, at the situation where the reaction consumed $CH_4 > CO_2$, there was a strong argument that the activation of methane most likely did not occur by dissociation, but proceeded through thermal cracking, due to the high temperature of the reaction.[10]

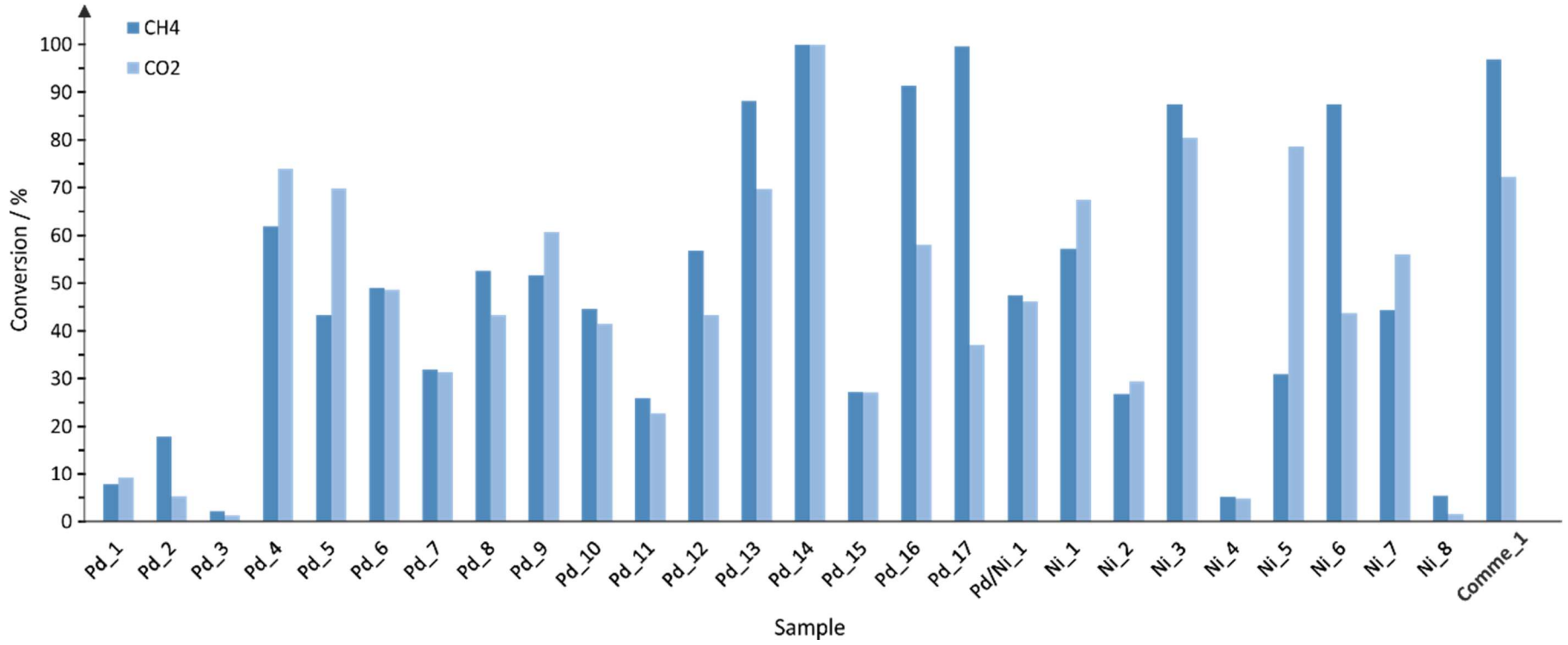


***Figure 4.8*** *$CH_4$ and $CO_2$ conversions of all samples at 650°C*

As described in detail in *section 1.4*, HAP displays basic properties that can reversibly adsorb $CO_2$ species giving rise to at least two types of carbonate apatites, which can be another reason for the observed variations in $CO_2$ conversions, though it is a great challenge to distinguish the observed variations experimentally. Even though the mechanism of this $CO_2$ incorporation in the phosphate is complex and not thoroughly understood, it enhances the chemical reactivity and basic character of HAP.[33]

### *4.3.3 Stability of Pd doped HAP: case of Pd_14*

Since catalyst *Pd_14* was found to be the most active of all prepared samples, the stability of this sample was investigated. For that, the same catalytic test was repeated a further 4 times without any treatments in between runs following the conditions described in *section 4.2.3*.

As presented in *Figure 4.9,* each consequent run gave rise to a higher conversion at a lower temperature. It is clear that, due to the reaction conditions, after the first run, the Pd metal was partially oxidised, thus on the surface of the HAP there was a mixture of reduced metal and metal oxide present, shifting to predominantly PdO after each run.

Moreover, the system was cooled down between runs, during which the reduced Pd favours a shift to the PdO form, suggesting that after consequent runs there was more PdO on the surface, along with reduced Pd, due to re-formation during temperature cycling, as described in the literature.[34] It can therefore be deduced that the exposure of Pd metal to oxygen containing species first led to a chemisorbed monolayer of oxygen forming, followed by slow oxidation, to nearly complete oxidation, to bulk PdO.[35]

This result is supported by the study performed by Datye *et al.,* where activation of $CH_4$ was accompanied by the presence of both phases on the surface of the support.[29]

In general, low metal loading facilitates high chemical potential of the nanosized metal particles that are bound to the support. Since HAP itself is a reducible support

and is capable of providing active surface oxygen during the catalysis processes, the addition of a small amount of Pd highly enhances the oxygen vacancies.[36]

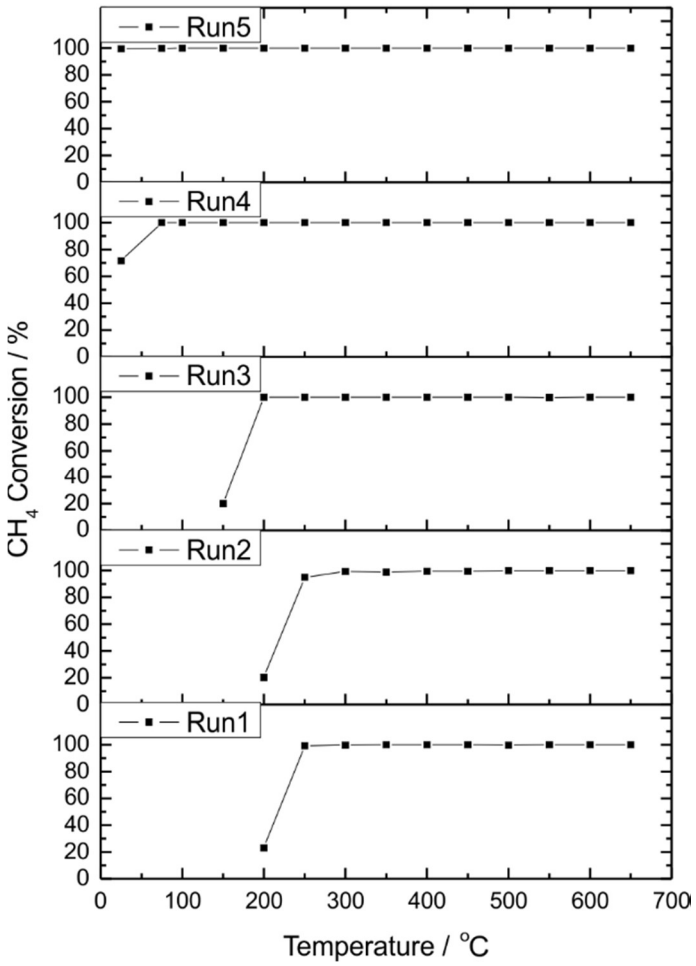


***Figure 4.9*** *$CH_4$ conversion of Pd_14 at different temperatures in 5 consecutive runs*

Following this, the same sample was investigated for any changes in catalytic activity in a continuous flow for 24 hours at 300°C, with the measurements taken hourly. The operating temperature was chosen based on the real situation engine temperatures, where the catalyst is required to be active below 500°C. As shown in the *Figure 4.10*, in the first hours of reaction, the catalyst revealed an oscillating catalytic profile between 65-90% conversion. Observed variations can be explained by a shift reaction from metal oxide and reduced metal *via* a redox cycle that will be discussed in detail in C*hapter 6* in the oxygen rich conditions.

It is interesting to note that after 15 hours of stream reaction, the catalyst reached an equilibrium in the conversion of $CH_4$ with a value of 80%, which is extremely high in view of the low temperature employed, and that such reaction is highly endothermic.

On the other hand, the minimum 20% drop observed the overall activity over time, which outperformed that reported in the literature, suggests that the synthesised catalyst Pd_14 might be resistant to coking process. For example, Souza *et al.* reported that the activity of Pt based catalysts for the DRM reaction exhibited a drop of 30%, however the reaction proceeded at a much higher test temperature (800°C).[37] Also, Takenaka *et al.* reported Pd and Ni based catalysts, which underwent total deactivation in the first 10 hours of the reaction at 600°C.[38] Thus, the catalyst proposed here, *Pd_14,* presented extremely high conversions in the reaction stream, with a low activity loss (20%) over 24 hours continuous performance.

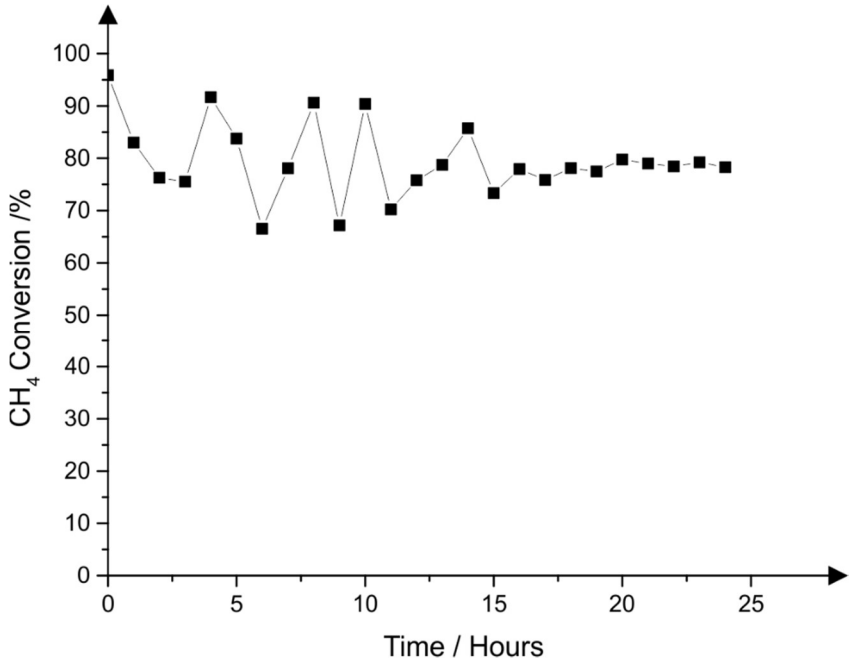


***Figure 4.10*** *Stability of catalytic activity of Pd_14 in the stream of reaction at 300°C*

In order to take the stability testing to another level and reproduce working conditions of the engine as close as possible to real situations, where the catalyst works ON and OFF for certain hours and rests overnight, the performance of *Pd_14* was

studied over 10 days for 8 hours of continuous reaction at 300°C. After which, the system was cooled down and kept closed in a He atmosphere overnight at room temperature. The results were plotted as 'hours on stream' and shown in *Figure 4.11*, and a repeated pattern of the performance was revealed on the catalytic profile obtained over the testing days.

The catalyst exhibited 100% conversion at the start of a working day, after which the activity decreased for 5 consecutive hours and increased again to reach an equilibrium at 80% conversion. The observed fluctuations agree with the previous study carried out over 24 hours, where the catalyst stabilised to 80% of converted $CH_4$ after 10 hours on stream reaction, suggesting a redox cycle between reduced metal and metal oxide, which is further explored in *Chapter 6*.

It is noteworthy that the system was cooled down after the reaction for 8 hours every day, after which 100% $CH_4$ conversion was achieved for the first hour next day. This implied that the catalyst was capable of recovering overnight due to the cooling process. Although it has been shown in the literature that besides metal reduction prior to the reaction, metal oxide decomposes to reduced metal in high temperatures, but what is more important is the fact that it transforms back to oxide upon cooling.[29] Hence, it is fair to say that the more active phase that activated methane in the DRM was metal oxide, or a mixture of two phases: oxide and reduced metal. This phenomenon will be studied in more detail in *Chapter 6*.

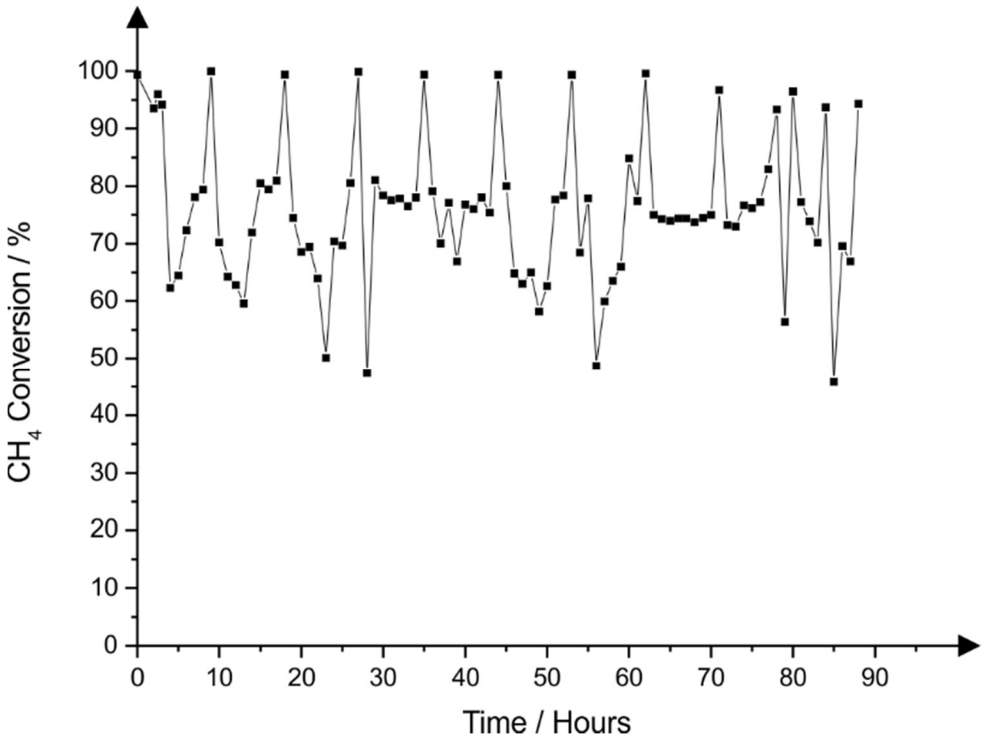


***Figure 4.11*** *Conversion stability of Pd_14 over 10 consecutive days at 300°C with resting overnight at ambient conditions*

### *4.3.4 Carbon deposition*

Attention was next turned to carbon deposition, which is the major cause of de-activation of the catalysts, as described in detail in *section 4.1.4*. After catalytic tests, all samples were analysed *via* TGA. As an example, the results obtained for *Pd_12*, *Pd_14*, *Ni_5* and *Ni_6* are shown in *Figure 4.12* and they were compared to the bare *HAP_5* support.

From the resulting TGA profiles, it was clear that all catalysts were resistant to the coking process, revealing minimum weight loss. Although, as expected, Ni samples showed slightly higher negative slopes and thus they were less resistant to carbon deposition, it still remained insignificant since the maximum weight loss was found to be as low as 5%. It is interesting to note that *HAP_5* exhibited a weight loss of 14%. This was accompanied by dehydroxylation of HAP and was with agreement with what was observed in *Chapter 3*.

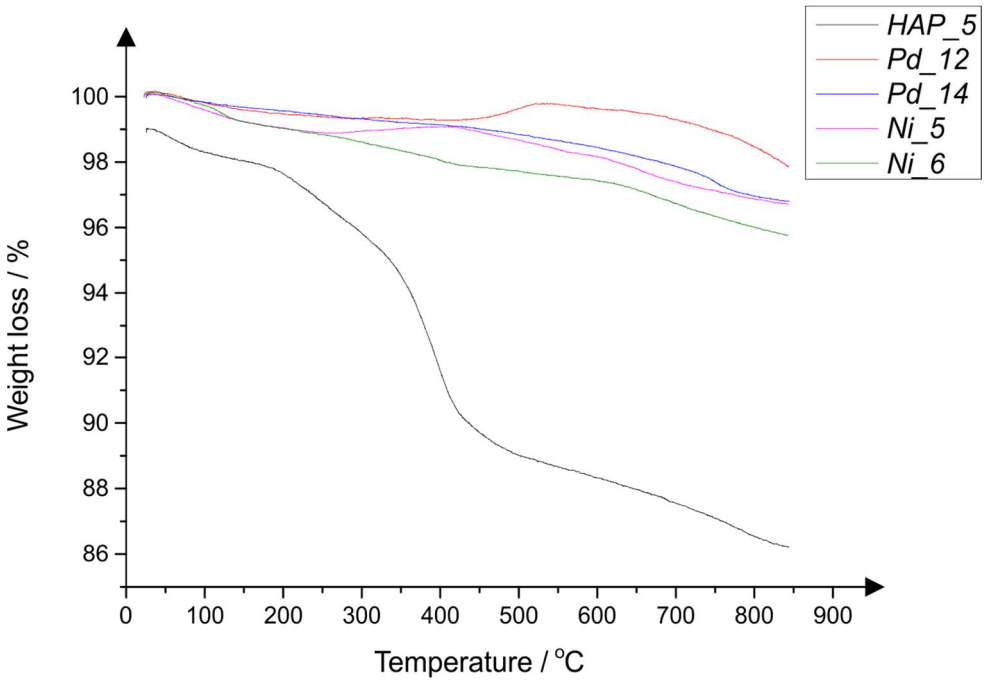


***Figure 4.12*** *TGA profiles of HAP_5 and subsequent 4 samples with metals after DRM reaction*

## 4.4 Conclusions

This chapter has reported on the successful Pd, Ni and Pd/Ni doping on the surface of HAP with the average total metal loading of 3 wt%, determined by EDX of each metal. All resulting catalysts were fully characterised and crystallinity was compared to bare HAP. It was found that Pd metal enhanced the porosity of the catalyst, while Ni metal reduced it, suggesting a different type of interaction between the metals and the support. XRD Retvield analysis revealed that Pd was adsorbed onto the surface of HAP and did not interfere with its crystal lattice, but Ni metal introduced disturbances within the HAP structure, confirming a different type of interaction with HAP when compared to Pd.

Also, all catalysts were investigated for dry reforming of methane using an *in-house* setup that involved a fixed bed reactor coupled to a GC-TCD to reproduce oxygen lean conditions. Based upon the results, it was clear that the precursor of the metal employed and metal loading approach used played a significant role in the resulting activity of the catalyst.

It was also observed that chloride residue from the metal salt can poison the catalyst, which was in agreement with reports in the literature. However excessive washing and calcination treatments successfully removed all chloride ions left from the metal doping process.

Among the numerous catalysts prepared and tested throughout this work, Pd based ones were found to be the most active and specifically the catalyst that utilised $PdCl_2$ loaded *via* IW, which in addition was the most porous out of all set prepared. This sample revealed an extremely high $CH_4$ conversion (100%) at low temperature (250°C), which impressively exceeded the commercially available catalyst (*Comme_1*) tested under the same conditions. The stability of this sample was further studied and revealed that the catalyst was generally stable and converted 80% $CH_4$ after 88 hours of stream reaction at low temperature, similar to real operating conditions (300°C).

A very interesting results obtained from this work also suggested that the more active form of metal in the DRM reaction was metal oxide or a mixture of metal oxide and reduced metal, which was obtained by cooling down and heating up the closed system. Finally, TGA results demonstrated that all synthesised catalysts were resistant to carbon deposition, showing a minimum weight loss of 5%.

## 4.5 References

1. D. Pakhare and J. Spivey, *Chemical Society Reviews*, 2014, **43**, 7813-7837.
2. R. Horn and R. Schlögl, *Catalysis Letters*, 2015, **145**, 23-39.
3. S. Arora and R. Prasad, *RSC Advances*, 2016, **6**, 108668-108688.
4. W.-C. Chung and M.-B. Chang, *Renewable and Sustainable Energy Reviews*, 2016, **62**, 13-31.
5. M. Usman, W. M. A. Wan Daud and H. F. Abbas, *Renewable and Sustainable Energy Reviews*, 2015, **45**, 710-744.
6. H. Y. Wang and E. Ruckenstein, *The Journal of Physical Chemistry B*, 1999, **103**, 11327-11331.
7. A. M. O'Connor, Y. Schuurman, J. R. H. Ross and C. Mirodatos, *Catalysis Today*, 2006, **115**, 191-198.
8. J. Wei and E. Iglesia, *Journal of Catalysis*, 2004, **225**, 116-127.
9. A. Erdohelyi, J. Cserenyi and F. Solymosi, *Journal of Catalysis*, 1993, **141**, 287-299.

10. Y. Schuurman, V. C. H. Kroll, P. Ferreira-Aparicio and C. Mirodatos, *Catalysis Today*, 1997, **38**, 129-135.
11. J. Chen, Q. Wu, J. Zhang and J. Zhang, *Fuel*, 2008, **87**, 2901-2907.
12. N. Rahemi, M. Haghighi, A. A. Babaluo, M. F. Jafari and P. Estifaee, *Journal of Industrial and Engineering Chemistry*, 2013, **19**, 1566-1576.
13. E. Kowalewski, I. I. Kamińska, G. Słowik, D. Lisovytskiy and A. Śrębowata, *Reaction Kinetics, Mechanisms and Catalysis*, 2017, DOI: 10.1007/s11144-017-1148-4, 1-14.
14. P. Kim, H. Kim, J. B. Joo, W. Kim, I. K. Song and J. Yi, *Journal of Molecular Catalysis A: Chemical*, 2006, **256**, 178-183.
15. C. F. Cullis and B. M. Willatt, *Journal of Catalysis*, 1984, **86**, 187-200.
16. P. Gélin and M. Primet, *Applied Catalysis B: Environmental*, 2002, **39**, 1-37.
17. E. Marceau, H. Lauron-Pernot and M. Che, *Journal of Catalysis*, 2001, **197**, 394-405.
18. D. O. Simone, T. Kennelly, n. l. brungard and R. J. Farrauto, *Applied Catalysis*, 1991, **70**, 87-100.
19. I.V. Yentekakis, R.M. Lambert, M. Konsolakis and N. Kallithrakas-Kontos, *Catalysis Letters*, 2002, **81**, 181-185.
20. J. H. Bitter, K. Seshan and J. A. Lercher, *Topics in Catalysis*, 2000, **10**, 295-305.
21. S. Sugiyama, Y. Iguchi, H. Nishioka, T. Minami, T. Moriga, H. Hayashi and J. B. Moffat, *Journal of Catalysis*, 1998, **176**, 25-34.
22. B. Faroldi, M. L. Bosko, J. Múnera, E. Lombardo and L. Cornaglia, *Catalysis Today*, 2013, **213**, 135-144.
23. M. S. Dresselhaus and I. L. Thomas, *Nature*, 2001, **414**, 332-337.
24. R. M. Dell and D. A. J. Rand, *Journal of Power Sources*, 2001, **100**, 2-17.
25. J. Kamieniak, E. P. Randviir and C. E. Banks, *TrAC Trends in Analytical Chemistry*, 2015, **73**, 146-157.
26. S. Wang, G. Q. Lu and G. J. Millar, *Energy & Fuels*, 1996, **10**, 896-904.
27. P. Chen, Z. Hou, X. Zheng and T. Yashima, *Reaction Kinetics and Catalysis Letters*, 2005, **86**, 51-58.
28. Z. Opre, J. D. Grunwaldt, M. Maciejewski, D. Ferri, T. Mallat and A. Baiker, *Journal of Catalysis*, 2005, **230**, 406-419.
29. A. K. Datye, J. Bravo, T. R. Nelson, P. Atanasova, M. Lyubovsky and L. Pfefferle, *Applied Catalysis A: General*, 2000, **198**, 179-196.
30. A. E. Allen and D. W. C. MacMillan, *Chemical Science*, 2012, **3**, 633-658.
31. Z. Boukha, M. Kacimi, M. Ziyad, A. Ensuque and F. Bozon-Verduraz, *Journal of Molecular Catalysis A: Chemical*, 2007, **270**, 205-213.
32. A. Indra, C. S. Gopinath, S. Bhaduri and G. Kumar Lahiri, *Catalysis Science & Technology*, 2013, **3**, 1625-1633.
33. Z. Boukha, M. Kacimi, M. F. R. Pereira, J. L. Faria, J. L. Figueiredo and M. Ziyad, *Applied Catalysis A: General*, 2007, **317**, 299-309.
34. S. Sugiyama, T. Minami, T. Moriga, H. Hayashi and J. B. Moffat, *Journal of Solid State Chemistry*, 1998, **135**, 86-95.
35. R. Burch, *Catalysis Today*, 1997, **35**, 27-36.
36. R. K. Singha, A. Yadav, A. Shukla, M. Kumar and R. Bal, *Catalysis Communications*, 2017, **92**, 19-22.

37. M. M. V. M. Souza and M. Schmal, *Applied Catalysis A: General*, 2003, **255**, 83-92.
38. S. Takenaka, Y. Shigeta, E. Tanabe and K. Otsuka, *Journal of Catalysis*, 2003, **220**, 468-477.

# Chapter 5: Exploring of New Methods for the Preparation of Pd/HAP Catalysts: Influence of pH and Ultrasound on Conventional Loading Methods

# 5.1 Introduction

In this chapter, the influence of ultrasound and different pH pretreatments during the Pd doping of the HAP support was investigated. Ultrasound-assisted ion exchange (IE) and incipient wetness impregnation (IW) methodologies were employed as a proof-of-concept to decorate the surface of HAP with Pd metal and are compared to conventional procedures previously utilised in *Chapter 4*. The influence of pH upon the distribution of Pd throughout the samples during the doping process was also studied. Then, all the prepared samples were evaluated for their catalytic activity towards dry reforming of methane (DRM), using the same procedure as described in *Chapter 4*. Note, that for this study, HAP synthesised on carbon nanorods was employed, which were prepared using MCM-48 as a template, as described in *Chapter 2*. Results within this chapter have been published in Catalysis Letters, 2017, 147 (8), 2200-2208.

## *5.1.1 Ion exchange protocol*

There are two metal doping methodologies mainly employed by scientists, ion exchange (IE) and incipient wetness impregnation (IW).[1-6] In general, the IE protocol has been described as more reproducible and reliable, while IW, even though it is a very simple approach, provides non-uniform metal distribution, size and shape.[7]

Ion exchange was discovered in the 19$^{th}$ century and since then it has become a valuable process in nearly all chemistry sectors.[8] The simplest ion exchange procedure involves a mixture of known concentration of electrolyte and known amount of negligible soluble material, as shown in *Figure 5.1*. The process takes place while stirring the mixture using a conventional magnetic stirrer. The solid is then saturated, and thus undergoes a quite rapid exchange process. However, it is best to continue the experiment for some time in order to reach equilibrium, which in some cases can even take weeks. Nevertheless, the analysis of equilibrium in the solution remains challenging.

Scientists extensively investigated the behaviour of electrolytes in aqueous solution in the late 1880s, and their studies revealed that many electrolytes fully dissociate in order to form solvated ions in the solution. In view of that, according to the Arrhenius theory of electrolyte dissociation, molecules of an electrolyte constantly alternate from splitting up into ions, to reuniting to form undissociated molecules. Hence, there is a dynamic equilibrium between ions and undissociated molecules. However, this theory is not accurate in the case of strong electrolytes, since they have been described as practically fully ionised.[9]

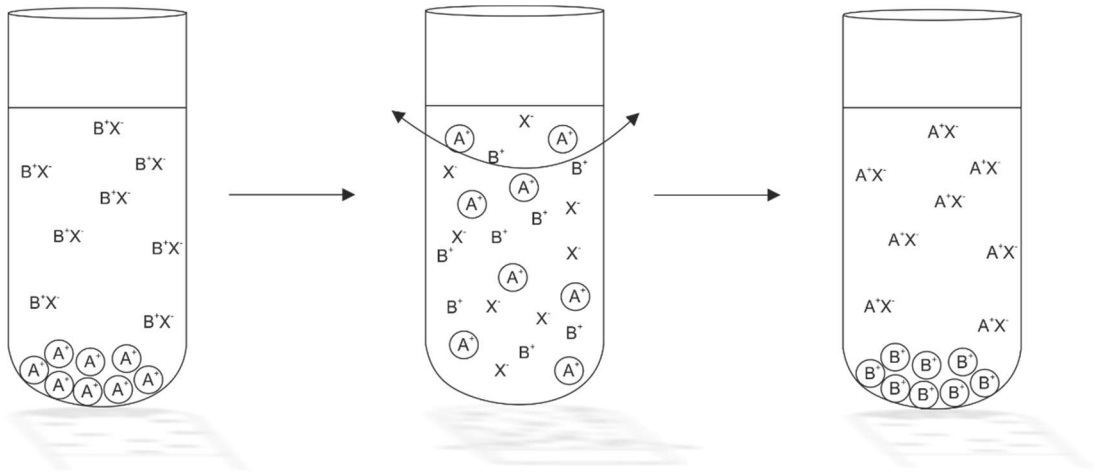

***Figure 5.1*** *Schematic representation of ion exchange process in the solution*

The very important parameter that can affect the ion exchange process is ion selectivity, and it is calculated from differences in Coulomb interactions between ions of the exchange material and the exchanger, which is controlled by ion hydration. The capability of the ions to be hydrated limits how close they can approach surface-charged sites, at the same time determining their binding energy. In other words, ions surrounded by fewer water molecules are capable of approaching exchange sites more closely. Thus they are selectively adsorbed, when compared to hydrated ions, where the higher radius keeps them a further distance from exchange sites.[8]

In the case of applying the aforementioned general IE principle in doping HAP with a metal, the metal salt plays the role of an electrolyte ($B^+X^-$ in *Figure 5.1*) and is dissolved or suspended in the water, where HAP is a non-soluble powder with $A^+$ being the corresponding calcium ions.

### *5.1.2 Incipient wetness impregnation methodology*

Impregnation occurs through contact of a solid with a liquid that contains the species to be deposited on the surface. During such deposition various processes can be recognised, such as selective adsorption by Coulomb forces; van der Waals of H-bond; partial dissolution of the surface of the solid; or polymerisation of the species attached to the surface.[10] However, there are factors like the nature of the surface or its reactivity that can influence the impregnation. It is important to note, that the equilibrium between liquid and solid is slow and highly challenging to establish, leading to non-uniform distribution of the attached species on the surface.

There are eight different impregnation methods described in the literature based on the aforementioned principles. One of them widely used in catalysis chemistry is incipient wetness impregnation.[11] It is a simple protocol where species to be attached are dissolved in a minimum amount of *e.g.* water and drop by drop applied onto the surface of the solid to the point beyond which the mixture begins to look wet, followed by drying *via* heating, as shown in *Figure 5.2*. The simplicity and 100% yield of the attached species make it an interesting approach, however distribution is rather random and difficult to reproduce.

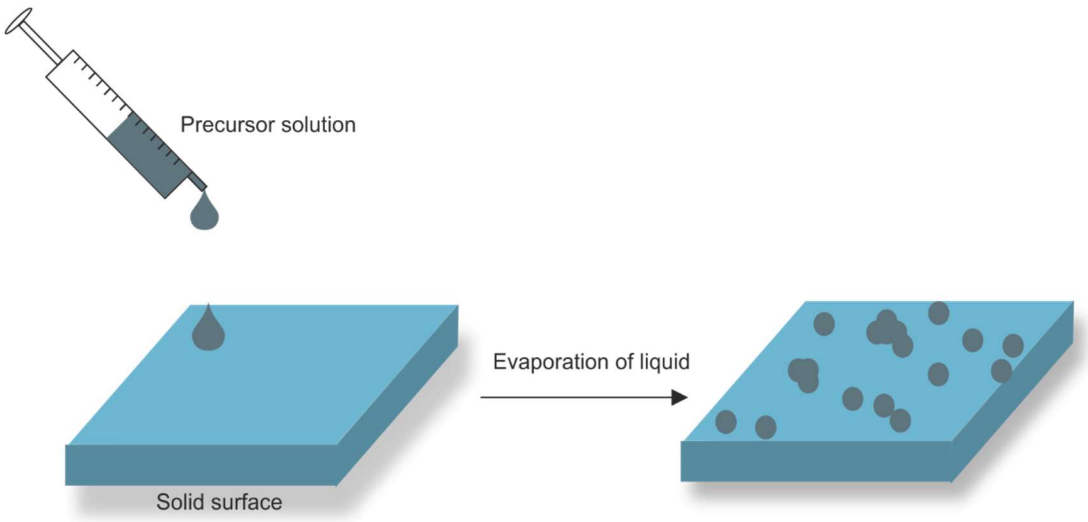


***Figure 5.2*** *Schematic representation of incipient wetness impregnation method*

Nevertheless, there are limited reports that investigate the optimisation of those methods or how the metal distribution is affected by different parameters *e.g.* pH. For example, Rego De Vasconcelos *et al.* produced syngas by DRM over Ru and Pt supported HAP using different doping methods. However only the Pt catalyst doped using the IW protocol was found to be stable.[12]

In view of that, there is a necessity in the field for reliable, simple methods that will successfully decorate the support with evenly distributed metal particles. Based on that, employing an ultrasonic treatment that is cost-effective and a widely available method, and relatively unstudied as an assistance for conventional methods during doping processes, may improve the metal distribution and form smaller metal particles, which can lead to enhanced catalytic activity.

On the other hand, based on the fact that pH plays an important role in the adsorption of heavy metals on HAP when applying the standard IE procedure (as widely reported in the literature for environmental applications of this material), the investigation of the influence of pH of the solutions involved in the IE and IW of Pd on HAP for further catalytic studies was also performed. Comparison with materials prepared using the same procedures in water solution towards DRM reaction was also carried out.[13, 14]

## 5.2 Experimental

### *5.2.1 Pd doped HAP by the ion exchange (IE) process*

A typical ion exchange methodology was employed as a reference following the same procedure as described in C*hapter 3*. First, $Pd(NO_3)_2$ (50 mg) was dissolved in deionised water (100 mL). After that, HAP was added (1 g) and stirred for three days at room temperature, then filtered and dried in an oven at 60°C for 3 hours.

To accelerate the IE process, instead of stirring in ambient conditions for 3 days, the solution was treated with ultrasound (UltraWave U95, 50-60 Hz) for 3 hours *via* the use of an ultrasonic bath.

The resulting samples were filtered, dried in an oven at 60°C for 3 hours and calcined in air at 550°C. Three replicates were diligently performed.

To investigate the influence of pH of the media in which IE takes place, a Britton-Robinson buffer was utilised, instead of water, at different pH (2, 4, 6, 8, 10 and 12). All samples were filtered, dried in the oven at 60°C for 3 hours and calcined in air at 550°C.

### *5.2.2 Pd doped by incipient wetness impregnation (IW) process*

As a reference sample, $Pd(NO_3)_2$ (50 mg) was dissolved in a minimal amount of deionised water and dripped onto HAP (1 g), which was carefully mixed. The obtained yellow-brown powder was dried in the oven at 60°C for 3 hours and calcined in air at 550°C.

For the ultrasound-assisted impregnation, six samples of HAP, mixed with Pd in the same proportions as described above, were placed in volumetric flasks and sonicated from 10 min to 1 hour, taking one sample out every 10 minutes. All samples were dried in the oven at 60°C for 3 hours and calcined in air at 550°C.

To examine the influence of pH upon the doping method, HAP was first pretreated in different pH by stirring HAP (1 g) in a Britton-Robinson buffer for 3 hours following the same procedure as for IE (pH 2, 4, 6, 8, 10 and 12), it was then filtered and dried. Metal was then dripped onto pretreated HAP using the standard IW procedure, then dried in the oven at 60°C for 3 hours and calcined in air at 550°C.

### *5.2.3 Catalysis tests*

The catalytic activity of each sample was studied through the DRM reaction, following the same procedure as described in *Chapter 3, section 3.2.2.* Conversions of $CH_4$ and $CO_2$ are presented at the highest measured temperature (650°C).

## 5.3 Results and Discussion

### *5.3.1 Ion exchange (IE)*

The first step was to apply Pd onto the surface of the HAP using a standard ion exchange approach (IE) loading methodology as a control sample. As described in *section 5.1.1*, this approach involves stirring the support and metal salt in the solution at ambient conditions over the course of a few days. Hence, as this method is time consuming (usually 3 days), ultrasound was employed as an alternative to accelerate the process (3 hours). Three samples were prepared and characterised, along with a control sample (standard IE), using EDX analysis to examine the Pd loading and its distribution across the surface of HAP. The metal loading was recorded from 5 different areas (*N*=5) on each sample.

As shown in *Table 5.1*, the average Pd content is slightly higher following the application of ultrasound, in comparison to the control sample (no ultrasound), with higher standard deviation (SD). This implies that ultrasound can accelerate the IE process, giving a high dispersion of metal upon the surface of HAP; hence it can be employed in the future as an alternative to the standard IE procedure with significant time-consuming benefits.

***Table 5.1*** *The average metal loading for IE and ultrasound-assisted IE approaches and standard deviation (SD) via EDX (N=5) and ICP-OES*

| | ***Average metal loading /wt%*** | ***SD*** | ***ICP-OES /wt%*** |
|---|---|---|---|
| **Control IE sample** | 2.044 | 0.07 | 2.07 |
| ***Ultrasound-assisted*** | | | |
| ***S1*** | 2.53 | 0.28 | 2.06 |
| ***S2*** | 2.18 | 0.51 | 1.90 |
| ***S3*** | 2.81 | 0.44 | 1.81 |

The catalytic activity of the ultrasound-assisted IE samples towards the DRM reaction was explored using the same in-house built experimental setup as described in *section 4.2.2*.

Based on previously described reports, as the Pd metal was fully distributed throughout the porous support, catalytic conversions would be expected to increase, due to more metal exposure to facilitate the reaction. As presented in *Figure 5.3*, the control sample actually exhibited higher conversions (91% for $CH_4$ and $CO_2$), in comparison to ultrasound-assisted samples.

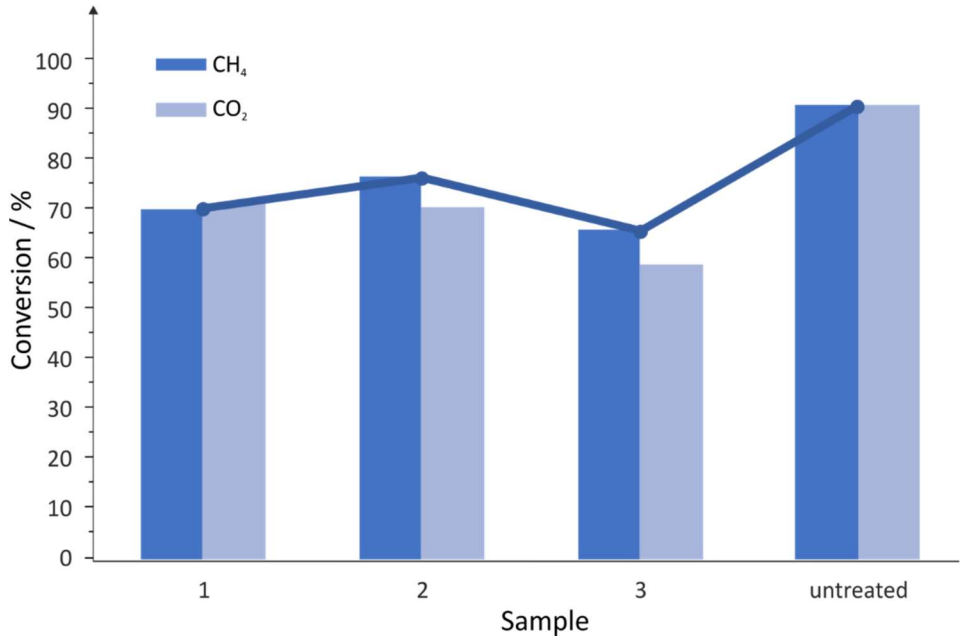


***Figure 5.3*** *DRM of ultrasound-assisted IE doped catalysts*

Even though the concentration of Pd on the surface remained approximately the same and suggested an improved distribution, it was noted that during ultrasonic treatment, water in the ultrasonic bath became warmer and slightly increased the temperature of the solutions. In consequence, $Pd(NO_3)_2$ became more soluble and smaller particles were produced; therefore they were more likely to create agglomerates during the IE process, resulting in a decreased catalytic activity (~70% conversion for $CH_4$ and $CO_2$).

However, despite this reduction in activity, ultrasound significantly accelerated the IE process from 3 days to 3 hours, hence with careful optimisation of time and temperature, ultrasound-assisted IE can become a beneficial tool for future use/applications.

Next, different pH media were investigated in the IE standard methodology, replacing water with a Britton-Robinson buffer and examining its influence on the metal distribution and subsequently catalytic activity towards DRM. Based on the EDX data (shown in *Table 5.2*), the average metal loading remained practically stable throughout the pH range studied. In fact, the lowest SD of the distribution was observed when IE took place in neutral pH in the control sample (SD = 0.07).

**Table 5.2** *The average metal loading for IE performed in different pH and standard deviation (SD) via EDX (N=5) and ICP-OES*

| | ***Average metal loading /wt%*** | ***SD*** | ***ICP-OES / wt%*** |
|---|---|---|---|
| **Control IE sample** | 2.044 | 0.07 | 2.07 |
| ***pH:*** | | | |
| ***2*** | 2.12 | 0.20 | 1.95 |
| ***4*** | 1.93 | 0.10 | - |
| ***6*** | 2.01 | 0.15 | 1.72 |
| ***8*** | 2.12 | 0.48 | 1.93 |
| ***10*** | 2.03 | 0.32 | 2.06 |
| ***12*** | 2.23 | 0.29 | - |

(-) represents insufficient sample for the analysis

As is also shown in *Figure 5.4*, neutral water media during metal loading was more beneficial in the catalytic reaction of methane, exhibiting over 90% $CH_4$ and $CO_2$ conversions. On the other hand, the lowest conversion (24%) was observed in the strongest acidic media. This can be explained by the higher solubility of the metal and HAP support in the acid, producing smaller particles that favour interactions between both materials.

Even though metal loading remained unaffected and Pd was well distributed (*Table 5.2*), which was expected to be advantageous in the catalytic performance, formation of clusters due to agglomeration of the particles significantly reduced the activity of the catalyst.

As pH was increased, an improvement in catalytic activity was clearly observed. It is noteworthy that the most active catalyst was obtained after a buffer treatment at pH 10 (over 80% $CH_4$ conversion), which was the same pH that was employed during the synthesis of HAP.

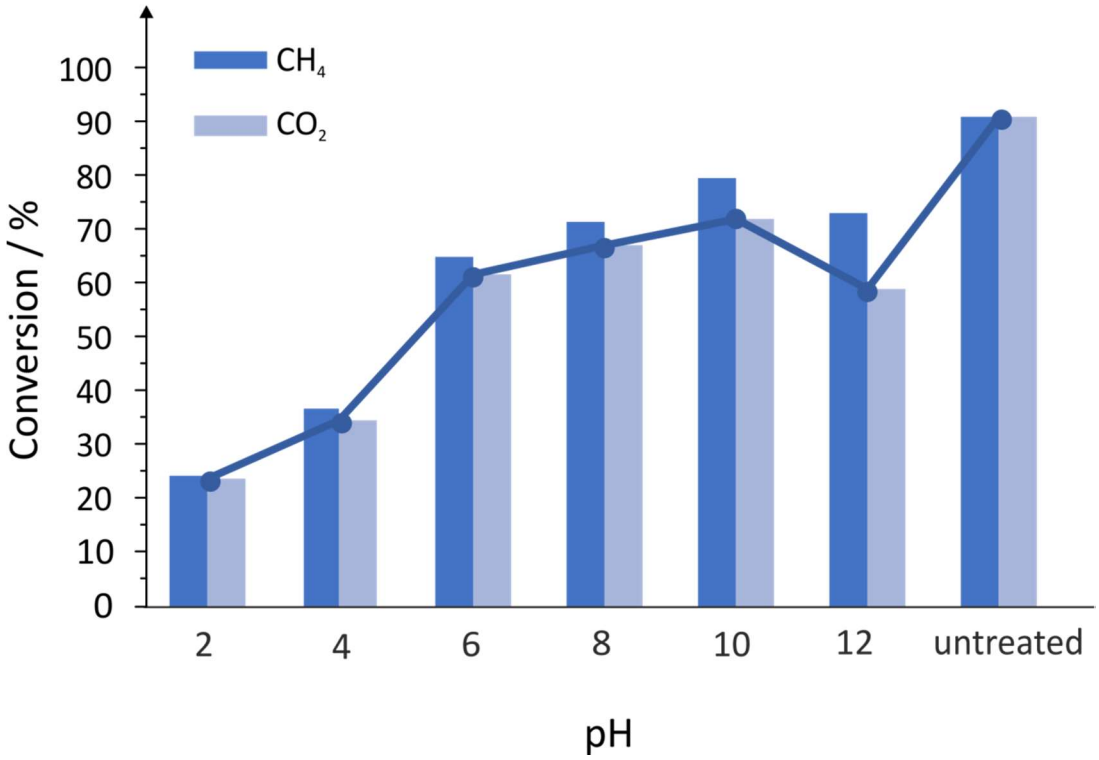


***Figure 5.4*** *DRM of IE doped catalysts fabricated using different pH media*

It is interesting to note, that some samples exhibited different conversions of $CO_2$ to that of $CH_4$ and this behaviour was already observed and described in C*hapter 3*. For the untreated sample, the % conversion of $CH_4$ was found to be equal to the % conversion of $CO_2$. This was due to the 1:1 molar ratio of both reactants in the DRM reaction, which suggested that the reaction attained high equilibrium conversions and was selective towards a high yielded syngas without any other products or side reactions.

On the other hand, in the case of all samples prepared either at different pH or ultrasound treatments, $CO_2$ conversions were lower than those of $CH_4$. There is a strong argument that the methane did not fully undergo activation through its dissociation, but also proceeded through thermal cracking due to the high temperature of the reaction.[15]

### *5.3.2 Incipient wetness impregnation (IW)*

Another metal loading methodology studied in this chapter was incipient wetness impregnation (IW). A typical IW approach employs the addition of metal dissolved in a minimum amount of water onto the solid support, followed by evaporation of excess water. In general, IE is a more reproducible method and results in more homogenous metal loading, due to stable doping conditions where all the support is exposed to the metal in the solution, unlike in the IW procedure, which provides random metal deposition (*Figure 5.5*).

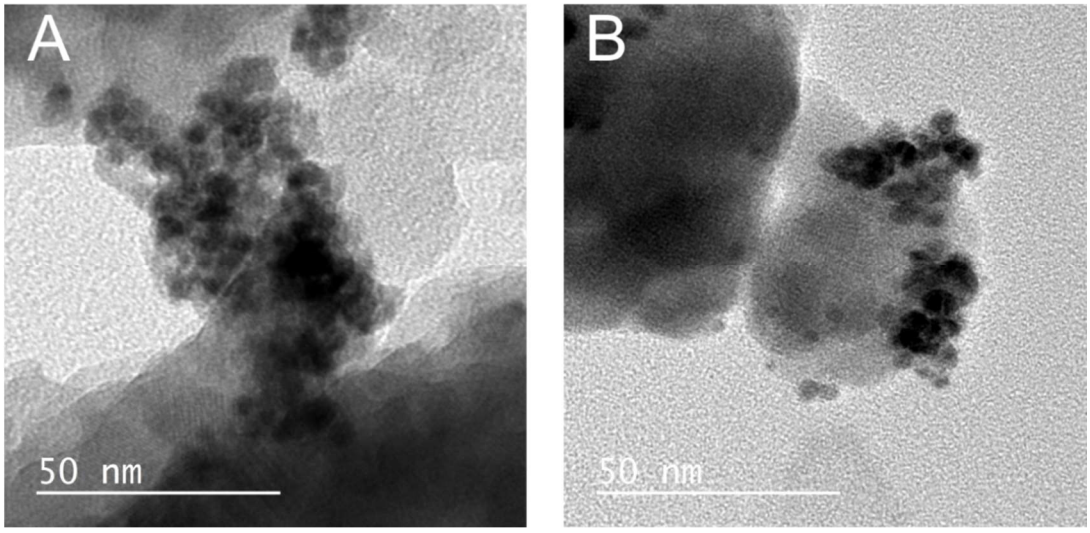


***Figure 5.5*** *Typical TEM images of standard Pd doped HAP via IE (A) and IW (B)*

In order to have more control over the dispersion of metal throughout the support in the IW approach, ultrasound was utilised over the time range from 10 to 60 min. EDX results from six samples of Pd doped HAP using the ultrasound-assisted IW method and a control sample prepared *via* a standard IW protocol, are shown in *Table 5.3*. Five different areas of each sample were analysed to obtain the average metal loading on the HAP.

***Table 5.3*** *The average metal loading for IW and ultrasound-assisted IW approaches and associated standard deviation (SD) via EDX (N=5) and ICP-OES*

| | ***Average metal loading /wt%*** | ***SD*** | ***ICP-OES / wt%*** |
|---|---|---|---|
| **Control IW sample** | 11.12 | 4.40 | 3.32 |
| ***Ultrasound-assisted (min)*** | | | |
| ***10*** | 7.39 | 3.52 | 4.13 |
| ***20*** | 6.45 | 3.55 | 4.33 |
| ***30*** | 6.29 | 2.61 | 2.72 |
| ***40*** | 5.82 | 2.62 | 3.18 |
| ***50*** | 5.10 | 2.66 | 2.96 |
| ***60*** | 4.17 | 2.52 | 4.14 |

It was observed in *Table 5.2* that longer sonication times were accompanied by decreased average metal (wt%) throughout the surface of the material and reduced SD values, respectively. However, ICP-OES analysis revealed that the total concentration of Pd remained constant in all samples, *i.e.* the samples prepared after 10 and 60 min of ultrasound contained 4.13 wt% and 4.14 wt% of Pd, respectively, which are almost identical. The corresponding EDX readings, however, decreased significantly for the same samples from 7.39 wt% to 4.17 wt%. Consequently, it appeared that during the sonication process the clusters formed were progressively broken down into smaller particles that were not detected by EDX (detection limits for this technique are typically particles >1-2µm), which accounted for the apparently lower metal loadings.

On the other hand, the results obtained from ultrasound-assisted IW, when compared to the standard protocol, suggested that the high Pd loading achieved in the control sample was due to poor metal distribution and the formation of agglomerates and, therefore the EDX surface analysis may be somewhat misrepresentative due to it being a semi-quantitative technique.

Note that, all samples loaded using the IW technique exhibited higher average metal content, when compared to those obtained after IE (*Table 5.1*), which was also validated by ICP-OES (average Pd concentration of 3.57±0.6 and 1.92±0.1 wt% for ultrasound-assisted IW and ultrasound-assisted IE, respectively).

This agrees with the general principle of the IW methodology described above, where irregularly distributed agglomerated metal particles are formed on the surface of HAP. In consequence, EDX surface analysis for the IE methodology was more reliable when compared to IW, where the average metal loading was overestimated, due to the presence of metal clusters on HAP.

Those observations were supported by the catalytic activity of the materials, as shown in *Figure 5.6*. As sonication time increased, higher catalytic activity was observed, with $CH_4$ and $CO_2$ conversions of 66% after 60 min of ultrasound exceeding the control sample by nearly 15%. Catalysis results were consistent with ICP-OES and EDX observations showing significant improvements in both metal distribution and catalytic responses, making ultrasound-assisted IW a valuable alternative to the standard method. Nevertheless, $CH_4$ and $CO_2$ conversions obtained by IW loaded samples were significantly lower when compared to IE, especially when considering the relative metal loading levels. Moreover, based upon the $CH_4$:$CO_2$ conversions, all samples revealed 1:1 molar ratio of the reactants indicating high equilibrium and selectivity towards the high purity syngas produced, making the reaction very attractive from the industrial point of view.

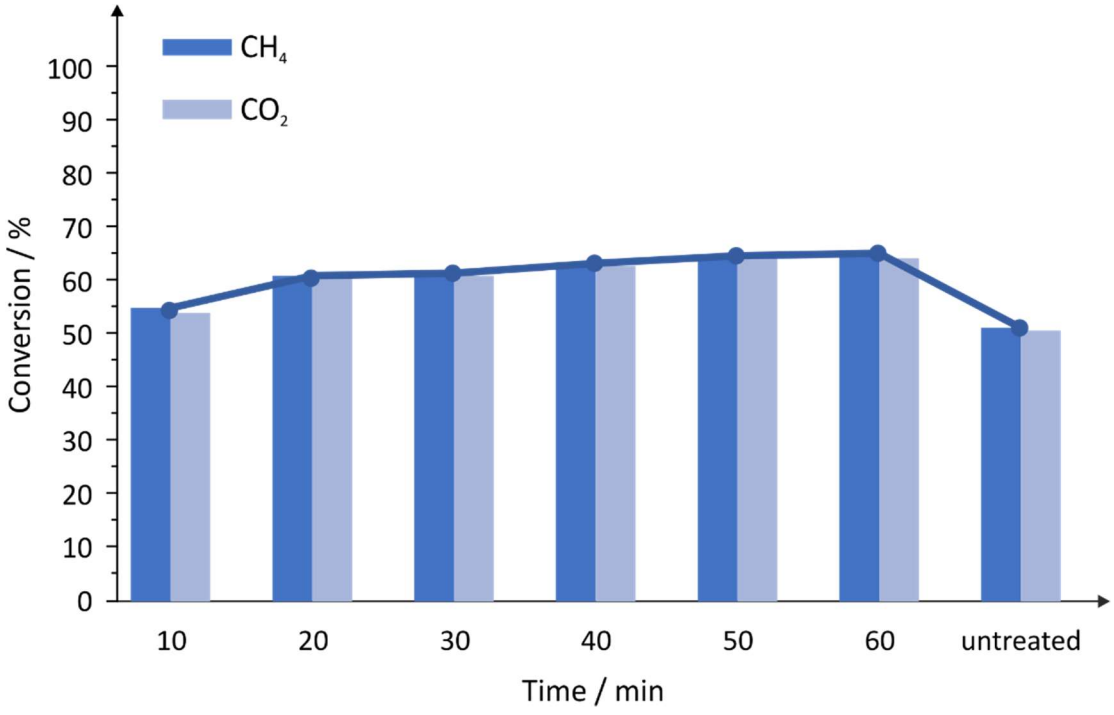


***Figure 5.6*** *DRM of ultrasound-assisted IW doped catalysts*

Finally, HAP was pretreated before being doped with Pd using a Britton-Robinson buffer and different pH (2, 4, 6, 8, 10 and 12). As presented in *Table 5.4*, lower SD values from the EDX analysis implied a better distribution of Pd particles formed upon HAP at all pH values when compared to the control sample. However, no apparent trend was found at different values of pH. It was found that, at pH 2, 6 and 12, higher average metal loadings were achieved, but they were accompanied with higher SD values, indicating non-homogenous deposition of metal on the surface of the HAP. On the other hand, it is interesting to note that metal loading percentages at pH 4, 8 and 10 were lower with improved SD values that were similar to those obtained for the IE technique.

***Table 5.4*** *The average metal loading for IW performed in different pH associated standard deviation (SD) via EDX (N=5) and ICP-OES*

| | ***Average metal loading /wt%*** | ***SD*** | ***ICP-OES / wt%*** |
|---|---|---|---|
| **Control IW sample** | 11.12 | 4.40 | 3.32 |
| ***pH:*** | | | |
| ***2*** | 3.44 | 2.24 | - |
| ***4*** | 2.42 | 0.54 | 1.84 |
| ***6*** | 4.66 | 2.78 | 1.99 |
| ***8*** | 2.41 | 1.04 | 1.95 |
| ***10*** | 2.05 | 1.16 | 1.54 |
| ***12*** | 5.93 | 3.09 | 1.01 |

(-) represents insufficient sample for the analysis

Regarding the DRM reaction over pretreated materials, in *Figure 5.7* it is clearly demonstrated that pH treatments were beneficial in terms of catalytic performance when compared to the control sample. $CH_4$ and $CO_2$ conversions ranged from 57% in the acidic pH to the highest value of 97% at pH 10, which significantly exceeded the activity of the untreated sample. The higher catalytic activities of buffer pretreated HAP catalysts were attributed to improved Pd distribution. As with the catalysts prepared by IE, the differences between EDX and ICP-OES metal loading values for the pretreated samples were lower than those for the control sample, which is believed to be due to the greater share of Pd nanoparticles in the buffer treated catalysts, which fall below EDX limits, resulting in higher catalytic activity in DRM.

The catalyst showing the highest activity was the sample treated at pH 10, which was the same pH utilised during the synthesis of HAP, and it was similar to the result observed for the IE method. It is noteworthy, that the $CO_2$ conversions varied from $CH_4$ of the same sample, depending on pH utilised during IW process. The untreated sample and the catalyst prepared at pH 12 exhibited the same response with 1:1 molar ratio with high equilibrium attained accompanied by high selectivity towards CO and $H_2$ formation, while catalysts treated at different pH varied. In the case where conversion of $CH_4$>$CO_2$, thermal cracking of methane occurred along with catalytic activation. On the other hand, in the case of samples when $CO_2$ conversions exceeded $CH_4$, production of syngas was influenced by the simultaneous existence of the water-gas shift reaction (*Equation 4.6*), described in great detail elsewhere.[15]

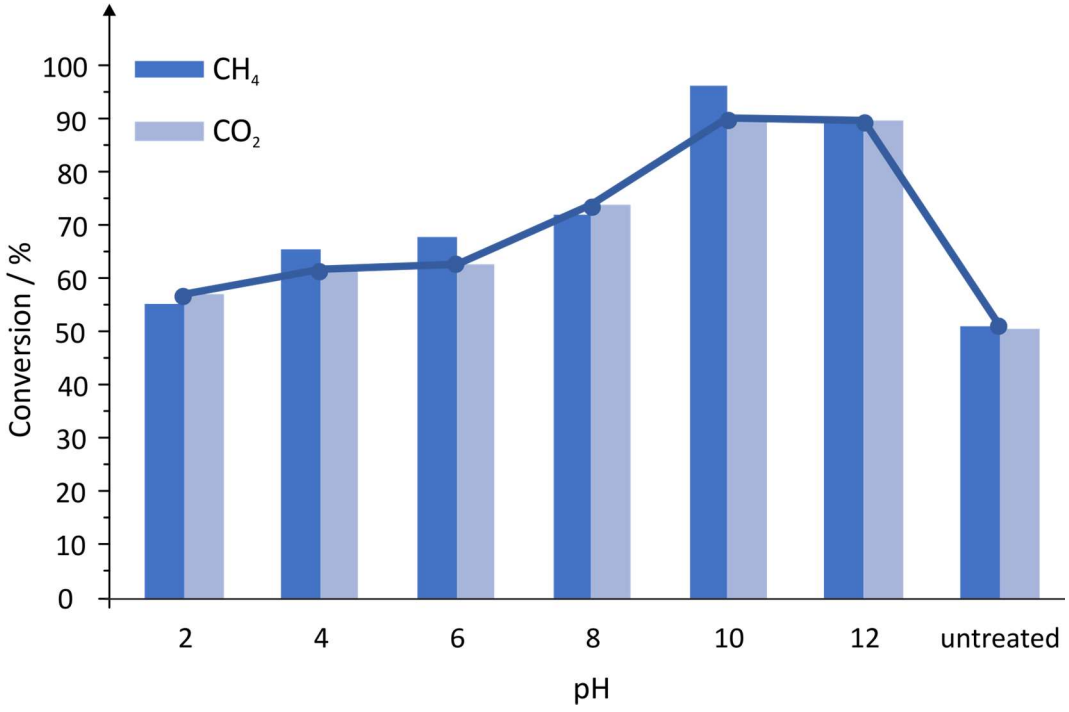


***Figure 5.7*** *DRM of IW doped catalysts at pretreated HAP fabricated using different pH*

## 5.4 Conclusions

This chapter has explored the influence of ultrasound and pH media during IE and IW doping processes on the metal distribution and their consequent catalytic activity towards DRM. Ultrasound was employed to assist the standard IE and IW procedures and Pd distribution on the resulting samples was investigated *via* ICP-OES and EDX. Metal distribution throughout the samples after ultrasound-assisted IE remained stable and catalytic activity decreased by 20%, most likely due to the formation of agglomerates. However, ultrasound significantly accelerated the IE process from 3 days to 3 hours and kept a homogenous metal distribution. Similar observations were made on IE samples at different pH values, where a stable Pd dispersion on HAP was obtained. Nevertheless, in alkaline media, $CH_4$ and $CO_2$ conversions decreased when compared to the standard IE procedure that took place in neutral pH.

Otherwise, ultrasound-assisted IW considerably improved both metal distribution and catalytic activity (by nearly 15%) of the resulting materials when compared to the standard IW protocol. Additionally, pretreatment of HAP at different pH values appeared to promote homogenous metal loading, substantially enhancing $CH_4$ and $CO_2$ conversions by 40% at pH 10. Finally, the physical and chemical treatments described in this chapter are easy adaptable and offer powerful alternatives to standard doping methodologies that overcome irregular metal distribution and make the material more reliable for real applications.

## 5.5 References

1. J. Kamieniak, E. Bernalte, C. Foster, A. Doyle, P. Kelly and C. Banks, *Catalysts*, 2016, **6**, 119.
2. Z. Boukha, J. L. Ayastuy, J. R. González-Velasco and M. A. Gutiérrez-Ortiz, *Applied Catalysis B: Environmental*, 2017, **201**, 189-201.
3. D. Chlala, M. Labaki, J.-M. Giraudon, O. Gardoll, A. Denicourt-Nowicki, A. Roucoux and J.-F. Lamonier, *Comptes Rendus Chimie*, 2016, **19**, 525-537.
4. M. Rakap and S. Özkar, *Catalysis Today*, 2012, **183**, 17-25.
5. M. Rakap and S. Özkar, *International Journal of Hydrogen Energy*, 2011, **36**, 7019-7027.

6. J. W. Jaworski, S. Cho, Y. Kim, J. H. Jung, H. S. Jeon, B. K. Min and K.-Y. Kwon, *Journal of Colloid and Interface Science*, 2013, **394**, 401-408.
7. J. Okal, M. Zawadzki, L. Kępiński, L. Krajczyk and W. Tylus, *Applied Catalysis A: General*, 2007, **319**, 202-209.
8. W. Bleam, in *Soil and Environmental Chemistry (Second Edition)*, Academic Press, 2017, DOI: https://doi.org/10.1016/B978-0-12-804178-9.00004-5, pp. 147-187.
9. K. C. De Berg, *Science & Education*, 2003, **12**, 397-419.
10. J. Haber, J. H. Block and B. Delmon, *Manual of Methods and Procedures for Catalyst Characterisation*, Physical Chemistry Division Commision on Colloid and Surface Chemistry, Great Britain, 1995.
11. G. J. Hutchings and J. C. Védrine, in *Basic Principles in Applied Catalysis*, ed. M. Baerns, Springer Berlin Heidelberg, Berlin, Heidelberg, 2004, DOI: 10.1007/978-3-662-05981-4_6, pp. 215-258.
12. B. Rêgo De Vasconcelos, L. Zhao, P. Sharrock, A. Nzihou and D. Pham Minh, *Applied Surface Science*, 2016, **390**, 141-156.
13. D. Liao, W. Zheng, X. Li, Q. Yang, X. Yue, L. Guo and G. Zeng, *Journal of Hazardous Materials*, 2010, **177**, 126-130.
14. Y. Hashimoto and T. Sato, *Chemosphere*, 2007, **69**, 1775-1782.
15. R. Horn and R. Schlögl, *Catalysis Letters*, 2015, **145**, 23-39.

# Chapter 6: Methane Oxidation over Pd, Ni and PdNi/Hydroxyapatite Catalysts

# 6.1 Introduction

In this chapter the methane oxidation reaction over Pd and Ni doped HAP catalysts was investigated under stoichiometric conditions. Selected synthesised catalysts were tested for their activity towards the oxidation of methane. Special attention was devoted to the conditions of the reaction and their influence on the transition between metal oxide and reduced metal *via* reduction and oxidation of the metal species prior to catalysis. The behaviour of the metals was studied in oxygen rich conditions and compared to the profile of a commercially available catalyst. After $CH_4$ oxidation, all the samples were tested towards coke formation *via* TGA. Note that the catalysts' names refer to previously synthesised and described samples summarised in *Table 4.1*. Results within this chapter have been submitted for the publication in Catalysis Communications and are under review.

## *6.1.1 Principles of Oxidation of the Methane Reaction*

It have been already mentioned that exhaust from a dual-fuel engine has a slightly acidic pH. Apart from this, it is also more likely to be an oxygen rich environment. Thus, in order to reproduce those conditions, the methane oxidation reaction is the closest setup to that in real life, and therefore of high interest.

The oxidation of methane is a one-step reaction for methane conversion, where pure oxygen or air is employed as an oxidant. There are two types of such oxidation described in the literature: complete and partial. Complete oxidation (*Equations 6.1* and *6.3*) occurs at low temperatures and is thermodynamically favourable, but more importantly it results in a mixture of $CO_2$ and $H_2O$, which has a higher value in the transport sector, but less value in the chemical industry, where the desirable product is syngas. On the other hand, partial oxidation became the most popular trend in research out of all methane transformation methodologies, since it allows the production of syngas with minimised energy input.

It is worth noting, that for both types of oxidation, there is the only one exothermic process from all methane conversion reactions, however at the same time it can lead to additional side reactions within the system. Nevertheless, the major limitations of the partial oxidation of methane are safety issues regarding pure oxygen, which is considered as highly dangerous in industrial applications. Moreover, the high temperatures required to activate methane and oxygen make the reaction very difficult to control, where hot spots are formed on the surface of the catalyst, leading to local overheating and reduced stability.[1]

Chemical reactions that take place during the oxidation of methane are governed by the thermodynamics of their reaction equilibria.[2] However, in the system where there is more than one equilibrium, there may be several possible different routes to obtain the desired products and/or by-products. In fact, an example of such a system is the partial oxidation of methane, where some of the reactions are practically irreversible (*Equations 6.1-6.3*).

$$CH_4 + 2O_2 \rightarrow CO_2 + 2H_2O, \Delta H = -891\ kJ\ mol^{-1} \quad 6.1$$

$$CH_4 + 1/2O_2 \rightarrow CO + 2H_2, \Delta H = -37\ kJ\ mol^{-1} \quad 6.2$$

$$CH_4 + O_2 \rightarrow CO_2 + 2H_2, \Delta H = -319\ kJ\ mol^{-1} \quad 6.3$$

$$CO + H_2O \leftrightarrow CO_2 + H_2, \Delta H = -41\ kJ\ mol^{-1} \quad 6.4$$

$$CH_4 + H_2O \leftrightarrow CO + 3H_2, \Delta H = 206\ kJ\ mol^{-1} \quad 6.5$$

$$CH_4 + CO_2 \leftrightarrow 2CO + 2H_2, \Delta H = 247\ kJ\ mol^{-1} \quad 6.6$$

$$CO + 1/2O_2 \rightarrow CO_2, \Delta H = -282\ kJ\ mol^{-1} \quad 6.7$$

$$H_2 + 1/2O_2 \rightarrow H_2O, \Delta H = -286\ kJ\ mol^{-1} \quad 6.8$$

According to equation *6.2,* this is a direct route to produce syngas, thus this reaction has been given great attention by scientists, questioning if it is possible to perform catalysis *via* only Equation *6.2* during the process. In view of this, it is theoretically possible to produce syngas at all temperatures when methane and oxygen are activated. However, the remaining reactions also play an important role, hence the product composition is controlled by global equilibrium of all the species present.

In fact, there are no reports published so far showing any undeniable evidence of a direct route to obtain syngas *via* Equation *6.2* only.[3] It is also interesting to note, that the possible side reaction shown in *Equation 6.6* is in fact the same reaction to that of dry reforming of methane.

Other important aspects worth mentioning that can interfere with the results obtained are heat and mass transport. For exothermic processes, the rising challenge is to remove the heat produced from the catalyst, since these may lead to the formation of hot spots which complicate the evaluation of the kinetics and reaction mechanisms involved.[4] The formation of hot spots is found from the ratio between thermal diffusivity ($\alpha$) and mass diffusivity ($D_{ij}$). However, catalytic material that exhibits high thermal conductivity may help to prevent the formation of small hot spots by distributing heat evenly throughout the system.[5]

In the past years, the mechanism of catalytic partial oxidation of methane has been investigated more than any other methane reforming process. Numerous scientists suggest that the reaction takes place following two routes; a direct mechanism that involves complete dissociation of methane and oxygen on the catalyst surface or a stepwise mechanism where deep oxidation of $CH_4$ is followed by steam or $CO_2$ reforming.[6] Nevertheless, because it is impossible to experimentally study the process of the catalytic reaction thoroughly, the exact mechanism remains unclear.

### *6.1.2 Nature of the Catalyst*

Catalytic oxidation of methane remained unexplored until 1990.[7] After investigating different supports coated with noble and non-noble metals with similar composition to other methane reforming catalysts, by end of 1993 the focus began to shift to stability, understanding the mechanisms involved and transitions between reduced metal and oxidised metal of the catalyst during methane oxidation.

Based on Pd coated catalysts, during this reaction at high temperatures, conversion of PdO to Pd has a profound effect on the catalytic activity.[8] At low temperatures, PdO is thought to be the phase that is more catalytically active for methane

oxidation and the transformation from PdO to Pd generally leads to a decrease in catalyst performance as the temperature increases. Such a reaction is observed due to a redox cycle between the metal oxide and the reduced metal oxide, but it is impossible to monitor this transformation experimentally.[9]

However, Lyubovsky *et al.* reported that the metallic form of Pd is more advantageous than PdO for the methane oxidation reaction, especially at higher temperatures.[9] On the other hand, Farrauto *et al.* described the phase transformation of PdO to Pd using thermogravimetric analysis (TGA) and observed that PdO decomposes to Pd at higher temperatures, however it transforms back to PdO upon cooling.[10]

Fujimoto *et al.* reported that the catalytic activity is due to the interaction between Pd and PdO. They described that low temperature methane decomposition is enhanced by the presence of oxygen atoms and oxygen vacancies on the surface of the catalyst.[11] Also, other authors such as Zhang *et al.* claimed that the highest catalytic activity is observed when the catalyst contains both Pd and PdO, and that the presence of Pd/PdO interfaces generates oxygen mobility that is beneficial for $CH_4$ oxidation.[12]

In addition, Pd particle size and the nature of the support plays an important role in the catalytic behaviour of these systems, with smaller metal particles exhibiting a higher tendency to be oxidised.[13] Nevertheless, understanding and controlling the phase transformations of metal based catalysts during methane oxidation is crucial, but not entirely clear for the scientists, thus it remains a subject of scrutiny.

The present work reports on methane oxidation under oxygen-rich conditions over Pd, Ni and Pd/Ni doped HAP and the behaviour of the metals during the reaction is studied. Also, the acid/base properties of HAP are investigated in the reaction stream.

## 6.2 Experimental

### *6.2.1 Experimental Conditions*

The catalytic experiments were performed using a modified in-house built catalysis setup, described in *Chapter 4*. This time, a feed mixture of 100 mL $min^{-1}$, comprising $CH_4$:$O_2$:He in the proportions 5:10:85 was used in all catalytic tests. Prior to the reaction, each catalyst was reduced in a flow of 30 mL $min^{-1}$ $H_2$ for 1 hour at 300°C, followed by purging with helium, while the temperature was adjusted to that of the reaction (200°C). Measurements were recorded at 50°C intervals (after holding at that temperature for 5 min) between 200 and 650°C, using a heating rate of 10°C $min^{-1}$. The same sample of catalyst was also oxidised in a flow of 30 mL $min^{-1}$ $O_2$ for 1 hour at 300°C and the catalytic reaction was performed following the same procedure described above.

### *6.2.2 Catalysts and Other Analysis Performed*

All tested catalysts were synthesised and characterised previously, as described in *Chapter 4*, based on HAP discussed in *Chapter 2*. The samples tested were *Pd_6, Pd_8, Pd_14, Pd_16, Pd_17, Pd/Ni_1, Ni_3* and *Ni_5* and all samples were benchmarked against a commercially available catalyst, *Comme_1*. After the reaction, the coking process was studied *via* TGA analysis.

## 6.3 Results and Discussion

All synthesised catalysts were tested towards $CH_4$ oxidation using a quartz fixed bed reactor, coupled with GC-TCD, as described in the experimental section. The reaction conditions employed were oxygen-rich with a molar ratio $CH_4$:$O_2$ of 1:2 in order to obtain complete oxidation (*Equation 6.1 or 6.3*), shift reaction (*Equation 6.4*) or CO oxidation (*Equation 6.7*) to fully oxidise the $CH_4$ and to prevent formation of toxic CO, which is disadvantageous in the transport sector.

### *6.3.1 Methane Oxidation over reduced Pd, Ni and Pd/Ni based Catalysts*

Similarly, the selected doped catalysts were tested towards the methane oxidation reaction as the temperature was ramped between 200-650°C, with the activity measured at steps of 50°C. Prior to the reaction, each catalyst was reduced to metal $Pd^0$ or $Ni^0$ using a continuous flow of $H_2$ as a reducing agent (similar to that of DRM, described in *Chapter 4*). As presented in *Figure 6.1*, all the Pd based samples were catalytically active at low temperatures. However, a loss of catalytic performance was observed at a temperature of 350°C. It is worth noting, that due to the oxygen present in the reaction, a redox cycle occurred between reduced metal and oxidised metal, as shown in *Figure 6.2*.[15] Consequently, as the temperature increased, an enhanced diffusion rate of the bulk oxygen in the metal oxides can be perceived and, hence the amount of consumed lattice oxygen increases. This was associated with a decrease of feed oxygen available for the reaction causing the observed drop in catalytic performance. The outlier to this trend is sample *Pd_14*, where the metal redox cycle shifted to 400°C, suggesting a different metal distribution on the support and altered oxygen availability for the metal to be oxidised. Interestingly, sample *Pd_14* was the most porous sample, thus it can be assumed that the observed shift in the activity was a consequence of more metal particles exposed to the reaction.

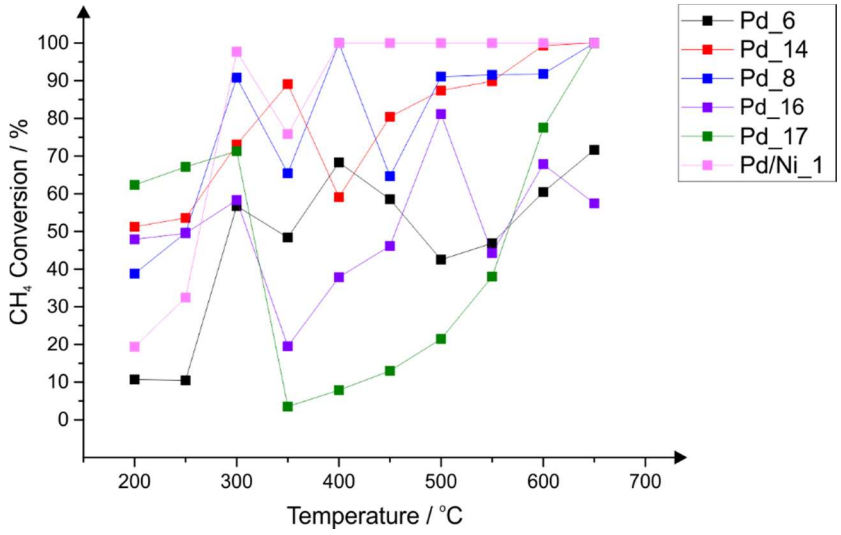


***Figure 6.1*** *Methane oxidation of Pd based catalysts as a reduced metal*

Subsequently, at the higher temperatures, the catalytic performance of all samples increased, followed by another drop in the activity in some samples between 400-550°C. Hence, it was clear that among the feed oxygen available in the stream, the adsorbed lattice oxygen of the metal oxide was the active specie for the complete oxidation of methane.

Therefore, this implied that the oxygen from the metal oxide took a direct part in the catalysis, successively forming reduced metal, which then used the oxygen species from the feed of the reaction to re-oxidised back to the metal oxide form, as presented in *Figure 6.2*.This observation agreed with what has been reported elsewhere.[12] As the reaction proceeded to higher temperatures, catalytic activity increased for all the samples.

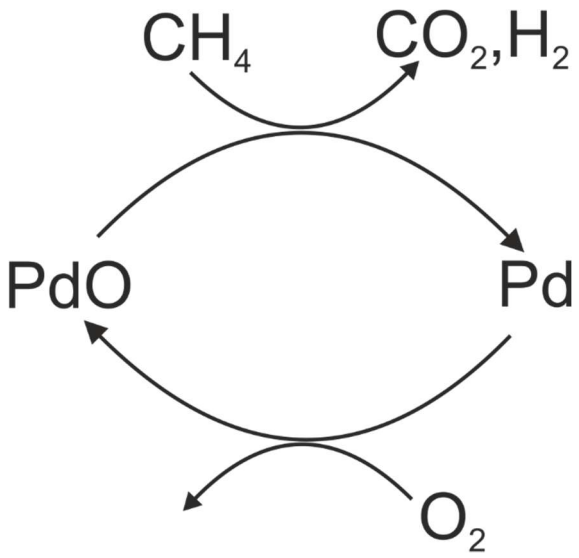


***Figure 6.2*** *Simplified redox cycle of Pd based catalyst under oxygen rich conditions*

On the other hand, Ni based catalysts revealed a similar catalytic trend to that of Pd based samples when Ni was reduced prior to the reaction, and showed a general rise of catalytic activity with an increase in temperature (as shown in *Figure 6.3*). A decrease in catalytic activity was observed at temperatures of 350°C and 550°C for *Ni_3* and 450°C for *Ni_5*, due to metal/metal oxide transformations, which were similar results to those obtained for Pd catalysts. It is worth noting, that the sample with a mixture of both Pd and Ni metals (*Figure 6.1*) demonstrated higher $CH_4$ conversions, when compared to single metal catalysts; showing 100% conversion of $CH_4$ at the low

temperature of 400°C. This phenomenon can be explained by the presence of more active sites on the surface of the HAP and, hence greater metal availability for the reaction, as the two metals undergo oxidation/reduction reactions.

Besides synthesised catalysts, the commercial catalyst obtained from the market (the same as that studied in *Chapter 4*) was tested following the same procedures. In fact, it is difficult to make direct comparisons, since the texture of the commercial sample was not powder, but coated metal sheet. It is interesting to note, however, that the *Comme_1* sample exhibited lower methane conversions at lower temperatures (below 350°C) when compared to all described all Pd and Ni based catalysts. In fact, no fluctuations were observed through the redox cycle, possibly due to the substrate present being able to stabilise metal particles and inhibit the redox cycle by some method.

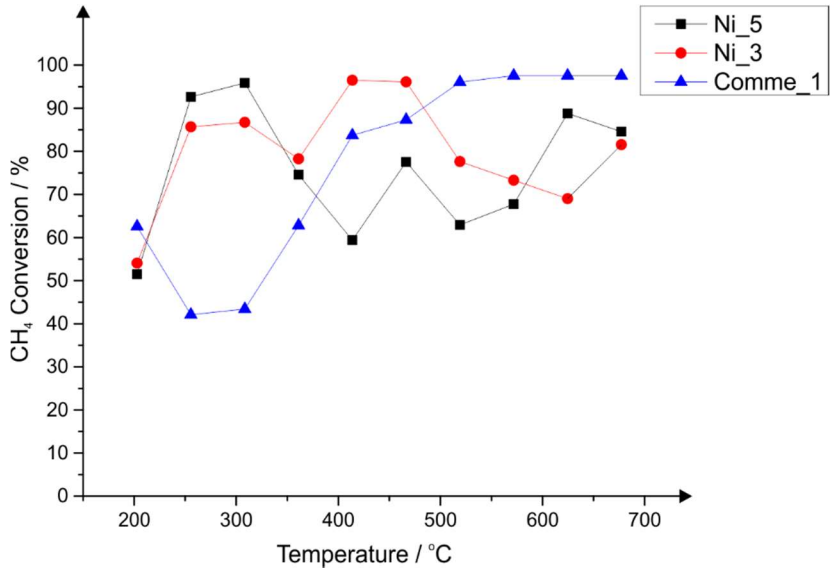


**Figure 6.3** *Methane oxidation of Ni based catalysts as a reduced metal*

## *6.3.2 Methane Oxidation over PdO, NiO and PdO/NiO based Catalysts*

After the reaction described above, the system was cooled down in a stream of He and then each catalyst was fully oxidised using a continuous flow of oxygen to create strongly bonded oxygen onto the metal. It was observed that, after the hydro-

gen treatment, the reduced metal catalysts were grey in colour, whereas after employing oxygen prior to the reaction all the catalysts turned brown, due to the progressive oxidation of the metal. The catalytic reaction was then performed under the same conditions as before.

As presented in *Figure 6.5*, as the reaction temperature increased, enhanced $CH_4$ conversion was observed. Nevertheless, at a temperature of 300°C, all conversions remained stable when compared to those at 250°C, suggesting that the metal began to undergo the aforementioned redox cycle at this temperature. However, due to the large fraction of bulk PdO and the oxygen present in the reaction, transformation of the metal oxide to reduced metal *via* the redox cycle was not favourable. This led to more stable catalytic profiles at higher temperatures when compared to reduced metal catalysts.

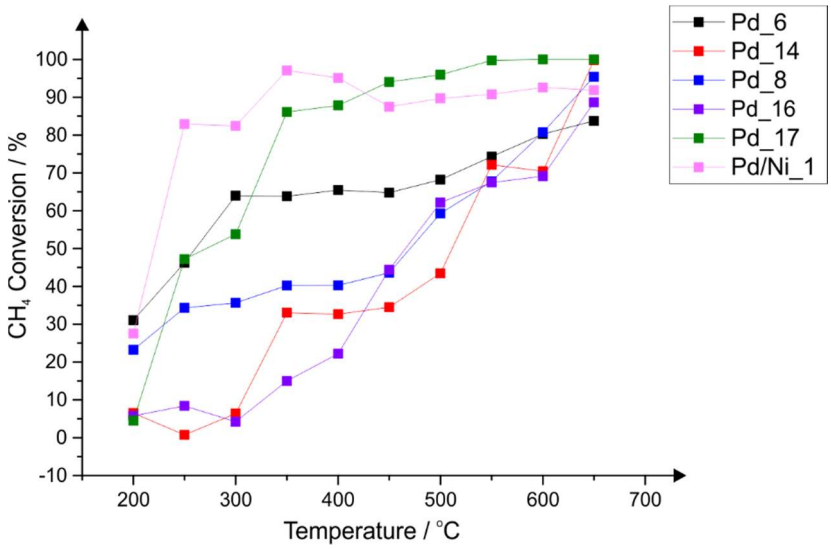


**Figure 6.4** *Methane oxidation of Pd based catalysts as an oxidised metal*

At the highest tested temperature of 650°C, all Pd based catalysts revealed high methane conversions of not less than 80%. On that basis, oxidised metal catalysts showed greater catalytic performance to that of reduced metal samples. This observation supported the hypothesis described above, that the oxygen species from the metal oxide were directly involved in the catalysis reaction. Similar results were reported by Datye *et al.,* where Pd↔PdO phase transformation during methane oxidation reactions was described.[8]

Moreover, they theorised that the observed redox cycle and formation of oxide caused surface roughening (and, therefore, increased surface area), and hence, resulted in higher activity of PdO, than reduced Pd metal, which was consistent with results obtained here.

Similar catalytic profiles were observed for Ni based catalysts, as shown in *Figure 6.5*, where in the presence of oxygen in the reaction, alterations between metal and metal oxide were not favourable, displaying more stable catalytic conversion profiles. It was noted that, $CH_4$ conversions by Ni based catalysts at lower temperatures (200°C) were higher, when compared to Pd doped samples, with samples exhibiting 40-65% $CH_4$ conversion for Ni and 5-30% for Pd samples, respectively (*Figure 6.4* and *6.5*).

On the other hand, sample *Comme_1* revealed a high catalytic profile, reaching nearly 100% $CH_4$ converted at a low temperature of 300°C. This was in agreement with what was observed when metal present in the sample was reduced, and indicated that the corrugated metal sheet employed as a substrate played a key role in stabilising and enhancing the availability of the active metal to the reaction.

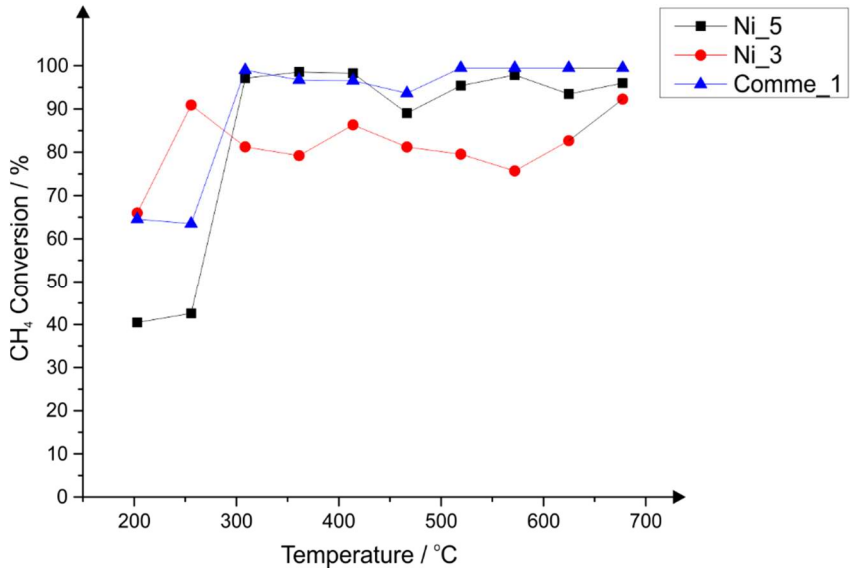


**Figure 6.5** *Methane oxidation of Ni based catalysts as an oxidised metal*

### *6.3.3 Coking Process*

Finally, after all the catalytic reactions were completed, TGA analysis was performed to investigate coke formation, which is the major lifetime limitation of the catalyst. As presented in *Figure 6.6*, the results obtained revealed a minimum weight loss, ranging from 1.0 to 3.0 wt% and 3.0 to 5.0 wt% for Pd and Ni based catalysts, respectively.

Even though non-noble metals have been previously described in the literature as less resistant to coke deposition in catalytic reactions[16], the Ni based catalysts reported here showed very low weight loss under an oxygen-rich reaction environment. Such low values obtained suggested that all the samples were also resistant to the coking process under the conditions studied, making them powerful alternatives to the existing catalysts.

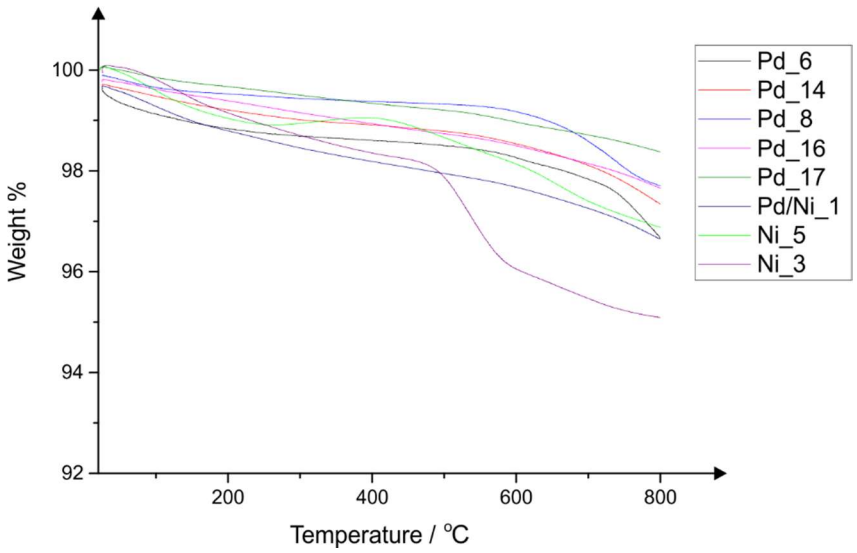


***Figure 6.6*** *TGA profiles of all teste d catalysts after performed reaction*

## 6.4 Conclusions

This chapter has explored the methane oxidation reaction in oxygen-rich conditions over Pd and Ni loaded upon the surface of mesoporous hydroxyapatite. All catalysts were evaluated towards $CH_4$ oxidation as both reduced and oxidised metals, and the behaviour of the metals in the reaction was investigated. The results obtained demonstrated that the reaction studied proceeds *via* a redox cycle between metal oxide and reduced metal.

Moreover, the oxidised metal was found to be more active than the reduced metal and exhibited more stable $CH_4$ conversions throughout the temperature ramp, suggesting that, along with the oxygen present in the stream, adsorbed lattice oxygen took a direct part in the methane oxidation reaction.

TGA analysis revealed that all tested catalysts were resistant to coke formation under the conditions studied.

## 6.5 References


1. P. Tang, Q. Zhu, Z. Wu and D. Ma, *Energy & Environmental Science*, 2014, **7**, 2580-2591.
2. B. Christian Enger, R. Lødeng and A. Holmen, *Applied Catalysis A: General*, 2008, **346**, 1-27.
3. S. A. Al-Sayari, *The Open Catalysis Journal*, 2013, **6**, 17-28.
4. J. Y. Lee, W. Jeon, J.-W. Choi, Y.-W. Suh, J.-M. Ha, D. J. Suh and Y.-K. Park, *Fuel*, 2013, **106**, 851-857.
5. V. L. Barrio, G. Schaub, M. Rohde, S. Rabe, F. Vogel, J. F. Cambra, P. L. Arias and M. B. Güemez, *International Journal of Hydrogen Energy*, 2007, **32**, 1421-1428.
6. S. A. Vladimir and V. K. Oleg, *Russian Chemical Reviews*, 2005, **74**, 1111.
7. S. De, J. Zhang, R. Luque and N. Yan, *Energy & Environmental Science*, 2016, **9**, 3314-3347.
8. A. K. Datye, J. Bravo, T. R. Nelson, P. Atanasova, M. Lyubovsky and L. Pfefferle, *Applied Catalysis A: General*, 2000, **198**, 179-196.
9. M. Lyubovsky and L. Pfefferle, *Catalysis Today*, 1999, **47**, 29-44.
10. R. J. Farrauto, M. C. Hobson, T. Kennelly and E. M. Waterman, *Applied Catalysis A: General*, 1992, **81**, 227-237.

11. K. I. Fujimoto, F. H. Ribeiro, M. Avalos-Borja and E. Iglesia, *Journal of Catalysis*, 1998, **179**, 431-442.
12. X. Zhang, C. S. M. Lee, D. M. P. Mingos and D. O. Hayward, *Applied Catalysis A: General*, 2003, **240**, 183-197.
13. T. R. Baldwin and R. Burch, *Applied Catalysis*, 1990, **66**, 359-381.
14. S. Sugiyama, Y. Iguchi, H. Nishioka, T. Minami, T. Moriga, H. Hayashi and J. B. Moffat, *Journal of Catalysis*, 1998, **176**, 25-34.
15. K. Asami, T. Shikada, K. Fujimoto and H. Tominaga, *Industrial & Engineering Chemistry Research*, 1987, **26**, 2348-2353.
16. E. Baktash, P. Littlewood, R. Schomäcker, A. Thomas and P. C. Stair, *Applied Catalysis B: Environmental*, 2015, **179**, 122-127.

# Chapter 7: General Conclusions and Future Work

## 7.1 General Conclusions

In this thesis, the development of new catalysts for methane management in dual-fuel HGVs has been explored. Based on the great number of samples synthesised, characterised and tested, together with the results obtained, this thesis contributes to the understanding and extends the knowledge in the exciting and powerful field of the preparation and use of catalysts to manage methane derived from the transport sector.

First, hydroxyapatite (HAP) was selected as a support for the catalyst due to its valuable properties and it has been synthesised using a novel wet chemical approach that utilised less toxic substrates and required less energy during the process, when compared to techniques described in the literature. A number of soft templates were investigated to enhance the porosity of HAP and an improvement in BET surface area from 12.3±0.1 $m^2g^{-1}$ to 84.9±0.3 $m^2g^{-1}$ was successfully obtained. Moreover, hard-templating was studied for the synthesis of mesoporous HAP using carbon nanorods. This novel approach was reported for the first time in the literature and a remarkable improvement in the surface area of HAP (242.2±2.3 $m^2g^{-1}$) was achieved. All resulting materials were thoroughly characterised for their physicochemical properties using SEM, EDX, TEM, XRD, Raman, FTIR and BET.

Next, attention was turned to the stability of HAP after pH, thermal and mechanical treatments by simulating in the laboratory the expected conditions in which catalysts would be exposed in the exhausts of HGVs during running on roads. The main findings of those studies were that the mesoporous HAP was fully stable under mechanical disturbances caused by ultrasound, as well as when it was exposed to different pH. Only under temperature treatments around 650°C did the HAP start to dehydroxylate to form OHAP with further decomposition to β-TCP and TTCP above 750°C, which was an advantageous results considering that the critical temperature at which HAP started to dehydroxylate was higher than the standard operating temperatures of the engines (up to 500°C).

Innovation in the performing of doping protocols to prepare metal based HAP catalysts was also explored in this work. In order to improve metal distribution throughout the support, ultrasound was employed as a tool to assist in the doping process of HAP with Pd. On the other hand, the study of the influence of the pH in the metal doping of HAP was also carefully study. The results obtained from both approaches were compared to conventional doping methods *i.e.* ion exchange (IE) and incipient wetness impregnation (IW). It was found that ultrasound-assisted IW significantly improved the distribution of the metal while the distribution after ultrasound-assisted IE remained homogenous distribution.

However, the process was efficiently accelerated from 3 days to 3 hours which was the main advantage. On the other hand, it was observed that pretreatment of HAP with different pH before conducting the IW protocol considerably enhanced the metal distribution when compared to conventional IW procedure. Moreover, metal distribution remained high when IE took place in a different pH buffer solution instead of neutral water. Finally, the physical and chemical treatments described herein are easy adaptable and offer powerful alternatives to standard doping methodologies that overcome irregular metal distribution and make the material more reliable for real applications.

All synthesised catalysts together with a commercial sample were intensely investigated for the transformation of methane under oxygen lean and rich conditions, using the dry reforming of methane (DRM) reaction with $CO_2$ as an oxidant and *via* the complete oxidation route in order to reproduce possible conditions found in exhausts, respectively. The products of both reactions were analysed using an in-house built catalysis rig that involved a fixed-bed reactor coupled to a GC-TCD. Operating conditions of the rig were previously optimised to ensure its efficient utilisation and reproducibility and repeatability studies were carefully performed to assure the correct analytical performance of the instrument.

Following the DRM reaction, it was observed that the most active catalyst converted 100% of methane at an extremely low 250ºC, which impressively exceeded the commercially available catalyst tested under the same conditions.

The outstanding catalyst was then subject to stability study, which revealed that the sample was generally stable with an activity of 80% $CH_4$ of conversion at 300°C over a time of 88 hours of continuous reaction.

On the other hand, in the case of complete oxidation of methane the results obtained demonstrated that the reaction proceeded through a redox cycle between reduced metal and metal oxide. Furthermore, oxidised metal was found to be more active when compared to reduced metal and exhibited more stable conversion profiles. This suggested that, in the presence of oxygen in the reaction stream adsorbed lattice oxygen took direct part in the catalysis process.

The final analysis of the materials synthesised and tested in the present work involved the evaluation of the coking process after the catalytic reactions, as a well-described major life limitation for the catalysts. TGA was successfully employed for this purpose and based upon the results obtained, all tested catalysts were resistant to coke formation under the conditions studied.

## 7.2 Suggested Future Work

Catalysis of methane in dual-fuel engine of HGV engines exhibits a complex nature and involves many different parameters that can influence the reaction. Therefore, this work still needs further experiments in certain areas to develop a better understanding of the process, and the possible future work could be continued, considering the following aspects:

- Natural gas (NG) could be employed instead of pure methane gas for the DRM and oxidation of methane reactions in order to reproduce engine fuel utilised in real life
- Investigate possible poisoning effect of the catalysts caused by $H_2S$, which is present in a small proportions in NG
- The best catalysts could be studied for their activity towards methane in the presence of water vapour, which can promote side reactions in the system leading to change in the compositions of reaction products

- Regarding ultrasound-assisted IE doping method investigated, duration of the ultrasonic treatment could be optimised to achieve the best distribution with the best catalytic activity
- Metal distribution on the surface of HAP after various treatments could be extensively studied *via* $H_2$ chemisorption in order to investigate the influence of metal salt, pH, ultrasound and doping method
- The magnetron sputtering technique could be utilised to modify HAP as a novel doping methodology to coat powders that excludes any possible contaminations raising from metal precursors

# Chapter 8: Relevant Publications and Patents arising from this Thesis

1. **J. Kamieniak**, E.P. Randviir, C.E. Banks, The latest developments in the analytical sensing of methane, TrAC Trends in Analytical Chemistry 73 (2015) 146-157

2. **J. Kamieniak**, E. Bernalte, C.W. Foster, A.M. Doyle, P.J. Kelly, C.E. Banks, High Yield Synthesis of Hydroxyapatite (HAP) and Palladium Doped HAP via a Wet Chemical Synthetic Route, Catalysts 6(8) (2016) 119

3. **J. Kamieniak**, A.M. Doyle, P.J. Kelly, C.E. Banks, Novel synthesis of mesoporous hydroxyapatite using carbon nanorods as a hard-template, Ceramics International 43(7) (2017) 5412-5416

4. **J. Kamieniak**, E. Bernalte, A.M. Doyle, P.J. Kelly, C.E. Banks, Can Ultrasound or pH Influence Pd Distribution on the Surface of HAP to Improve Its Catalytic Properties in the Dry Reforming of Methane?, Catalysis Letters 147(8) (2017) 2200-2208.

5. **J. Kamieniak**, P.J. Kelly, C.E. Banks, A.M. Doyle, Methane Emission Management in a Dual-Fuel Engine Exhaust using Pd and Ni Hydroxyapatite Catalysts, Fuel 208 (2017) 314-320

6. **J. Kamieniak**, P.J. Kelly, C.E. Banks, A.M. Doyle, Mechanical, pH and thermal stability of mesoporous hydroxyapatite, Journal of Inorganic and Organometallic Polymers and Materials, under review, 2017

7. **J. Kamieniak**, P.J. Kelly, A.M. Doyle, C.E. Banks, Influence of the Metal/Metal Oxide Redox Cycle on the Catalytic Activity of Methane Oxidation Over Pd and Ni Doped Hydroxyapatite, Catalysis Communications, under review, 2017

8. IP: **J. Kamieniak**, A. M. Doyle, P. Kelly, C. E. Banks, Methane decomposition at low temperature over a precious metal apatite based heterogeneous catalyst (P236707GB)